University of Liège

Applied Sciences Faculty
Centre Spatial de Liège

Thermal Design of the Oufti-1 nanosatellite

Lionel Jacques

Thesis submitted in partial fulfillment of the requirements for the degree of
Master in Aerospace Engineering

Advisor : Prof. Pierre Rochus

Academic Year 2008 – 2009

Space isn't remote at all. It's only an hour's drive away, if your car could go straight upwards.

Sir Fred Hoyle

Acknowledgments

I wish to thank all the people who helped me, during the whole year, to carry out this master thesis.

I express my sincere thanks to Prof. Pierre Rochus for his precious advice and encouragement and for giving me the opportunity to enter the very interesting world of spacecraft thermal control.

I am greatly indebted to Tanguy Thibert for his guidance, suggestions, useful feedbacks and all the support he has given throughout my work. I expressed also my sincere gratitude to all the people working at the Centre Spatial de Liège for their availability and support in helping me conducting the different tests.

I also wish to thank Philippe Poinas for his valuable advice and help in developing OUFTI-1's thermal model.

My special thanks goes to all the OUFTI-1 student and management team, especially to Amandine Denis and Jonathan Pisane who managed the project with an incomparable team-spirit. Particularly, I am thankful to Prof. Gaetan Kerschen for his valuable suggestions and recommendations and to Vincent Beukelaers who helped me during the tests.

Last but not least I thank my family and I thank you, Géraldine, for encouraging, supporting me and not being weary of always hearing me talking about OUFTI-1...

Again, many thanks to all of you, for keeping our eyes turned toward the sky...

Harzé, August 30, 2009.

Abstract

OUFTI-1 is the first nanosatellite developed at the University of Liège and even the first one ever made in Belgium. This student project takes place within the framework of a long-term goal program called LEODIUM (Liège in Latin). The goal of this program is to provide hands-on experience to engineering students through the development of a series of nanosatellite for scientific experiments in cooperation with space industries of the region of Liège.

OUFTI-1 will be the first satellite ever equipped with one of the latest digital amateur radio communication protocol : the D-STAR protocol. This technology represents one of the three payload of OUFTI-1, since one target of the mission is to test this new protocol in space. The two other payloads are high efficiency solar cells provided by Azur Space and an innovative electrical power system developed with Thales Alenia Space ETCA.

OUFTI-1 will hopefully be launched on the new European launcher Vega with eight other student nanosatellites.

This present thesis focuses on the thermal design of OUFTI-1 whose goal is to guarantee all components are functioning within their allowable temperature range. With this in mind, different thermal model of increasing complexity are developed within both Matlab/Simulink and ESATAN/ESARAD environments. based on their results, proper measures will be taken to ensure all the components works indeed in their allowable range of temperatures.

Keywords : [OUFTI-1, CubeSat, satellite, Thermal, LEODIUM, ESATAN, ESARAD]

Contents

List of Figures

List of Tables

Thesis outline

This thesis focuses on the thermal analysis of the nanosatellite OUFTI-1, developed at the University of Liège. Through it, the thermal environment the satellite will be exposed to is studied. The ultimate goal of this thesis is to take suitable measures to ensure all the components will be functioning in their safe range of temperatures and a proper heat rejection.

This work will be divided into 7 parts : first, a brief introduction about the project, the mission and the CubeSat concept. Then a preliminary analysis is conducted through Matlab/Simulink softwares to have a first guess of the temperatures the CubeSat will undergo. After that, two ESATAN/ESARAD models are developed: a first one to confirm the results of the single node Matlab/Simulink model and a second one, far more detailed, to reveal and/or confirm the possible issues. With this detailed model, a series of parametric analysis are performed to enable suitable design modification accordingly with the other subsystems to enforce thermal reliability with sufficient margins. Before developing this detailed model, measurements will be performed on critical elements such as the battery or the main structure. Finally, thermal vacuum and cycling tests that will be performed next year at the Centre Spatial de Liège will be introduced. Then we will draw conclusions and propose future development.

OUFTI-1 project, mission and nanosatellite

1

1.1 The Project Story

The LEODIUM program

The OUFTI-1 project takes place within the framework of a long-term goal program called LEODIUM. LEODIUM, besides meaning Liège in Latin, stands also for *Lancement En Orbite de Démonstations Innovantes d'une Université Multidisciplinaire* (*Launch into Orbit of Innovative Demonstrations of a Multidisciplinary University*). It involves both the University of Liège and Liège Espace, a consortium of space industries and research centers in the Liège region. In 2005, Mr. Pierre Rochus, as the president of Liège Espace and Deputy General Manager for Space Instrumentation of the Centre Spatial de Liège, was charged with the training of students to the design of miniaturized satellites. Different possibilities were foreseen and the project finally began with the participation in the Student Space Exploration and Technology Initiative (SSETI) of the European Space Agency. For two years, students were involved in the European Student Earth Orbiter (ESEO) with the design of the solar panels deployment system and also in the development of the the Narrow Angle Camera (NAC) for the European Student Moon Orbiter (ESMO).

A CubeSat, why not ?

The idea of developing a nanosatellite was already in the mind of many people at ULg but yet nothing concrete had began. One must wait until September 2007 when Mr. Luc Halbach, sales manager of Spacebel, proposed to test a new amateur radio digital technology in space on board of a CubeSat : the D-STAR protocol. It did not even take one month for a team of students and professors to set up around the newborn project. Yet it needed a name : *OUFTI-1*, which is a typical expression of the city of Liège, standing for *Orbiting Utility For Telecommunication Innovation*. In fact, the University of Liège, through the LEODIUM program, has now the ambitious goal to develop other CubeSats to keep on giving students satellite hands-on experience. Last year, in their master theses, Stefania Galli and Jonathan Pisane performed respectively the feasibility study and a detailed analysis of the D-STAR protocol.

Vega Maiden Flight

In October 2007, the ESA Education Office in cooperation with the Directorate of Legal Affairs and External Relations and the Vega Programme Office in the Directorate of Launchers, issued a first Announcement Opportunity offering a free launch on the Vega maiden flight. After presenting the project at the Vega Maiden Flight CubeSat Workshop at the European Space Research and Technology Center (ESTEC) in January 2008, ESA published a call for proposal for CubeSat on board of Vega to which we submitted our own proposal in March 2008. We finally got a positive answer in June 2008, thanks to the good presentation made 6 months earlier. Eight other CubeSats are selected (Xatcobeo for Vigo/INTA in Spain, Robusta for Montpellier in France, UNICubeSat for Rome, AtmoCube for Trieste and e-st@r for Turin in Italia, PW-Sat for Warsaw in Poland, Goliat for Bucharest in Roumania and SwissCube for Lausanne in Switzerland) and there are also two back-up (HiNCube for Narvik in Norway and UWE-3 for Würzburg in Germany). In April 2008, Amandine Denis presented the project at the 5^{th} Annual CubeSat Developers' Workshop in San Luis Obispo, USA. This year again, the status of our project has been presented during the 2^{nd} European CubeSat Workshop in January 2009 at ESTEC and at the 6^{th} Annual CubeSat Developers' Workshop in San Luis Obispo, USA.

Initially, the Vega Maiden Flight was scheduled for November 2009. This left us only a little bit more than one year to develop our CubeSat. This tight schedule involved some decisions that will be described later. Nevertheless, the flight has recently been delayed to spring 2010.

The Team

The initial team was composed of 2 second master students (Stefania Galli and Jonathan Pisane), 1 first master student (Philippe Ledent) two graduate students (Amandine Denis and Jean-François Vandenrijt), three professors (Prof. Gaëtan Kerschen (A&M Dept.), Prof. Pierre Rochus (CSL and A&M Dept.), Prof. Jacques Verly (EECS Dept.)) and Luc Halbach from Spacebel.

This year, more students joined the project so that we are now 13 students divided up into 9 subsystems:

ADCS	:	Samuel Hannay[1]
COM	:	Renaud Henrard[2] and Francois Mahy[3]
EPS	:	Philippe Ledent[3] and Pierre Thirion[3]
GND	:	Laurent Chiarello[4]
MECH	:	Jérôme Wertz[5]
MIAS	:	Vincent Beukelaers[1]
OBC	:	Nicolas Evrard[6], Johan Hardy[6] and Damien Teney[7]
STRU	:	Gauthier Pierlot[1]
THER	:	Lionel Jacques[1]

[1]ULg, Aerospace engineering; [2]Isil Institute, Electrical engineering; [3]ULg, Electrical engineering; [4]ULg, Computer engineering; [5]Gramme Institute, Mechanical engineering; [6]Gramme Institute, Electrical engineering; [7]ULg, Computer science.

Management is carried out by Amandine Denis and Jonathan Pisane, both PhD students at the University of Liège.

1.2 The Mission

In addition to give students satellite hands-on experience, OUFTI-1 mission has three main objectives. OUFTI-1 will be the first satellite ever equipped with D-STAR. The primary goal is thus the space qualification of this new technology so that a functional D-STAR repeater can be given to the amateur radio community. Hence, we will use the amateur radio frequency bandwidth reserved for the communications between the satellite and the ground station. Furthermore, seeing the worldwide coverage of the amateur radio community, they will reveal to be an invaluable help us to keep our nanosatellite in good health when it is not in sight of our ground station.

But what is D-STAR? As previously said, it is a new amateur-radio communication protocol. The main difference between conventional protocols and D-STAR is that it is digital. The quality on the voice is then definitely better. Another D-STAR key feature is that it allows simultaneous data and voice transmission.

What becomes D-STAR in space? In fact, using D-STAR in space have some consequences. The frequency shift due to Doppler Effect during one pass of the satellite is indeed too large for the acceptable bandwidth of the ICOM 2820 transceiver Doppler Effect compensation capabilities. Unfortunately, this transceiver is, at the moment, the only one able to deal with D-STAR protocol available on the market. Doppler Effect will so have to be on-board compensated. Seeing that, there will be two system-selected doppler-compensated coverage zones : the first around ULg for control and another one dynamically determined. Concerning the second one, there will probably be a registration procedure on our website for the user to reserved one pass of the satellite over a specific region. This is illustrated on the figure 1.1. This zone definition fits well with an emergency usage of D-STAR in space : in case of large scale disasters (Katrina Hurricane or more recently the earthquake that hits center Italy), common communication networks are often unavailable. D-STAR is then very useful because this recently developed protocol allows not only digital voice communication but also data transmission such as GPS data at the same time! The disaster zone could then be selected to be Doppler compensated and allow amateur radio to use this D-STAR satellite repeater to communicate and send GPS data.

Anyway, as it is also shown on the figure 1.1, any user who has the ability to make his own Doppler compensation could technically communicate with the CubeSat when it is in sight from the user and in D-STAR mode (and not in AX.25 mode for Telecommand/Telemetry communication).

As previously said, OUFTI-1 has two other payloads : high efficiency solar cells and an innovative EPS. As it will be presented in the next paragraph, nanosatellite are ideal low cost solutions for testing new technologies. Concerning OUFTI-1, AZUR SPACE Solar Power GmbH proposed us to test their new solar cells. These are 30% efficiency triple junction

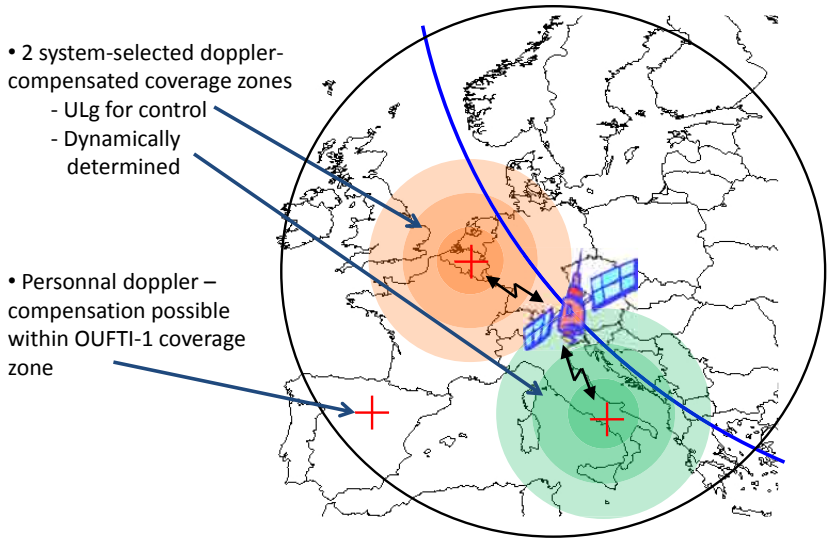

Figure 1.1 – *Mission description : Doppler-Effect compensated zones*

GaAs cells, compared to their previous 28% model or their silicon cells (type S-32) having only an efficiency of 17%. The cells are thus going to be tested in real conditions. AZUR SPACE is a world recognized company in space solar cells production and nowadays, more than 300 satellites have been equipped with solar cells without any failure[7].

The third payload is a new digital electrical power unit developed in cooperation with Thales Alenia Space (ETCA) about which we will come back later. This innovative EPS is digitally controlled and based on a PIC microcontroller and other components such as planar transformers. When the batteries voltage is high enough (and the CubeSat normally works), digital EPS will supply and be connected to the 3.3V power bus. Yet, this EPS has a relatively lower efficiency than the analog 3.3V converter (50% compared to 90%).

1.3 The Satellite

Up to this point, even if the word CubeSat has been used at least ten times, it has not yet been presented. But what really is a CubeSat or a nanosatellite ? In fact, for several years satellite have become larger and larger (e.g. Envisat launched in 2002 which weights more than eight tons and is 26 meters tall or Hubble in 1990 with its 11 tons and 16 meters) but such missions required generally about ten years of development and billions of euros. This is why there is a new tendency in reducing the size and thus costs and development time. Actually, there is now a classification of miniaturized satellites according to their wet mass : minisatellites (between 100 and 500 kg), microsatellites (between 10 and 100 kg), nanosatellites (between 1 and 10 kg) and finaly Picosatellites (between 0.1 and 1 kg). During the Second European Workshop at ESTEC, Prof.

Figure 1.2 – *OUFTI-1's three payloads*

Bob Twiggs from the *Department of Aeronautics & Astronautics* at Stanford University presented the concept of even smaller satellites : femtosatellites, weighting less than 100g, for teaching purposes ! Miniaturized and nanosatellites are now very sought-after by industrials and academics for testing new technologies under real conditions at low cost and short development time.

Within this framework, Prof. Bob Twiggs originally proposed the 10x10x10cm 1kg CubeSat Standard. Through this standard definition, he wanted to promote an easier space access and hands-on university-level space education. Standardization of the bus allows standardization of the interface between the satellite and the launcher so that standard deployment systems can be developed and launch opportunities increased. As an educational university program, the CubeSat concept is based on lowering the costs and simplicity. The use of non-space rated Commercial-Off-The-Shelf (COTS) components is thus unavoidable. The CubeSat leitmotiv is then :

In 2000, Pumpkin, Inc. decided to design a reliable off-the-shelf CubeSat Kit conform to CubeSat specifications to facilitate CubeSat development within tight schedules. As said in the presentation made Andrew E. Kalman, Pumpkin's president, the CubeSat Kit is *strong, modular, light, scalable, customizable and affordable* [47]. Now, Pumpkin offers 1-unit (1U), 2-unit and 3-unit structures and also OBC, EPS and ADCS modules. In conjunction with Prof. Jordi Puig-Suari at California Polytechnic University San Luis Obispo, a Picosatellite Orbital Deployer (POD) has been developed : the P-POD (Poly-Picosatellite Orbital Deployer). It can launch up to 3 single-unit CubeSats or any fitting combination. Nevertheless, one had to waid until 2003 to see first CubeSats in space.

Figure 1.3 – *On the left, the CubeSat Kit Structure, on the right, the P-POD*

1.4 The Subsystems

ADCS [25]

Since our payloads do not require a precise attitude control, our CubeSat will be passively controlled with hysteretic materials and a permanent magnet. The initial rotation rate given at the P-POD ejection is variable. This explains the main goal of hysteretic materials: to prevent from too high rotation rates which could cause an additional unfavorable modulation of the communication signal. Hysteretic materials will thus damp the rotational energy acquired at the deployment. But perturbation torques (gravity gradient, solar pressure, atmospheric drag...) are such as, even with hysteretic materials, the CubeSat will never stop rotating.

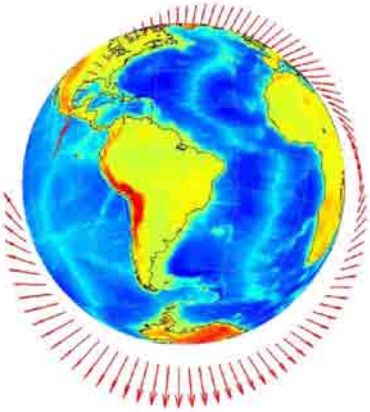

Figure 1.4 – *Earth's magnetic field orientation on the orbit[25]*

On another hand, the permanent magnet will align the satellite on Earth's magnetic field which is represented during one orbit on the figure 1.4. As the lines of the magnetic field are already falling above Belgium, the magnet will be perpendicular to the face with the antennas so that antennas are nearly perpendicular with zenith above Belgium. This is favorable by seeing antennas' radiation pattern.

COM [36],[28]

OUFTI-1 will use the amateur radio communication bands : 435 MHz for the uplink and 145 MHz for the downlink. As described previously, D-STAR communication protocol will be used as payload. Nevertheless, AX.25 protocol has been chosen for TC/TM[1] to avoid TC/TM relying on the experimental communication payload. Anyway, there is also a reliable CW beacon sending continuously satellite's key housekeeping parameters that any ham-radio operator in the world will be able to listen and forward to us.

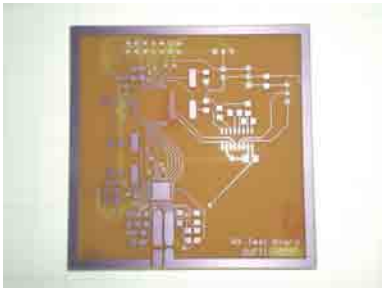

Figure 1.5 – *OUFTI-1's test RX PCB[36],[28]*

EPS [55],[33]

Figure 1.6 – *Main EPS engineering model*

The primary function of the EPS is to store the energy collected by the solar cells in the batteries and provide the bus with the required voltages. Concerning OUFTI-1, 5 faces of the CubeSat will be covered with 2 solar cells connected in series, the remaining face being dedicated to the antenna deployment mechanism. As previously presented, solar cells are our second payload and are provided AZUR SPACE. The exact battery model is not yet defined but Varta or Kokam lithium polymer batteries are nevertheless foreseen for their high energy density. The EPS contains three power bus: 3.3V, 5V and 7.2V.

In addition to the main and robust 3.3V converter, an innovative digital EPS is being developed in cooperation with Thales Alenia Space ETCA, already presented in a previous paragraph.

GND [10]

The Ground subsystem consist in the tracking antennas, its remote control and the scheduler. The Main Tracking Station, located on the campus of the University of Liège, will be made of two separated units : the first one located at the Poste Central de Commande (PCC) of the university and the second one, the User Tracking Station (UTS), located at the Montefiore Institute. The first one can only deal with D-STAR transmission while the UTS also supports communication with the CW beacon. The GENSO[2] compatibility is thus foreseen for the UTS. A Backup Tracking Station will

[1] TC : Telecommand, TM : Telemetry

[2] GENSO states for Global Educational Network for Satellite Operations. GENSO is a worldwide network of ground stations and spacecraft interacting via a software standard. Through this, GENSO aims to increase the return from educational space missions.

also be installed at the Redu Euro Space Center. It will be fully redundant and linked by a high speed internet tunnel with the first one.

MECH [63]

Using two frequencies (uplink and downlink), OUFTI-1 will have two monopole $\frac{\lambda}{4}$ antennas : a 17cm and a 50cm one. Throughout the launch sequence, antennas will have to be folded since the CubeSat will be in the P-POD until deployment. Therefore, the MECH subsystem has to design a reliable deployment mechanism. As shown on the figure 1.7, antennas will be winded around a dedicated panel. During the launch phase, they will be maintained by a small thread which will then be heated up to its melting point to release both antennas.

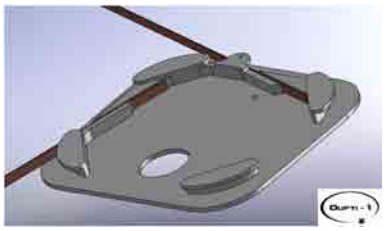

Figure 1.7 – *OUFTI-1's antenna deployment mechanism panel[63]*

MIAS [9]

Mission Analysis consists in analyzing the global comportment of the satellite in orbit. This includes lifetime evaluation, link budget with the ground station calculation, Doppler estimation and so on... To do this, a global simulator is being developed in Matlab Simulink environment in correlation with STK software. The simulator include orbit propagation, taking into account Earth's oblateness, atmospheric drag, solar radiation pressure... A simple model of each subsystem is also embedded : EPS for power calculation, ADCS for the attitude determination, COM for the link budget and Doppler considerations. A thermal model will also be provided and described later. A screenshot of the simulator is shown on the figure below.

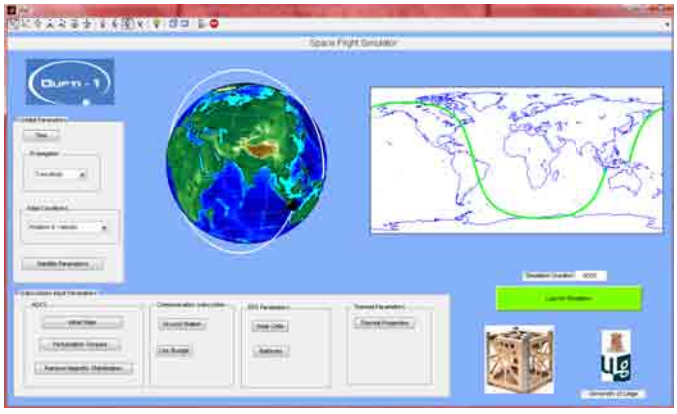

Figure 1.8 – *Snapshot of the Simulator developed by V. Beukelaers in Simulink[9]*

OBC [54],[19],[26]

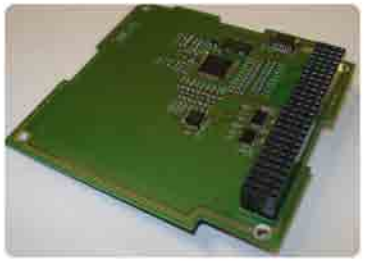

Figure 1.9 – *OUFTI-1's second OBC PCB[19]*

The On-Board Computer is the brain of the CubeSat : it controls data flow, deals with the different operational modes, ensure telemetry data formatting and storage and telecommand data decoding and management. OUFTI-1 will have two fully redundant OBC : a first robust one provided in the Pumpkin's CubeSat Kit (FM430 flight module with Texas Instruments single-chip 16-bit MSP430). But this one contains many unnecessary functionalities for us. This is why a second lighter OBC has been developed (OBC2). If this home proves itself, it will probably be used as the main and only OBC for the next OUFTI Missions. The picture 1.9 shows the home made OBC Printed Circuit Board (PCB). OBC also deals with housekeeping parameters such as batteries' voltage, solar cells' currents, temperatures...

STRU [42]

The first key objective of the Structure and Configuration subsystem is to position the many components in order to be compliant with the CubeSat design specification and many other constraints (thermal, radiations, high frequency issues). The second objective is to ensure withstanding to the harsh launch environment : even in the P-POD, the nanosatellite undergoes extremely strong vibrations. Therefore, both random and sine vibrations tests are performed in correlation with Samcef finite element models. The CubeSat should ultimately proof that its structure and equipments are capable of withstanding the maximum expected launch environment through a series of acceptance and qualification tests. Those final tests will be performed at the Centre Spatial de Liège.

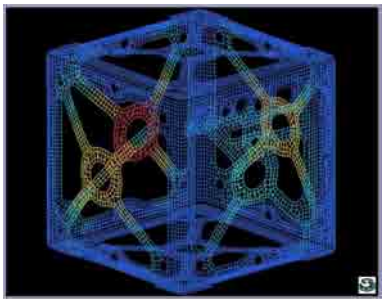

Figure 1.10 – *Finite element modal analysis with SamcefField[42]*

Seeing the tight schedule, the idea to buy the CubeSat Kit structure and OBC module (FM430) was accepted to save time and let us concentrate on our payloads and other subsystems.

1.5 OUFTI-1's anatomy

Throughout this work, different components and specific parts of OUFTI-1 will be referred to. These components are therefore introduced here through relatively detailed exploded view (figure 1.11).

The skeleton of the satellite consist of Pumpkin's 1U structure itself divided into three parts : the lateral frame and the top and bottom faces. The last two are fixed on the main frame with M3 screws not represented here (4 screws for the up face and 6 for the bottom one). We called the ports or rear side of the CubeSat the side where USB, remove-before-flight pin hole and other ports are located.

The solar cells will be glued on aluminum panels. The panels must be such as they keep the rails free (at least 8.5mm). By the rails, one means the four vertical edges of the lateral frame which are hard anodized because they are the only surfaces in contact with the P-POD. Up to now, all aluminum panels will also be glued on the structure to avoid remachining. As depicted on the view, only five of the six faces of the cube will be covered with solar cells. The remaining one is dedicated to the antenna deployment mechanism panel. OUFTI-1 will indeed have two antennas described in a later paragraph.

Inside OUFTI-1, there are five printed circuit boards (PCBs). From bottom to top, one has the OBC (CubeSat Kit's FM430 Flight Module) followed by its redundant home-made counterpart, the OBC2. Above them lies the EPS also followed by the payload : the innovative EPS (EPS2). The last PCB is the communication one on which will be located amplifiers, quartz and other electronics circuits. While the OBC is the CubeSat's brain, its heart is the EPS with its two LiPo batteries fixed on a secondary PCB and is strategically positioned as the central PCB. This PCB layout has been driven by many constraints and considerations among these the CubeSat specification stating that the center of gravity of the CubeSat has to remain inside a 4cm diameter sphere centered on the geometric center of the cube.

All the PCBs are maintained together thanks to four endless screws. They are fixed at their bottom on the bottom face of the frame and at their top on the lateral frame with the "*midplane standoffs*". The separation between PCBs is ensure by spaces which are small aluminum cylinders. We already sees that there are only 8 contact points between the PCB stack and the external structure relies : four with the bottom face and 2×2 with the lateral frame.

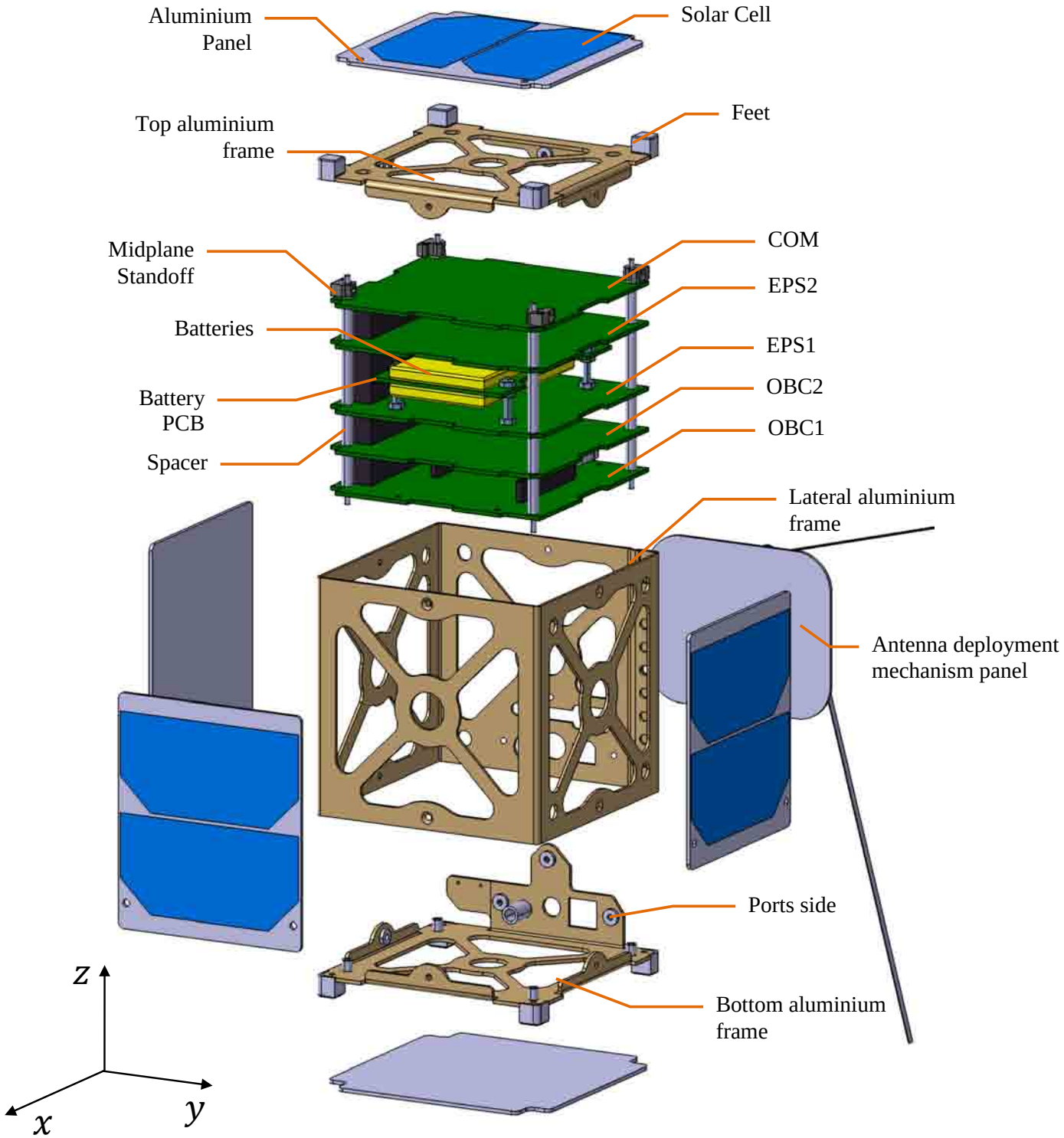

Figure 1.11 – *OUFTI-1 exploded view*

The Thermal Control Subsystem

2

This chapter introduces the basics of spacecraft thermal control. It begins with a brief recall of heat transfer and then thermal environment will be exposed. After that, we will describe in a few words what is the aim of the thermal control subsystem : why and how dealing with space thermal issues.

2.1 Space heat transfer

In general, there are three main heat transfer modes[1] : conduction, radiation and convection.

2.1.1 Conduction

In space, due to the extremely low residual pressure, only conduction and radiation modes are present[2]. Conduction is governed by Fourier's Law. For an isotropic material:

$$\vec{q} = -k\vec{\nabla} T$$

where k is the constant thermal conductivity and where $\vec{q}$ is the heat flux. This equation can be rewritten in the case of a steady unilateral flow through a surface of a thickness L and constant area S as follows :

$$Q = qS = \frac{kS}{L}\Delta T = GL_{(i,j)}(T_i - T_j)$$

This defines the thermal conductance $GL_{(i,j)}$ between the isothermal surfaces i and j.

2.1.2 Radiation

On the other hand, radiation heat transfer is governed by Stefan-Boltzmann's Law stating that the black-body irradiance is proportional to the fourth power of its temperature :

[1] Ablation, a combination of these three processes with chemical reaction, is also considered for atmospheric re-entry vehicles

[2] Nevertheless, convection must be taken into account for manned mission, launchers... (ISS, Shuttle,...)

$$E_{BB}(T) = \int_0^\infty E_{BB}(\lambda, T)d\lambda = \sigma_0 T^4 \ [W/m^2]$$

where σ_0 is the Stefan-Boltzmann's constant in vacuum defined in function of the universal constants : π, Boltzmann's constant k, the speed of light in vacuum c_0 and Planck's constant h :

$$\sigma = \frac{2\pi^2 k^4}{15c^2h^3} = 5.67051\ 10^{-8}\ [Wm^{-2}K^{-4}]$$

$E_{BB}(\lambda, T)$ is the hemispherical spectral emissive power of a black-body and is given by Planck's Law :

$$E_{BB}(\lambda, T) = \frac{2\pi hc^2}{\lambda^5(e^{\frac{hc}{k\lambda T}} - 1)}\ [W/(m^2.\mu m)]$$

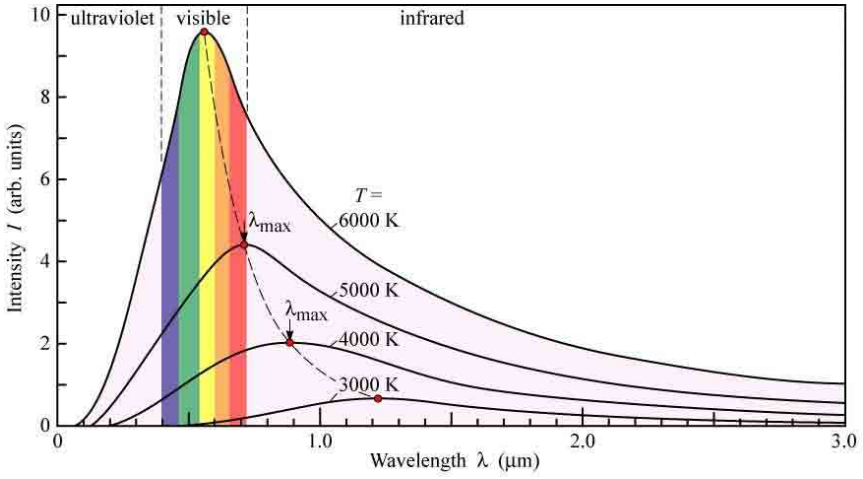

Figure 2.1 – *Planck's black body radiation curves for different temperatures*

Planck's law is illustrated in the figure 2.1. For a given temperature, there is a maximum in the energy distribution. The corresponding wavelength is governed by the Wien's displacement law describing the location of the maximum in the hemispherical spectral emissive power :

$$\lambda_{max} = \frac{b}{T}[m]$$

with $b = 2.897\ 10^{-3}\ [m\ K]$.

All these formulas concerned the black-body which is idealized object absorbing all radiant energy from any direction or wavelength and emitting in any direction isotropically. The radiated energy of the black-body only depends on its temperature. But a real body can absorb, reflect and transmit radiation energy so that absorptivity α, transmittivity τ and reflectivity ρ quantities are defined, all wavelength and angular dependent. For a semi-transparent body, energy conservation leads to the following equality

$$\alpha(\theta, \lambda) + \rho(\theta, \lambda) + \tau(\theta, \lambda) = 1$$

where θ is the angle of incidence. As there is no perfect black-body in practice, the emissivity $\epsilon(\lambda)$ is defined as the ratio between the energy emitted by a surface to that of a black body at the same temperature. Absorptivity and emissivity can either be hemispherical or directional and either total or spectral. The second Kirchhoff's law states that for a given direction θ, directional spectral absorptivity and emissivity are equal :

$$\epsilon(\theta, \lambda) = \alpha(\theta, \lambda)$$

But, in general, this is not true with total hemispherical values mainly because of their strong wavelength dependence. Both α ans ϵ varies with the angle of incidence but they are assumed to follow the Lambert's law stating that directional absorptivity/emissivity is proportional to $\cos\theta$ (maximum for normal incident angles and null for tangential ones). The reflectivity can be either diffuse or specular ($\rho = \rho_d + \rho_s$). When diffuse, it follows the Lambert's law as the emissivity and absorptivity while specular reflection follows Descartes' law according to which the reflexion angle is equal the the incident angle.

In space heat transfer, thermal engineers made the following assumption : thermo-optical properties are assumed to be constant in two spectral regions :

- the infrared spectrum, from $\lambda = 4.25\mu m$ to $40\mu m$, corresponding to temperatures between 70K and 700K.
- the visible spectrum, ranging from $\lambda = 0.3\mu m$ to $2.5\mu m$ associated to a temperature range going from 1150K to 10000K

As the temperature of a spacecraft lies in the 70K-700K range, the emitted radiation is infrared. But the source of the main incident radiation is the sun which can be considered as a blackbody emitting at 5776K. This temperature lies in the visible spectrum, as it is also shown by the figure 2.1. Actually, ESA and NASA thermal engineers adopted the following convention : they call ϵ the (constant) emissivity (and absorptivity) in infrared wavelengths and α the (constant) absorptivity (and emissivity) in visible wavelengths. This convention will also be adopted in this work.

Finally, surface thermo-optical properties are defined through eight coefficients (6 independent) related by the two following equations :

$$\epsilon + \rho_{IR,d} + \rho_{IR,s} + \tau_{IR} = 1 \quad \alpha + \rho_{VIS,d} + \rho_{VIS,s} + \tau_{VIS} = 1$$

Where τ is the transitivity An important concept for radiative exchange is the view factor $F_{(i,j)}$ between two surfaces S_i and S_j. It is the proportion of all the radiative power leaving S_i which directly strikes surface S_j (without any reflection) and only depends on the geometrical configuration :

$$F_{i,j} := \frac{P_{ij}}{P_i} = \frac{1}{\pi S_i} \int_{S_i} \int_{S_j} \frac{\cos\theta_i \cos\theta_j}{r_{ij}^2} dS_i dS_j$$

Another useful concept is the Gebhart factor B_{ij} : this factor takes into account multiple reflections and represents the portion of the radiation emitted by a surface S_i and finally incoming to the surface S_j. The Gebhart factor does not only depends on geometry but also on thermo-optical

properties. It is defined through the following equation, valid for diffuse reflection[1] :

$$B_{ij} = F_{ij}\epsilon_j + \sum_k F_{ik}(1-\epsilon_k)B_{kj}$$

The radiative coupling between two surfaces is directly deduced from the Gebhart factor. Indeed, the radiative power Q_{ij} flowing from S_i to S_j is equal to the difference between the power emitted by S_i, absorbed by S_j ($\epsilon_i S_i B_{ij}\sigma T_i^4$) and the one emitted by S_j and absorbed by S_i ($\epsilon_j S_j B_{ji}\sigma T_i^4$). At equilibrium, $Q_{ij} = 0$ and thus $\epsilon_i S_i B_{ij} = \epsilon_j S_j B_{ji}$. Out of equilibrium :

$$Q_{ij} = \epsilon_i S_i B_{ij}\sigma T_i^4 - \epsilon_j S_j B_{ji}\sigma T_i^4 = \epsilon_i S_i B_{ij}\sigma(T_i^4 - T_j^4) = GR_{(i,j)}\sigma(T_i^4 - T_j^4)$$

This defines the radiative exchange factor $GR_{(i,j)}$ between two surfaces i and j.

2.2 The thermal environment

A satellite orbiting Earth has several heat sources, as represented on the figure 2.2 :

1. Direct solar flux depending on sun distance, with a mean value around 1367 $[W/m^2]$ at 1AU (1414 $[W/m^2]$ at winter solstice and 1322 $[W/m^2]$ at summer solstice [24]).
2. Albedo planetary reflected radiation. For Earth, the mean reflectivity is assumed to be near 30%. But it can vary localy up to 40 or 80% above shiny clouds and from 5 to 10% for ocean and forests[44].
3. Earth infrared radiation. Earth can be modeled as an equivalent black-body emitting at 255 K [50], [44], [24].
4. Internal dissipated power in electronic components (Joule effect).
5. Not represented on the figure, aerothermal flux have also to be considered during launch or re-entry phases.

During the eclipse, only two heat sources are still present : Earth's infrared and internal dissipation and the spacecraft will be cooler. The temperatures of the satellite tend thus to vary in a cyclic way along the orbit, rising in sunshine and dropping during eclipse. The sky, called Deep Space, is the main source of cold and can be seen as a black body emitting at 3K. This temperature represent the radiation of the stars, the galaxies and the Cosmic Microwave Background which will be studied by ESA's new satellite Planck.

[1] A theory has been developed to take partial specular reflection into account [50] but will not be used in this work because the reflections encountered here are mainly diffuse

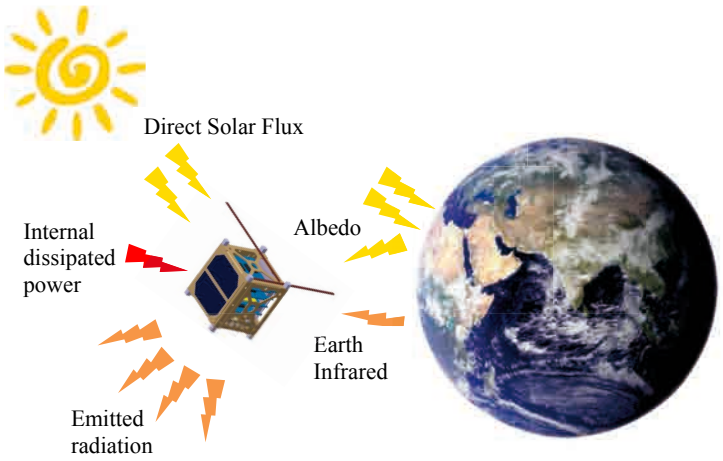

Figure 2.2 – *Thermal environment of a satellite in LEO*

2.3 Thus, why Thermal Control ? and how ?

The primary objective of thermal control is thus to maintain temperatures of onboard equipments within specified ranges, that will be later introduced for OUFTI-1. It also must ensure that temperature gradients (spatial consideration) are not too large and a good temperature stability (temporal consideration). Temperature gradients are undesirable for optics pointing and alignment while stability and thus narrow temperature ranges are important for the sensitivity of detectors. Therefore, the critical equipments usually are optical instruments and electronics components (mainly the batteries). For precise pointing satellites, thermo-elastic coupling involving unwanted vibrations also occurs at eclipse in and out : this is known as jitter phenomenon.

Then, how to fulfill all these requirements since the spacecraft undergoes temperature variation solely determined by its radiative exchanges with environment. In fact, there are two main categories of thermal control means : active and passive ones. This can be summarized in the following non exhaustive table :

Passive	**Radiation** - coating - MLI blanket - radiator **Latent heat & Ablation** - Thermal protection system - Phase change materials	**Conduction** - structural materials - doubler, filler, adhesive - washer, strap, bolt, stand-off
Active	**Heaters** - thermostat control - electronic control - ground control **Peltier element**	**Heat pipes & fluid loops** - fixed/variable conductance - loop heat pipe - mono/diphasic fluid **Louvres**

Table 2.1 – *Thermal control means*

Except for heaters, most of active means required too much power and mass or complex mechanisms and moving parts or even fluid packaging and this is not compatible with the CubeSat concept. Furthermore, even if active thermal control means are able to cope with larger heat loads, they are also generally less reliable than passive ones and CubeSats have usually low power consumption and dissipation. Nevertheless, if the temperature of an equipment dropped under its specified minimal one, a simple way of heating is the use of heaters. The advantage of heater is that it can nearly be of any dimension and is thus very convenient.

For all these reasons, the main and easiest way of doing thermal control for nanosatellites remains passive control or small heaters.

2.4 Thermal control systems of other CubeSats

This is indeed the means other CubeSat teams have used to do thermal control. Some of them are described below:

SwissCube

SwissCube nanosatellite [53] is developed at EPFL in Lausanne, Switzerland. SwissCube's mission is to study the nightglow phenomon. SwissCube has its own developed structure fabricated by CNC milling and wire electrical discharge machining and uses an active attitude control with magnetotorquers, sun sensors, gyroscopes and magnetometers to stabilize the satellite. Concerning the thermal control subsystem, their simulations led them to use a 500 mW (25 Ω) heater to keep the two batteries within their allowable range of temperatures. They are packed in an aluminum box to prevent deformation due to the vacuum environment and are fastened on a copper plate as the heater, all with epoxy resin. The copper plate is used because of its high thermal conductivity to conduct the generated heat to the batteries. The heater is thermostatically controlled avoiding the use of the OBC and is switched on under the 0°C threshold. SwissCube has not yet been launched but is ready for it.

Compass-1

Compass-1 [12] is developed by the students of the University of Applied Sciences in Aachen. Its mission is to take picture of the Earth and it has therefore a active attitude control as SwissCube. Their thermal model led them to use 2.01 W (68 Ω) heater located at the top of the battery box combined with LM75 temperature sensors. The heater is switched on once the temperature of the batteries drops under 5°C.

Compass-1 has already been launched on April, 28^{th}, 2008 by the Indian PSLV launcher. After the successful launch, Compass-1 entered in a vicious circle: the heater was too often switched on and the battery power drops drastically. This untimely switch on of the heater occurred because the temperature to which was compared the threshold was based on the minimal temperature given by the three sensor inside the battery box. The threshold has then been adapted but Compass-1 had to be reset for other reasons so that the nominal threshold had also been reset. Unfortunately,

they lost their two ground stations at that time but, with the help of the amateur radio community, they managed to recover the satellite and successfully changed into its nominal mode. Now, all goes well for Compass-1 and many pictures have already been taken.

Del -C^3

Delfi-C^3 [13] is the nanosatellite developed and has been launched with Compass-1 in April 2008. In addition to be a 3-Unit CubeSat, on the contrary of both previous CubeSats, the particularity of Delfi-C^3 lies in the fact that it do not have any battery but deployable solar arrays. As the battery is usually the more critical component, Delfi-C^3 has no active thermal control and its thermal behavior relies only the thermo-optical properties of the outer surfaces.

Preliminary thermal analysis

3

A first analysis had already been developed in the Phase A study by S. Galli. That was a steady state model and it did not take into account the effect of satellite's thermal inertia. In this chapter, a single node transient model of the CubeSat will be implemented in Matlab Simulink environment.

This chapter will begin with a description of the notations and conventions that will be adopted not only in this preliminary analysis but also in the next chapters. Then, we will study the thermal environment and implement a general way to compute the different incoming fluxes. After that, the cyclic single node transient model will be introduced and first guesses of hot and cold case will be computed. A sensitivity analysis will also be performed.

3.1 Notations

Here are described the notations and conventions we will use throughout this work.

Concerning the reference frame, it will be the one used by the Structure and Configuration subsystem. It was shown on the exploded view[1] (figure 1.11) : its center is the geometric center of the CubeSat. The $+X$ direction will be perpendicular to the face where are fixed the antennas and where the access ports are located and oriented to the opposite face, the $+Z$ direction will be the direction perpendicular to PCBs stack, from bottom with the OBC PCB to top with the COM PCB. Finally, the $+Y$ direction is such as it forms with the other ones a right handed coordinate system. We will also use the following numbering convention :

- $+X = 1$ & $-X = 4$
- $+Y = 2$ & $-Y = 5$
- $+Z = 3$ & $-Z = 6$

Concerning thermo-optical properties, ESA and NASA convention will also be adopted, as described previously :

$$\alpha = \alpha_{vis} = \epsilon_{vis}$$

[1] Excepted that it is not located at the center of the CubeSat for the sake of clarity

$$\epsilon = \epsilon_{IR} = \alpha_{IR}$$

Environmental fluxes notation will be as follows :

Q_S Solar power
Q_A Albedo power
Q_E Earth infrared power
Q_I Internal dissipated power

3.2 Thermal Requirements

As explained in the previous chapter, the aim of thermal control is to ensure that all onboard units will be working within their own allowable temperature range. All electronic components are not yet defined but the use COTS components mainly involves -40...+85°C temperature ranges. For instance, this is the case for Pumpkin's FM430 Flight Module (OBC), following its datasheet [48], and also for the PIC18F2331 microcontroller used on the experimental EPS [37]. Concerning COM PCB integrated circuits, the ADF7021 transceiver has also the same wide temperature range [5]. A more critical component was the oscillator because of its important temperature sensitivity. To avoid this potential problem, the use of a TCXO (Temperature Compensated Quartz Oscillator) has been foreseen. In this case, common TCXOs have the same temperature range.

The CubeSat Kit's, as all the previous parts, also operates in the -40°C to +85°C industrial temperatures range [47]. Typical values for solar cells operating temperature ranges are -100 to +100°C [62].

Finally, the most critical part of the satellite remains the batteries. Lithium polymer batteries have been chosen for their high specific capacity. The final model is not yet determined but, among the possible foreseen models (VARTA PoLiFlex® [58] and Kokam™SLPB 554374H [31]), all have the same specifications depending on whether it is in charge, from 0 to +45°C, or discharge, from -20 to +60°C.

OUFTI-1 thermal requirements are summarized in the table 3.1.

Component	T_{min} [°C]	T_{max} [°C]	Note
Main structure	-40	+85	
Solar cells	-100	+100	
Electronics	-40	+85	
LiPo Batteries	0	45	charge
	-20	60	discharge

Table 3.1 – *OUFTI-1's Thermal Requirements*

Another thermal requirement concerns the thermal expansion of the structure. The main CubeSat Kit's structure is made of aluminum 5052H32 alloy and thus already satisfies the differential dilatation condition with the P-POD, also made of aluminum alloy (7075-T73). Concerning the panels supporting the solar cells, it was decided, in agreement with the Structure and Configuration subsystem, that aluminum would again be more suitable than CFRP for the same reason. Panels will indeed be glued on the main frame (for a reason already explained in a previous chapter), and minimize the difference between the thermal expansion coefficients of the

panels and the frame was a good way to reduce the shear stress inside the glue.

3.3 Thermal environment related to OUFTI-1's orbit

Now, the different incident fluxes exposed in the previous chapter will be calculated. To do so, a simple Simulink Model will be developed in order to integrate the equations of motions of the two-body problem and compute the position of the satellite required for the fluxes calculation.

3.3.1 The orbit

An orbit is described by its classical orbital elements (COE aka Keplerian elements) : the semi-major axis a, the eccentricity e, the inclination i, the right ascension of the ascending node Ω or RAAN, the argument of perigee ω and the true anomaly ν.

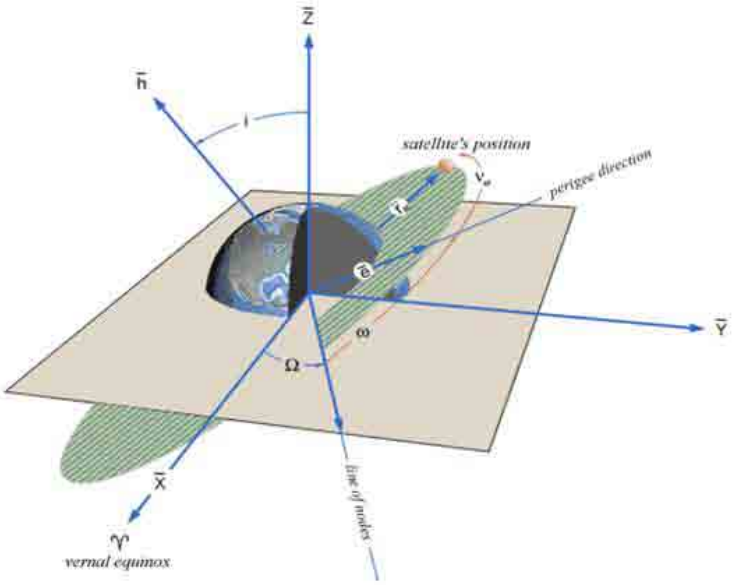

Figure 3.1 – *Classical orbital elements*

The reference line for the RAAN is taken as the vernal equinox, i.e. the intersection of the equatorial plane with the ecliptic at vernal equinox pointing directly to the sun. OUFTI-1's orbit has a perigee altitude of 354km, an apogee altitude of 1447km and an inclination of 71°. The two remaining parameters, the RAAN and perigee argument ω, are still unknown.

To compute the satellite position around the earth, a simple Simulink two body model has been derived. Initial position and velocity computed from the COE are given as input to the Simulink 6DoF Euler Angles integrator in addition to the acceleration given by equation 3.1:

$$\vec{a} = -\frac{\mu}{r^3}\vec{r} \tag{3.1}$$

where μ is the standard gravitational parameter of the earth and $\vec{r}$ the position vector of the satellite. An approximate attitude is given by the mean of initial euler angles and rotation rate of the satellite. The rotation rates of the satellite will remain constant as we consider that no moment act on it. As output, the integrator gives the position and direct cosine matrix (DCM) for the next time step. The DCM represents the current orientation of the satellite compared to the inertial axes, i.e. it is the rotation matrix to pass from the inertial coordinate frame to the body axes.

Then, at each time step, the model compute the incident heat flux on each face of the satellite. This is done in the *Albedo and IR calculation* box described in the next paragraphs.

3.3.2 Solar flux

As the sun distance is extremely large, the rays coming from the sun are assumed to be parallel. Furthermore, seeing the cubic shape of the satellite, there is no coupling between the faces, i.e. any ray that is reflected by one face will never hit another face. Therefore, the incident flux on each face is simply obtained by multiplying the solar constant C_S with the scalar product between the normal to the face and the sun direction.

$$q_{S,i} = C_S(\vec{n}_i \cdot \vec{r}_{sun}) \ [W/m^2]$$

The incident solar flux on each face is thus directly determined by the direct cosine matrix (DCM) and only depends on the solar constant C_S and the satellite attitude.

But how to know whether the spacecraft is in sunlight? The same method as the one implemented by V. Beukelaers in the Simulator was used: the Line-Of-Sight (LOS) method, developed by Alfano in 1991, described in [56]. This method is based on determining if the line between the satellite and the sun intersects the Earth : if it does, there is no LOS and the satellite is in eclipse and in all other cases it is in sunlight. The advantage of this method is that it avoids trigonometric operations. For further details, refer to [56] and [9].

The sun direction will be taken as a constant and equal to $\vec{r}_{sun} = [1\ 0\ 0]$. This means that if the inclination is 90°, the orbital plane will be perpendicular to the sun rays if $\Omega = 90°$and parallel for $\Omega = 0°$.

3.3.3 Albedo flux

The albedo flux is relatively more complex to evaluate. Indeed, it depends on many parameters such as satellite's position from the subsolar point, Earth view factor and many others. Many different expressions or tables can be found in the literature to compute the albedo but they are often not easy to use or incomplete. For that reason, we decided to combine two references : a simple formula coming from the notes of *"Contrôle thermique des engins spatiaux"*[1] by I. Alet and an abacus coming from the book *"Spacecraft Thermal Control Handbook"* by D. Gilmore [24].

Here is the formula and the abacus[1] is represented on the figure 3.3 :

[1] initially coming from Lockheed Martin

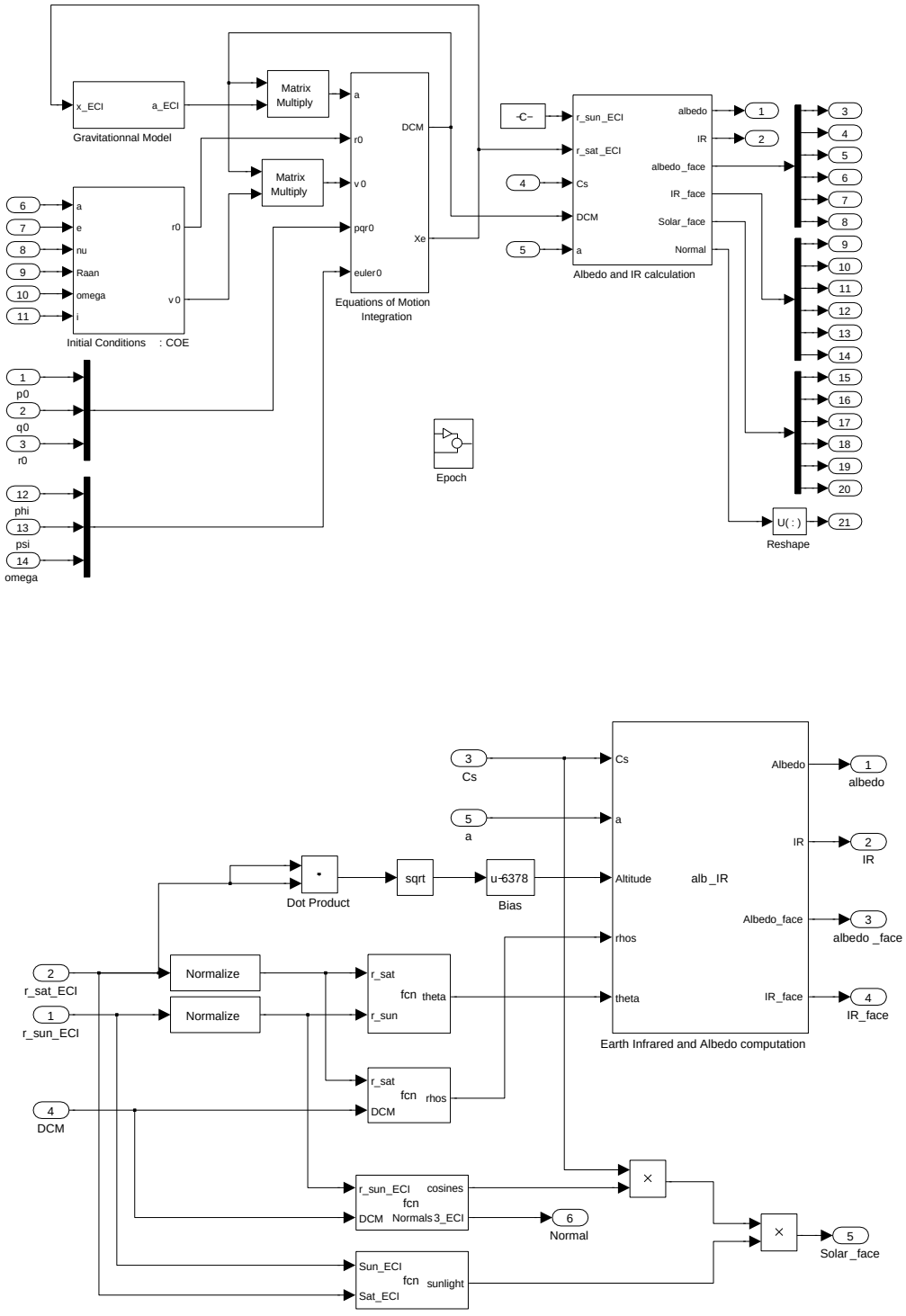

Figure 3.2 – *Simulink two-body propagator for incident ux computation : main window (top) and Albedo and IR calculation box (bottom)*

$$q_A = C_S a \left[\cos(0.9\,\theta)\right]^{1.5} F_E \; [W/m^2]$$

where C_S is the solar constant, a the albedo reflectivity coefficient, θ the "sun-earth-satellite" angle and F_E the view factor between the face and the earth. The 0.9 coefficient in the cosine means that even if the satellite has just come above the shadow part of the Earth, reflected rays are still hitting the satellite. When $\theta = 0$, the satellite is at the subsolar point and the albedo is maximum.

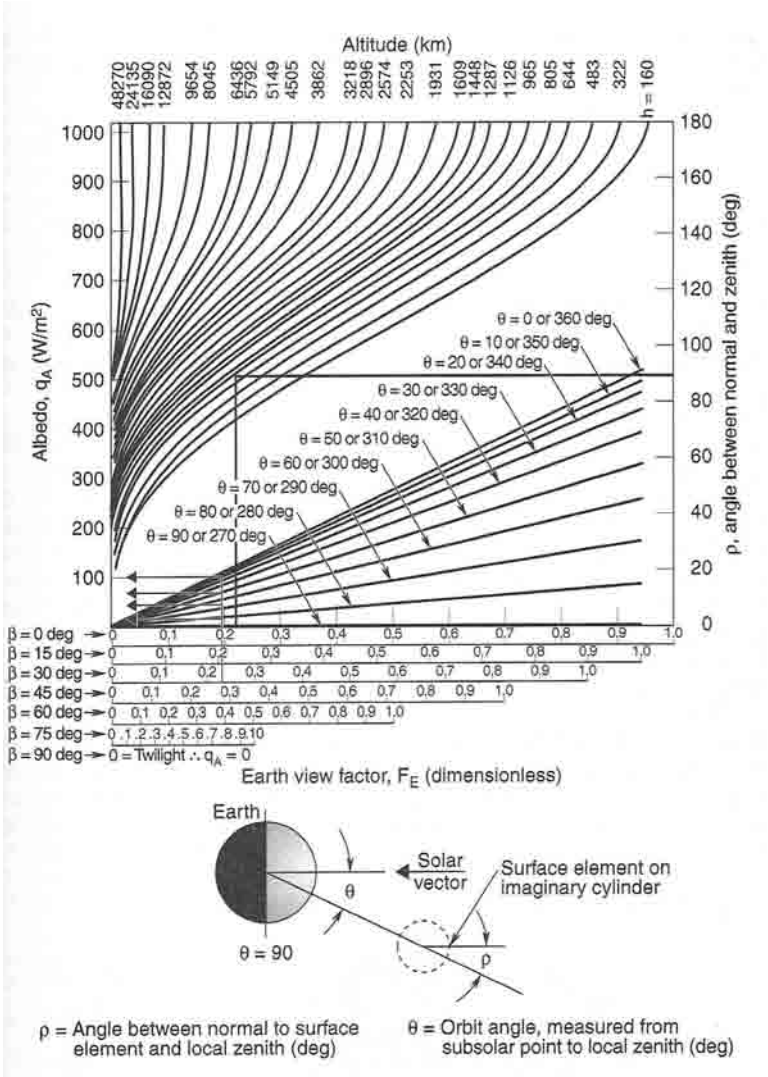

Figure 3.3 – *Incident albedo irradiation on a surface element in Earth orbit [24]*

The formula required to compute the view factor between the face and the earth, F_E which is quite difficult since it depends both on the altitude and orientation of the face. But, even if this view factor can be easily hand computed with the abacus, this is no more easy to implement within Matlab. Therefore, all these curves were digitized and, to simplify their use, fitted with this formula :

$$F_E = r^{2.1} \left[\sin\left(\frac{\rho}{2}\right)\right]^e \tag{3.2}$$

with the exponent e described as a function of r:

$$e = -160.31r^6 + 723.36r^5 - 1380r^4 + 1394.6r^3 - 780.65r^2 + 226.81r - 21.232$$

where $r = \frac{R_\oplus}{R_\oplus + h}$. The fitting approximation of the view factor F_E is represented on the figure 3.4, in comparison with the Lockheed Martin abacus.

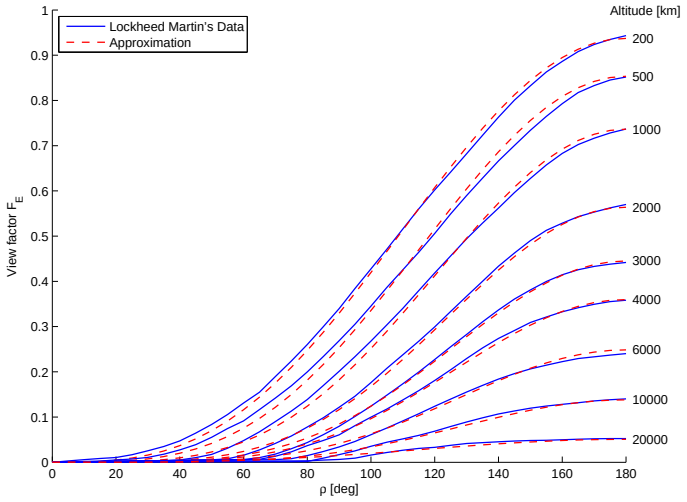

Figure 3.4 – *Fitting of the Gilmore abacus curves with the formula 3.2*

The equation and the abacus show that even if the scalar product $\vec{n}_{face} \cdot -\vec{r}_{sat}$ is negative (i.e. $\rho < 90\ deg$ and the face does not point directly toward the Earth), the view factor is not null and the face still absorbs albedo or infrared flux. This can be explained by the fact that the incoming rays are no more parallel as it was the case for the sun rays since the satellite is close to the emitting body that can no more be considered as a point. This feature will involve a greater effective surface as it will be shown.

Of course, the combined model has been correlated with the abacus method. This albedo model does not take into account local reflectivity variation (clouds, forests, oceans...)

3.3.4 Earth infrared flux

Earth's infrared flux, also depending on the same F_E is now easier to compute since F_E is already known. By neglecting diurnal and seasonal variation in the temperatures of the earth and considering it as an equivalent 255K black body (thus emitting diffusely in all directions), one can obtain the following equation :

$$q_E = E_{BB\ T=255K}\, F_E = 240\ F_E \quad [W/m^2]$$

3.3.5 Aerothermal flux

For a circular orbit, the aerothermal flux decrease with the altitude from $1300W/m^2$ at 150km to 160 then $39W/m^2$ at 200 and 250 km. The remaining aerothermal flux at 350 km is only $7W/m^2$. This contribution will then be neglected throughout this work.

3.3.6 Results

Using this model, we are now able to represent the fluxes seen by the satellite on its orbit. In Figure 3.5 is plotted the nominal Earth IR and albedo fluxes incident to a unit surface pointing toward the Earth ($\rho = 180°$), on OUFTI-1's orbit, $\Omega = 0°$(line of nodes perpendicular to the sun vector), $\omega = 0°$.

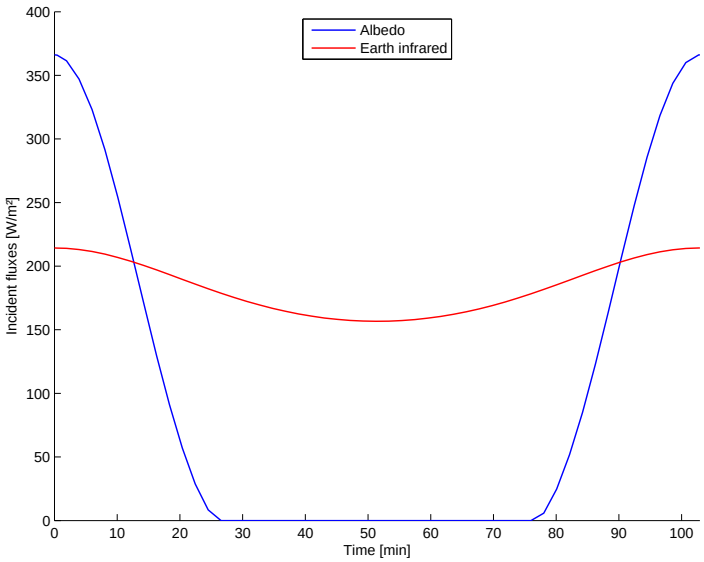

Figure 3.5 – *Nominal Earth IR and Albedo uxes seen by a surface pointing to the Earth on OUFTI-1's orbit*

But it has already been noticed that when the satellite is close to the earth, unless a face points perfectly away from the Earth, all the six faces have a non zero view factor F_E. This means that an effective area can be defined as the area pointing toward the Earth that would receive the same flux as the sum of all the faces.

$$A_{eff} = \frac{1}{q_{nom}} \sum_{i}^{n_{faces}} A_i q_i = \frac{A}{q_{nom}} \sum_{i}^{n_{faces}} q_i \qquad \frac{A_{eff}}{A} = \frac{1}{q_{nom}} \sum_{i}^{n_{faces}} q_i$$

The figure 3.6 shows this. The CubeSat is initially oriented in such a way that its great diagonal is parallel to the local zenith. For this position, all the six faces have a non-zero incident flux and that the effective area ratio (ratio between the effective area and a cube's face) is greater than 2 !

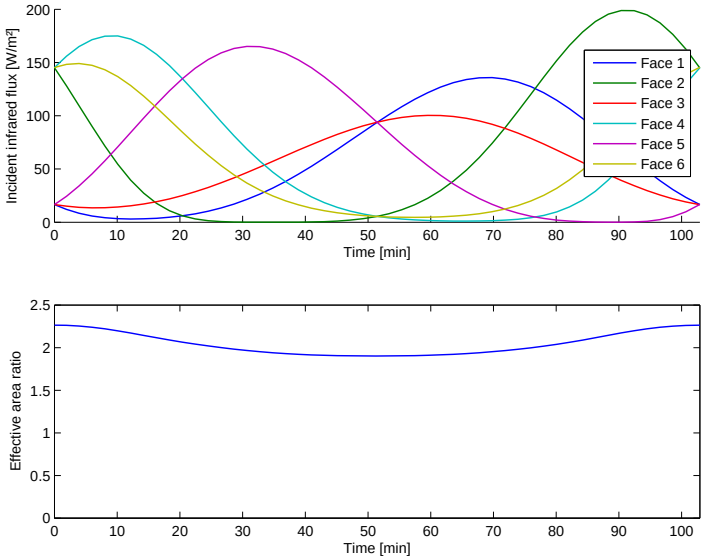

Figure 3.6 – *Infrared uxes incident on each face and effective area ratio*

The case of a randomly spinning CubeSat is represented in Figure 3.7. The effective area ratio does not significantly change and this is the same for albedo and IR. The conclusion is that the spin rate of the CubeSat does not significantly affect the effective area ratio related to IR and Albedo for LEO.

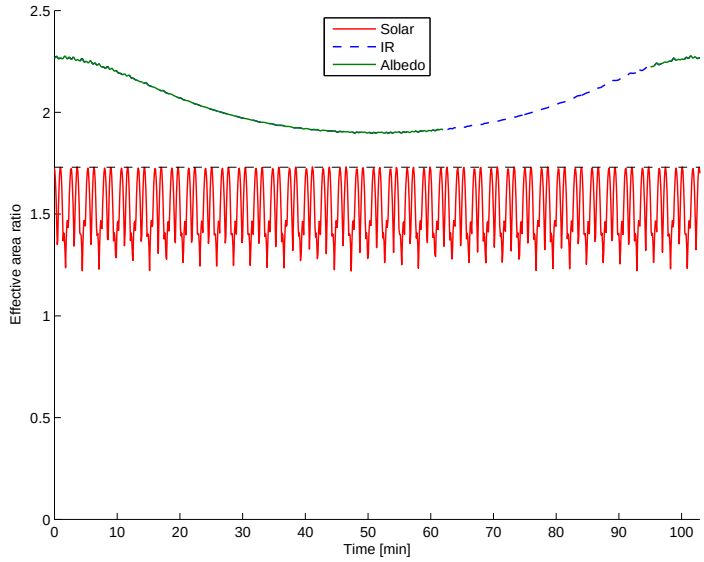

Figure 3.7 – *Effective area ratio*

On another hand, the effective area ratio related the solar flux never exceeds the theoretical value of $\overline{3}$, corresponding to the case when the

great diagonal is pointing to the sun (the projected area is $\overline{3}$ times greater than the cube's face area).

3.4 Cyclic Transient Model

Now that the incident fluxes on each face can be computed, the temperature must be computed. For this preliminary analysis, a very simple model has been created. It is based on only one node for all the satellite (so considered isothermal) but taking transient effects into account.

3.4.1 Implementation

The basic underlying equation used for this model is the lumped parameter equation, written here under its general form for a transient multiple nodes model :

$$Qint_i + Qext_i + \sum_{j=1,j=i}^{n} GL_{i,j}\,(T_i - T_j) + \sigma \sum_{j=1,j=i}^{n} GR_{i,j}\,(T_i^4 - T_j^4) = C_i \frac{dT_i}{dt} \tag{3.3}$$

$Qint_i$ the total internal dissipated power for the node i, $Qext_i$ the total external power incoming on the node i ($Qext_i = QS_i + QA_i + QE_i$), $GL_{i,j}$ and $GR_{i,j}$ are respectively the conductive and radiative links between nodes i and j. T_i is the temperature of the node i and C_i its heat capacity. This equation results from the heat balance to node i.

For a single node model, it reduces to :

$$Qint + Qext + \sigma GR_{sat,DS}\,(T_{sat}^4 - T_{DS}^4) = C \frac{dT_{sat}}{dt}$$

where $GR_{sat,DS}$ is the radiative exchange factor between the satellite and the Deep Space and $T_{DS} = 3K$ the Deep Space temperature. As there is no coupling between the faces of the cube, $GR_{sat,DS}$ is simply equal to the product of the CubeSat's total area by its averaged emissivity :

$$\epsilon_{eq} = \frac{\sum_i A_i \epsilon_i}{\sum_i A_i}$$

Concerning $Qext$, the heat flux incident on face i are simply multiplied by its corresponding equivalent absorptivity/emissivity (α for solar and albedo and ϵ for IR) and then added:

$$Qext = QS + QA + QE = \sum_{i}^{n_{faces}} A_i\,(\alpha_i q_{S,i} + \alpha_i q_{A,i} + \epsilon_i q_{E,i})$$

The cyclic transient solver is implemented in Matlab/Simulink environment. The solver is made up two main consecutive phases : a first one calculating the external incident fluxes around the orbit in Simulink (already developed and represented at the figure 3.2) and a second one integrating the lumped parameter equation. Once the first phase is completed and the external absorbed power is known for each face and at each position around the orbit, the equation 3.3 is integrated over one orbit several times. By this way, after a finite number of orbit integrations,

the temperature evolution over one orbit does not depend anymore on the first initial condition. The process is summed up in the flow chart of the figure 3.8.

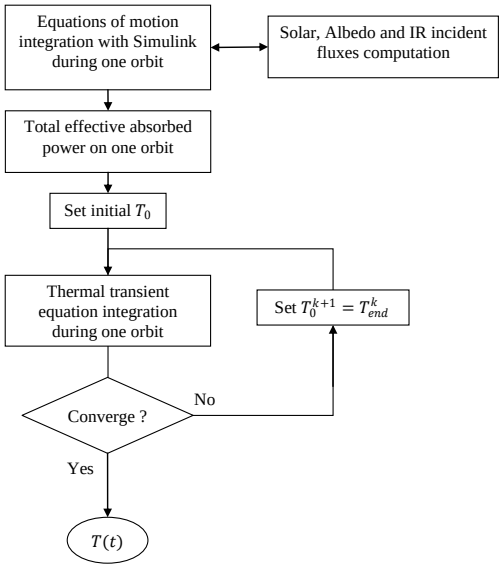

Figure 3.8 – *Cyclic transient Matlab Simulink solver ow chart*

The cyclic repetition of the temperature evolution is based on two convergence criteria.

1. The temperature reached at the end of one orbit must be equal to the temperature at the beginning of this orbit. If they are not equal, the initial condition of the $(k+1)^{th}$ orbit integration is updated with the final temperature of the previous orbit.

$$\left\| T_{t=0}^k - T_{t=T_{orbit}}^k \right\| < tol_T$$

   where T_{orbit} is the period of the orbit.

2. The time derivative of the temperature at the beginning and at the end of one orbit must be equal.

$$\left\| \left. \frac{dT^k}{dt} \right|_{t=0} - \left. \frac{dT^k}{dt} \right|_{t=T_{orbit}} \right\| < tol_{dT}$$

In practice, the Runge-Kutta algorithm (`ode45` in Matlab) is used to solve the non linear differential equation over the orbit period. If the convergence criteria are not satisfied, the initial temperature of the next orbit is set as the final one of the previous orbit, as described in the flow chart.

3.4.2 Validation

Before running and analyzing the model, it has been correlated with ESATAN/ESARAD softwares. The validation is performed for a non-rotating cube pointing toward the sun on OUFTI-1's orbit ($354 \times 1447km \times$

71°), with a RAAN $\Omega = 45°$, and a perigee argument $\omega = 0°$. The cube is considered as a perfect black-body ($\alpha = \epsilon = 1$). To evaluate its heat capacity, the heat capacities of OUFTI-1's main components[1] have been added. The different contribution are exposed in the table 3.2.

Component	Mass [g]	Specific Heat [J/kgK]	Heat capacity [J/K]
aluminum frame	145	980	142.1
aluminum panels	165	980	161.7
PCBs	350	1136	397.6
Antenna panel	33	980	32.3
Batteries	50	960	42.3
Total	≈698		776

Table 3.2 – *OUFTI-1s thermal heat capacity*

The figure 3.9, shows that both temperature and flux are identical with the two solvers and that the Matlab/Simulink one is valid.

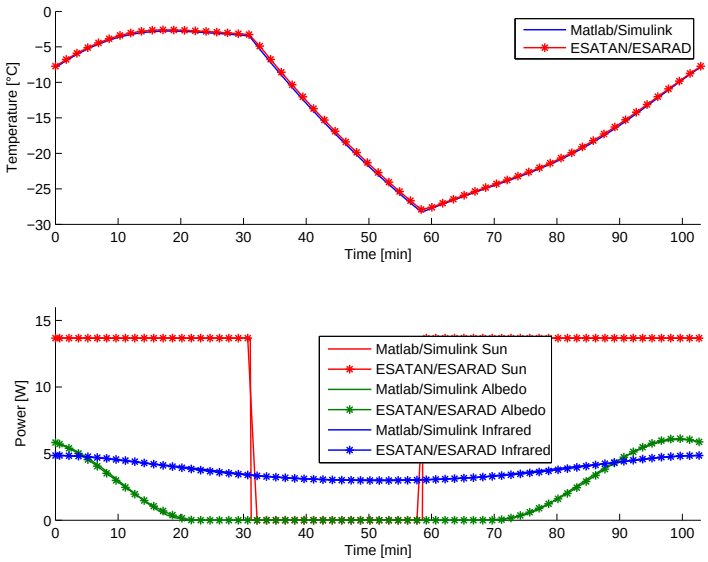

Figure 3.9 – *Validation of the cyclic transient Matlab/Simulink solver with ESATAN/ESARAD*

3.5 Results

Now that one can convincingly compute the mean temperature of the CubeSat for given thermo-optical properties and orbit, it is time to briefly

[1] All materials properties data comes from CES EduPack. CES EduPack, created by Professor Mike Ashby of Cambridge University, is a very useful tool for materials selection, containing an impressive database of materials and process properties.

introduce the concept of cold and hot case, as it will be reused many times throughout this work. It is based on a worst case conservative study :

- the hot case corresponds the case for which all parameters, both environmental and satellite related, are chosen in such a way that they all contribute to reach maximal temperatures and/or gradients during one orbit. For instance, considering the solar constant at the winter solstice (1414 $[W/m^2]$) instead of the mean value 1367 $[W/m^2]$ or a higher albedo coefficient or even a particular orbit (as the orbit changes over time).
- On the contrary, the cold case is the perfect opposite of the hot case: all parameters are such as the reached temperature is minimal.

The parameters that are biased hot or cold are:

- Emissivity and Absorptivity
- Environmental Constants (Solar, Albedo, IR)
- Spacecraft Orbital Orientation
- Internal Power Dissipation

External surfaces emissivity/absorptivity values are not perfectly known and vary throughout the lifetime of the spacecraft (mainly an increase for α due to high reactive atomic oxygen present in the upper layers of the atmosphere) and are therefore subjected to the cold/hot case definition. The concept of Beginning of Life (BOL) and End of Life (EOL) values is then useful. As the emissivity does not suffer great variation over time while the absorptivity tends to increase, BOL values are considered for the cold case analysis and EOL for the hot case. But at this point, as these values are not yet perfectly knows and defined, this effect will not be taken into account. A sensitivity analysis will be performed to see the relative importance of each thermo-optical property.

The cold and hot case assumptions are summarized in the following table 3.3:

Parameter	Hot Case	Cold Case
Orbital parameters	permanently illuminated	max eclipse time
Solar constant	1414 $[W/m^2]$	1322 $[W/m^2]$
Albedo coefficient	0.35	0.25
Earth temperature	250K (220$[W/m^2]$)	260K (260$[W/m^2]$)
Internal dissipation	full	none

Table 3.3 – *Preliminary Hot & Cold case definition*

As described in the table, for the cold case, all the electrical power collected by the solar cells is assumed to be perfectly stocked in the batteries without any dissipation. On the other hand, it is totally converted into heat in the hot case (cells' efficiency equal to zero). These are indeed the worst cases. One finally considers that the satellite is randomly rotating for both cases[1].

[1] ADCS simulations [25] shows that the satellite will never stop rotating because of the passive control and continuous perturbation torques acting on it

3.5.1 Hot Case

As explained above, the first hypothesis used for the hot case is a constantly illuminated orbit which is possible due to the high inclination of OUFTI-1's orbit : 71°. This means that the line of nodes, defined by the RAAN, is perpendicular to the direction of the sun. But in this situation, albedo is reduced because the satellite is continuously far from the subsolar point. One could wonder if an orbit containing the subsolar point with a minimum eclipse time (perigee in eclipse) could be more critical. The figure 3.10 shows the influence of the orbit orientation on the hot case temperatures evolution.

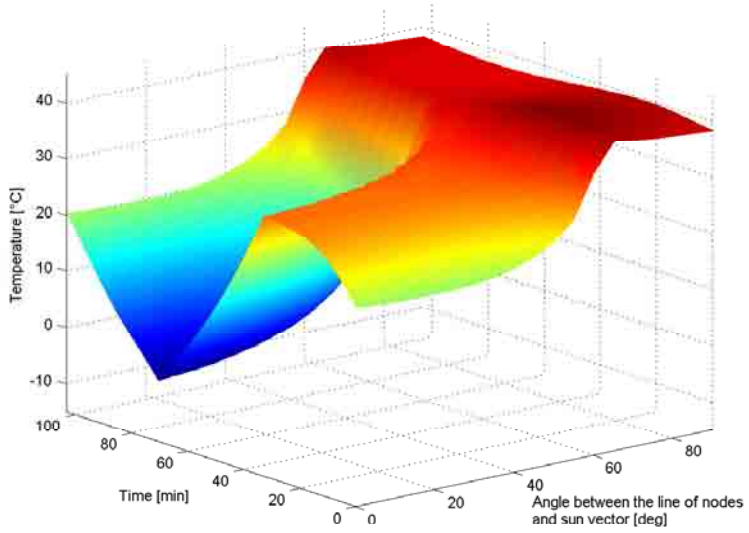

Figure 3.10 – *Hot Case definition, in uence of orbit orientation*

One can see that the lower the angle between the line of nodes and the sun direction, the lower the temperature reached. But there's an angle near 70°for which the satellite still experiences no eclipse and yet have a slightly higher albedo. This case would be slightly worst than the presupposed one but the difference is small and the hot case will still consider an orbit whose line of nodes is perpendicular to the sun's direction.

Recalling the maximal specified temperature of the batteries of 45°C, the mean temperature of the CubeSat in this preliminary hot case is already close to it and will thus be carefully looked at in the next analysis.

3.5.2 Cold Case

Here are the results of the cold case defined earlier. The temperature falls down to -20°C. This would represent the mean temperature of the CubeSat and one can imagine that external parts could still be cooler and internal parts slightly hotter. When the satellite comes out of eclipse, the batteries begins to charge and this analysis let us think that the batteries could be below their minimal specified temperature while charging: 0°C.

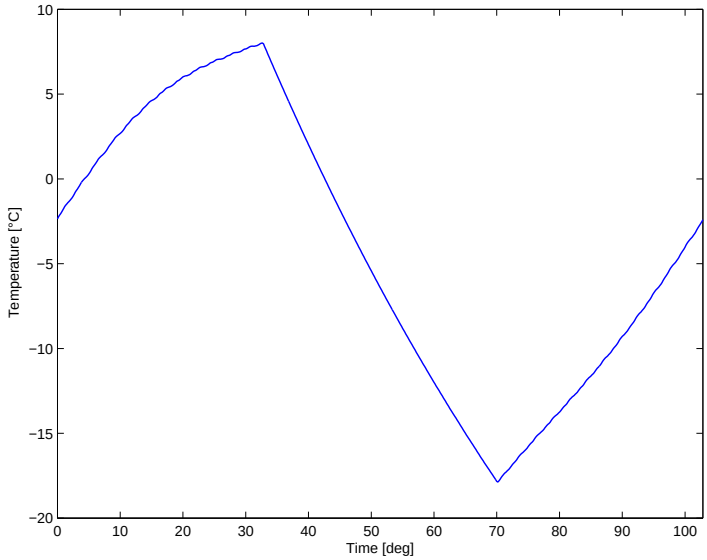

Figure 3.11 – *Cold Case temperature evolution*

3.6 Sensitivity analysis

Except for the solar cells, absorptivity/emissivity values are not yet well known. That's why, we carried out an evaluation of the sensitivity of the extremal temperatures to thermo-optical properties. One can already compute the area ratios of the different external materials of the CubeSat. The results are given in the table 3.4.

Component	Area [cm^2]	Ratio [%]
Solar cells	301.8	50.3
aluminum panels	107.2	17.9
Anodized rails	68	11.3
Remaining aluminum frame	65.6	10.9
Antenna deployment mechanism panel	57.4	9.6
Total area	600	100

Table 3.4 – *External area ratios*

The solar cells obviously fill the half of the total area of the CubeSat while the aluminum panels and rails cover 30% of the cube. The remaining 20% are divided up between the frame and antennas' panel.

To do so, we vary the α/ϵ values for each component separately and compute the minimal/maximal temperatures in the cold/hot case, T_{min} & T_{max}. For instance, the figure 3.12 represents the evolution of T_{min} & T_{max} for all combination α/ϵ of the aluminum panels.

Figure 3.12 shows that all the curves are nearly linear. Linearized sensitivities of the maximal and minimal temperatures of the CubeSat to the emissivity and absorptivity of the aluminum panel can thus be computed. The coefficients for the other surfaces are obtained by the same way: all

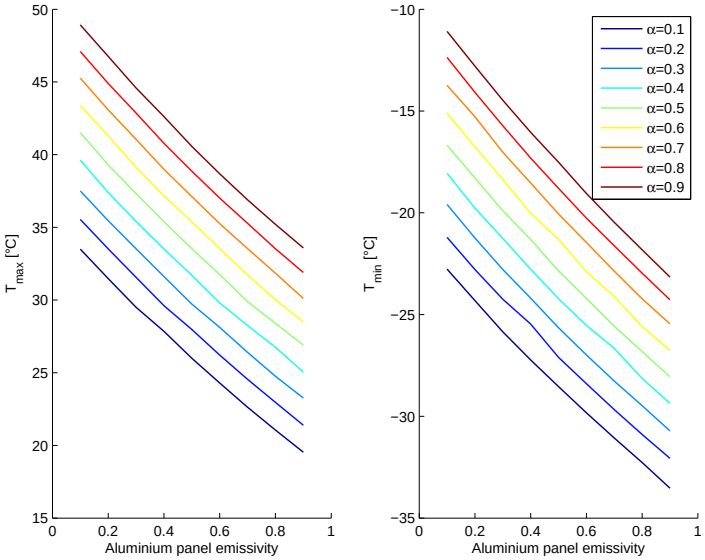

Figure 3.12 – *T_{max} & T_{min} sensitivity to aluminum panel thermo-optical properties*

the values are exposed in table 3.5. The value must be interpreted as the variation of the minimum/maximum temperature resulting from a 10% variation of the thermo-optical property. For instance, if the absorptivity of the rails increase(decrease) from 10%, the maximal temperature will decrease(increase) from 0.8°C.

	$\frac{dT_{max}}{d\epsilon} \times 0.1$	$\frac{dT_{min}}{d\epsilon} \times 0.1$	$\frac{dT_{max}}{d\alpha} \times 0.1$	$\frac{dT_{min}}{d\alpha} \times 0.1$
aluminum panels	-1.8	-1.4	1.8	1.4
Rails	-0.8	-0.6	1.0	0.8
aluminum frame	-1.0	-0.8	0.6	0.4
Antennas' panel	-0.9	-0.8	0.1	0.1

Table 3.5 – *Sensitivity coefficients to thermo optical properties*

It emerges that the aluminum panels properties have the more influence but that it yet remains relatively small.

3.7 Advanced Simulink Model

As presented in the introduction, V. Beukelaers, who is in charged of the MIAS subsystem, develops a global simulator in Matlab Simulink environment. Within this framework, a more detailed simulink thermal model has been developed. However, for the sake of conciseness, only its main features and results are presented. Each PCB and face has a dedicated node in addition to the batteries' node. The incident fluxes are computed though the same previously used module.

Figures 3.13 and 3.14 display the results for the hot and cold cases. The bottom plots show the evolution of the eclipse time while the two others

represent the evolution of the temperature of the PCBs and faces. Figure 3.13 shows the reduction of eclipse time and the resulting transient period lasting four to three orbits before the hot case is achieved.

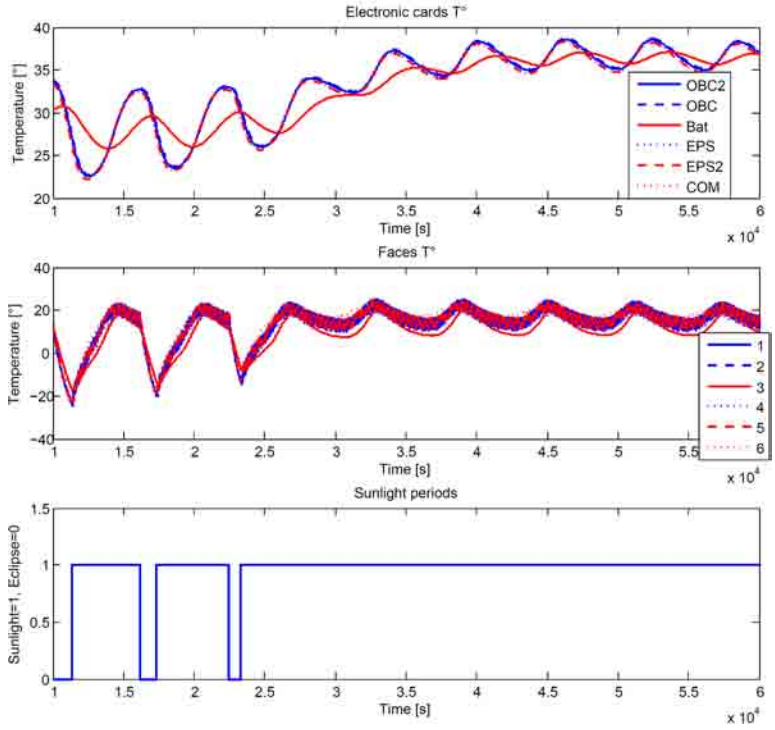

Figure 3.13 – *Advanced simulink thermal model hot case results*

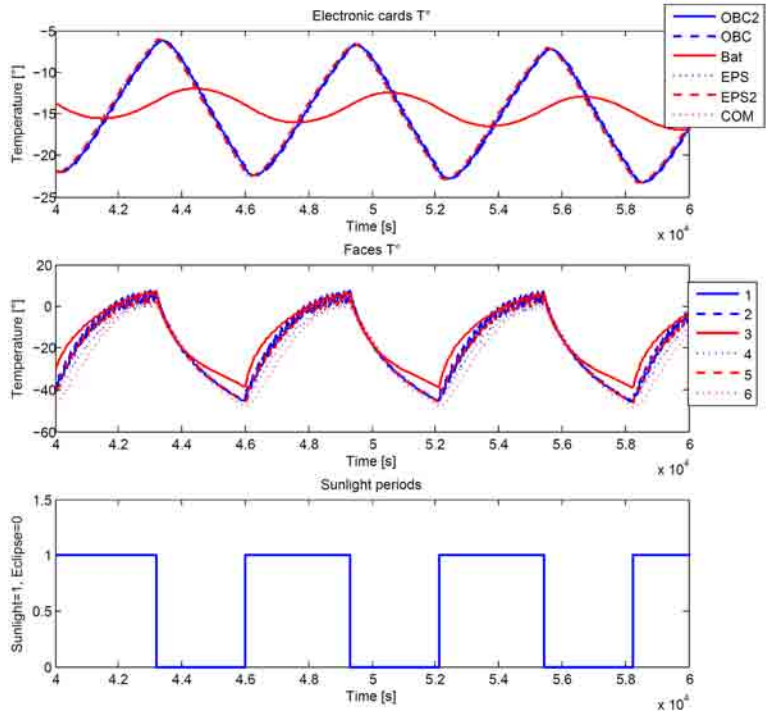

Figure 3.14 – *Advanced simulink thermal model cold case results*

Summary

The preliminary analysis already suggests that the battery, which has the narrower allowable temperature range, will be one of the key driver of the thermal design in the hot case as well as in the cold case. On another hand, hot spots could occur in the hot case but are not observable here. Moreover, the available surface area for thermal control coating is low and their individual effect on the extreme reached temperatures are quite small. However, accurate data about the optical-properties of the outer surfaces should be gathered

Simplified Thermal Model 4

After this first preliminary analysis, the use of ESATAN/ESARAD softwares seemed necessary even for the development of a simple multi-nodes model. This chapter includes a brief description of these softwares and thermal modeling. The particular modeling flow chart will be described. Then, it will be used for the creation of our first multi-nodes model, namely the Simplified Thermal Model (STM). The aim of this model is not to give accurate temperature distributions of PCBs but rather a first guess of the temperature of OUFTI-1's main units which was not available in the previous single-node model.

4.1 Thermal modeling with ESATAN & ESARAD

The global thermal analysis is performed in two stages : the radiative analysis and the thermal analysis. These two stages are performed respectively with ESARAD and ESATAN softwares, ESA's standard tools for thermal radiation and thermal analysis. It is based upon the lumped parameter method. The fundamental assumption is that it considers isothermal nodes in a thermal network (electrical analogy).

The global thermal model is thus divided up into two separated models with different purposes : the Geometric Mathematical Model (GMM) and the Thermal Mathematical Model (TMM). GMM's goal, created within ESARAD, is to compute the radiative coupling between its different nodes and the environmental thermal fluxes along the orbit which are then input into the TMM. The TMM includes conductive links and heat capacity and is solved within ESATAN to predict the temperatures of the spacecraft.

For our model creation, pre/post-processing is done in Matlab environment. This choice is motivated by relatively low parametrization of ESATAN/ESARAD models. GMM and TMM input files are written within Matlab, based on spacecraft and environmental data, all parametrized. ESARAD/ESATAN are then launched within Matlab, using batch mode, except for model checking. All output files are also post-processed within Matlab. By this way, parametric studies are easier to perform since all the process is Matlab controlled. Figure 4.1 shows the thermal model processing flow chart.

The conductive network links and nodal heat capacities are calculated by hand, based on material properties and geometrical configuration.

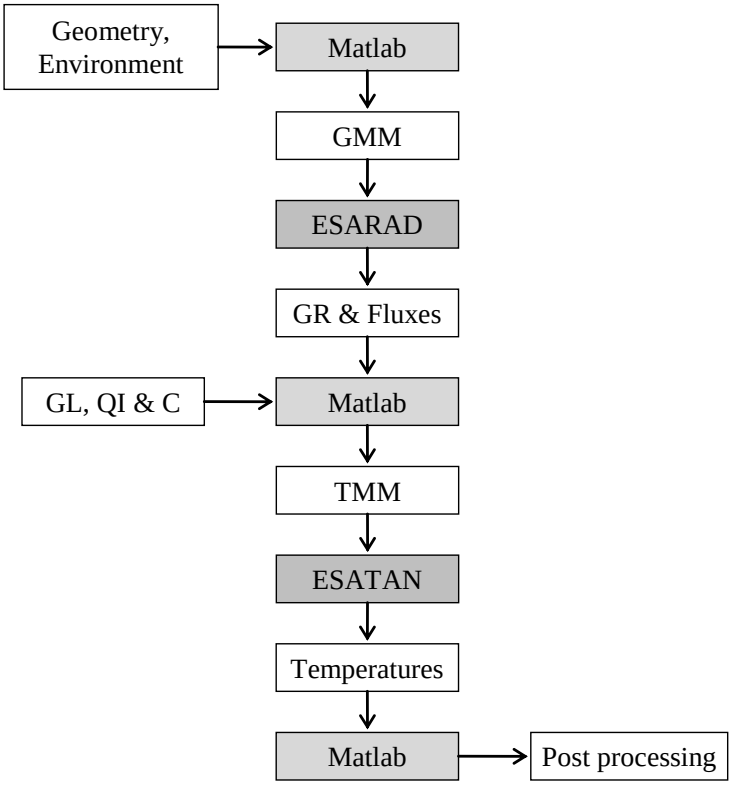

Figure 4.1 – *Thermal model processing ow chart*

4.2 Geometric Mathematical Model

4.2.1 Nodal breakdown

For a good understanding and easy interpretation of heat flow paths, this first multiple-nodes model remains relatively simple. It is made up of 18 nodes :

- One node per face : each face is considered as one node and so isothermal, for all face's *layers* except solar cells. We call *layer* the different elements constituting the face along its thickness: successively the aluminum frame, the aluminum panel and the solar cells. This is a relatively good assumption seeing the small thickness and high conductivity of aluminum. The glue is neglected.
- One node for each pair of solar cells (two per face).
- One node per PCB (OBC, OBC2, EPS, Batteries' PCB, EPS2, COM), representing the average temperature of the PCB.
- One node for the two batteries.

Here is the numbering convention adopted :

- i^{th} face solar cells	$10i$	$i = 1 \dots 6, i = 4$
- i^{th} Face	$30i$	$i = 1 \dots 6$
- OBC	10000	
- OBC2	12000	
- EPS	14000	
- BAT	15000	
- EPS2	16000	
- COM	18000	
- Batteries	20000	

Figure 4.2 illustrates the nodal breakdown and GMM. Spacers and PCB connectors have not been modelled, considered just as conductive links. Neglecting spacers is a good assumption seeing their low contribution in the radiative model (low area and low emissivity of aluminum) and low capacitance for the TMM. The assumption about the connectors is stronger : in the GMM, the view factors between face 5 and PCBs are artificially increased but as it will be shown, radiation inside the CubeSat is less influent than conduction. Nevertheless, their heat capacity will be taken into account and included to the PCBs.

4.2.2 Thermo-optical properties

Concerning thermo-optical properties, precise measurements are not affordable for a student project. Therefore, data have been collected from many sources and compared in order to choose the most realistic values as possible. Recall that the CubeSat's rails are hard anodized to prevent

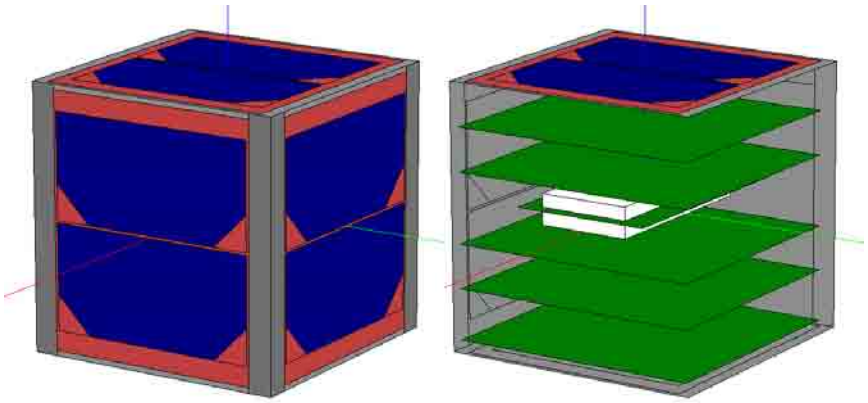

Figure 4.2 – *Geometric Mathematical Model nodal breakdown in ESARAD*

galling while the rest of the frame is alodyned to enhance electrical conductivity[1]. Both processes will be studied in details in the next chapter. aluminum panels' surface treatment is also Alodine (1200). For insulation reasons, solar cells have not been directly integrated on the panels but a Kapton® foil is used as insulator and completely covers the panels. Data for the kapton™ covered panels comes directly from EADS Astrium, who performed the solar cells integration on the aluminum panels, and did optical properties measurements of the integrated panels. Figure 4.3 shows the panels before and after solar cells integration.

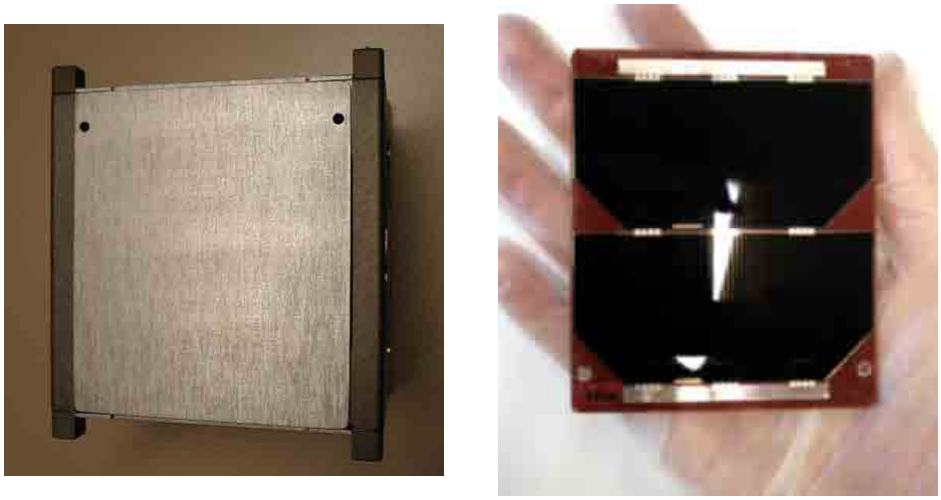

Figure 4.3 – *On the left, the CubeSat with one aluminum panel before integration. On the right, the panel integrated with the cells by EADS Astrium*

4.2.3 Orbit & attitude

As already said in the beginning of this work, OUFTI-1 is selected for the Vega Maiden Flight and the only defined orbital parameters are :

[1] According to Adam Reif from Pumpkin, the MIL-spec reference of the anodized process is MIL-A-8625F, TYPE III, CLASS 1 while the one of alodyned process is MIL-DTL-5541F Type II, CLASS 1A

Part	Material	Thermal finish	α	ϵ	reference(s)
aluminum frame	5052 aluminum alloy	Alodine	0.08	0.15	[27]
			0.08	0.15	[11]
			0.1	0.1	[57]
			0.08	0.15	[20]
aluminum frame rails	5052 aluminum alloy	Hard anodized	0.88	0.88	[24]
			0.86	0.86	[50]
			0.85	0.87	[49]
			0.86	0.86	[43]
aluminum panels, inside	7075 aluminum alloy	Alodine 1200	-	0.1	[45]
			-	0.08	[8]
			-	0.07	[43]
aluminum panels, outside	7075 aluminum alloy	2mil Kapton® foil on Alodine 1200	0.87	0.81	(a)
Solar cells	triple junction GaAs cells	anti reflective coating	0.91	0.81	(a), [7]
PCBs	FR4	-	-	0.8	[64]
Battery pack	plastic	-	-	0.8	[21]

Notes : (a) : EADS Astrium measurements

Table 4.1 – *Thermo Optical Properties*

- its apogee: 354 km,
- its perigee: 1447 km
- and its inclination: 71°.

Due to the telecommunication payload, the satellite does not require a precise attitude control so that this will be a passive one. As described in the ADCS subsystem presentation, a permanent magnet will be used to align the CubeSat on Earth's magnetic field and hysteretic materials to damp the remaining rotation energy.

In ESARAD, this attitude has been simplified by using a planet centered Local Orbit Coordinate System (LOCS), described on the figure 4.4. Within this coordinate system, as the orbit inclination is relatively high, the alignment on Earth's magnetic field is approximated by prescribing a constant rotation speed around y axis such as the CubeSat perform two revolutions during one orbit. The LOCS already performing one revolution along the orbit, the prescribed rotation rate is $\frac{360}{T}$ deg/sec where T is the period of the orbit.

4.2.4 Radiative coupling

The calculation of view factors and direct heat fluxes is performed in ESARAD by the Monte Carlo ray-tracing (MCRT), also used in realistic rendering. MCRT method is based on a statistical approach. For a perfect

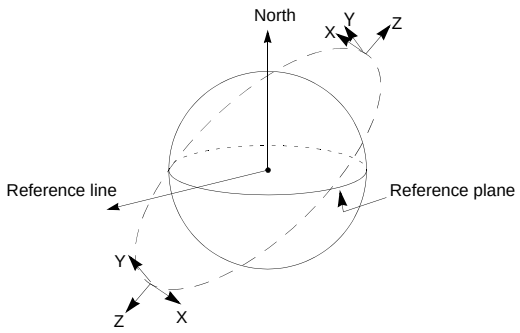

Figure 4.4 – *Planet centered Local Orbit Coordinate System (LOCS), from ESARAD User Manual*

accuracy, an infinite number of rays should be fired from each face since each ray has its own path, its own initial direction and may reach and be reflected by any other radiative face in the model. Firing and following the path of an infinity of rays is not possible. The statistical feature of MCRT comes from the estimation of the radiative couplings or heat fluxes made by averaging the results obtained from a finite random sample of rays.

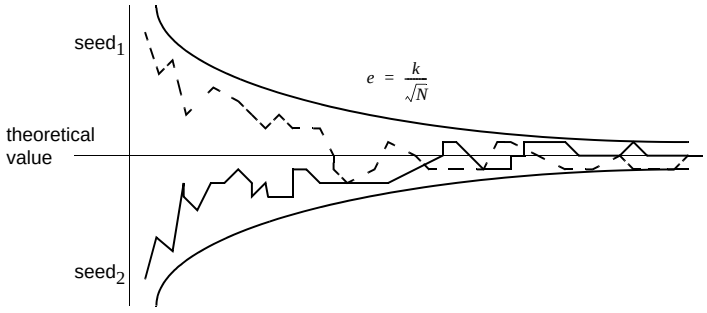

Figure 4.5 – *MCRT convergence from ESARAD user manual [2]*

The two control parameters of MCRT method are the number of rays fired from each face and the *seed*, a user input defining the pseudo-random initial distribution of rays' orientation. Due to the stochastic nature of MCRT, different seed values will lead to different results, as shown by Figure 4.5. However, the estimated value evolution goes randomly within a band whose width is inversely proportional to the square root of the number of rays fired. A disadvantage of MCRT method is that required calculation time increase as the face emissivity/absorptivity decrease since the rays are reflected more times before being absorbed.

This random evolution could lead to some mistakes and a convergence analysis was performed. Concerning our GMM, external faces have no radiative coupling so that environmental fluxes calculation does not require many rays. On another hand, figure 4.6 illustrates the convergence of the radiative exchange factor (REF) between the EPS PCB and face 1 for different seeds. By setting the number of rays to 10000 (or more), figure 4.6 shows that the relative error is about 1% (or below).

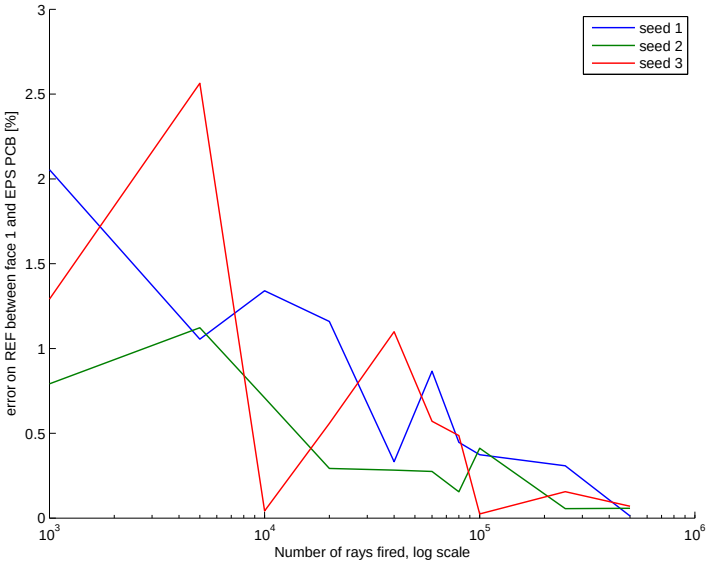

Figure 4.6 – *Radiative exchange factor convergence with number of rays fired (MCRT)*

4.3 Thermal Mathematical Model

Now that the GMM is defined and ready for computation, the second stage of the thermal analysis consist in the TMM creation. TMM involves conductive links network and nodal heat capacities definition and internal heat load distribution. These tasks are made by hand within Matlab and described for each group of nodes in the next paragraphs.

4.3.1 The structure

As previously described, each face of the CubeSat is modelled by one node. This means that temperature gradients inside a face are assumed to be low and therefore neglected : the face is considered isothermal. The conductive flow path between the faces only goes through the aluminum frame since there is no other contact. This is an approximation : the contribution of aluminum panels to the conductance between faces has been neglected. Seeing the relatively complex geometry of the frame, conductive links calculation is not immediate. Hence, for each of the 12 links, a finite element model has been created within SamcefField.

The method used is the following one : to compute the equivalent coductive link between two faces, each of them is cut in two in the middle, perpendicular to the flow path. A temperature gradient is imposed across the two half faces and SamcefField is then able to compute the resulting flux proportional to the temperature gradient. The equivalent conductance is easily deduced from $GL = \frac{Q}{\Delta T}$. Figure 4.7 shows the temperature distribution across the face 1 and 3 for a gradient of 10°C.

The 12 conductances are exposed in the table 4.2.

These values do not take into account the contact resistance in the links with faces 3 and 6. Contact results from the fact that faces 3 and 6

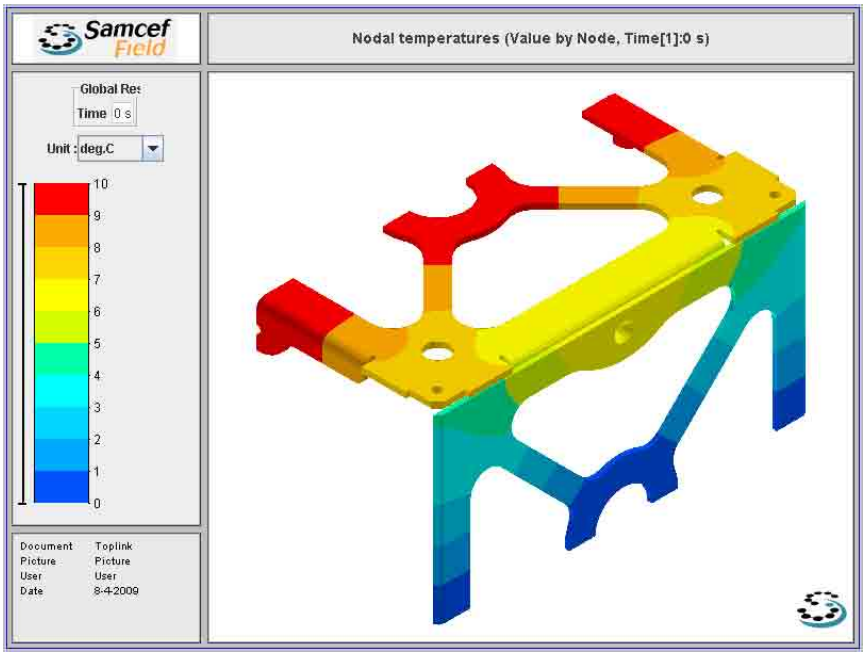

Figure 4.7 – *Evaluation of the conductive link of aluminum frame through a finite element analysis within SamcefField*

Faces	GL [W/K]	faces	GL [W/K]
GL_{12}	5.496×10^{-2}	GL_{26}	5.465×10^{-2}
GL_{13}	5.465×10^{-2}	GL_{34}	5.789×10^{-2}
GL_{15}	5.496×10^{-2}	GL_{35}	5.465×10^{-2}
GL_{16}	5.465×10^{-2}	GL_{45}	5.924×10^{-2}
GL_{23}	5.465×10^{-2}	GL_{46}	8.988×10^{-2}
GL_{24}	6.519×10^{-2}	GL_{56}	5.465×10^{-2}

Table 4.2 – *Equivalent conductance between aluminum frame faces*

are fixed on the lateral frame with screws : one for each face, except for face 4 fixed with 3 screws because of the ports. The two assumptions tends to balance each other since that neglecting contact overestimate the conductance while neglecting panels conduction contribution underestimate the total conductance. These phenomena will be studied and taken into account in a more detailed model : the low level model.

The frame is made of 5052 aluminum alloy while 7075 aluminum alloy was used for aluminum panels. Properties of these alloys are given in the table 4.3 and comes from the CES EduPack software.

Alloy	ρ [kg/m^3]	c [J/kg.K]	k [W/m.K]
5052	2672 - 2698	963 - 1002	140 - 152
7075	2770 - 2830	913 - 979	131 - 137

Table 4.3 – *aluminum alloys properties*

Using these properties, the nodal capacitances of the faces are computed by adding the capacitances of the frame face and associated panel.

Node	C [J/K]
301	46.5
302	46.5
303	58.9
304	48.1
305	46.5
306	63.9

Table 4.4 – *Nodal capacitances*

4.3.2 The solar cells

Electrical power management

As the SwissCube, a dissipation circuit has been designed by P. Ledent and P. Thirion in order to deal with the extra power produced by solar cells when the batteries are charged and the required power is lower than collected one. The only way of dissipation in space is heat. As the CubeSat's attitude is passively controlled, no face is pointing to deep space and the use of a radiator to ensure heat rejection is not to be foreseen. In a first design, the extra power is thus dissipated through electrical resistances on the EPS PCB.

The energy collected by the cells is not directly available in ESARAD but can be easily obtained from the power balance of a solar cell (figure 4.8).

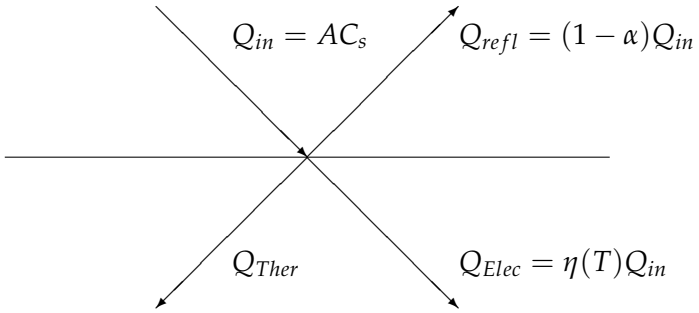

Figure 4.8 – *Solar cell power balance*

Q_{in} is the incident power, equal to the projected area A multiplied by the solar constant C_s and η is the solar cell efficiency. The efficiency available in the data sheets is indeed the AM0 efficiency, meaning that it refers to the incident power and not the absorbed one. The equilibrium gives:

$$Q_{in} = (1-\alpha)Q_{in} + Q_{Ther} + Q_{Elec}$$

Therefore, the heat generated by the cells is given by:

$$Q_{Ther} = (\alpha - \eta(T))Q_{in}$$

But ESARAD gives us the absorbed power : $Q_{ESARAD} = \alpha Q_{in}$ and here is the electrical collected power Q_{Elec} expressed in function of Q_{ESARAD} :

$$Q_{Elec} = -\eta(T)Q_{in} = -\frac{\eta(T)}{\alpha}Q_{ESARAD}$$

In ESATAN, this power is subtracted at the cells and reinjected, partially or not, inside the CubeSat, where dissipation occurs.

Solar cells model

Solar cells have a dedicated node with its own capacitance and its link with the corresponding face. The layout of the solar cell integration made by EADS Astrium is the following one : aluminum panels have been covered with 50 microns (2mil) thick Kapton® foil for insulation reason. The laydown adhesive is RTV S 691 (silicone adhesive) for the Kapton® foil and for the solar cells and is 80 microns thick. From this layout, the equivalent thermal resistance between the cell and the face becomes :

$$\frac{1}{GL_{cell,face}} = R_{cell,face} = \frac{1}{A_{cell}}\left(\frac{t_{cell}}{k_{cell}} + \frac{t_{adhesive}}{k_{adhesive}} + \frac{t_{Kapton}}{k_{Kapton}} + \frac{t_{adhesive}}{k_{adhesive}} + \frac{t_{aluminum}}{k_{aluminum}}\right)$$

Kapton® and RTV S 691 properties are given in the table 4.5

	k [W/m.K]
Kapton®	0.12
RTV S 691	0.39

Table 4.5 – *Thermal conductivity of Kapton™ [14] and RTV S691 adhesive [18]*

The cells are 150 microns thick [7], have a thermal conductivity of more or less 100 [W/mK] [59], a specific heat of about 700 [J/KgK] [59] and weights 86 $[\mathrm{mg/cm^2}]$[7].

4.3.3 The PCBs stack

As explained previously, each PCB is modelled with only one node, representing the mean temperature of the PCB and this model will not be able to reveal local hot spots inside the PCBs. The heat capacity of the PCBs is evaluate by multiplying their mass (about 70g, including PCB and connector) with a equivalent specific heat. The equivalent specific heat is determined with the help of the online calculator developed by Frigus Primore [46].

Inter PCBs links

Concerning the conductive links between the PCBs, there are two main heat flow paths : through the spacers and through the connector. According to the PC/104 specification [41], the connector is made up of 104 phosphor bronze pins and only pins contributes to the link since connector's housing height is such as there is no contact with the above PCB.

Conduction through the M3 endless screws is neglected seeing the clearance with the PCB holes and spacers. The spacers are made of 6061-T6 aluminum and the contact between spacers and PCBs is considered to be perfect. A spacer is a small hollow aluminum cylinder with diameters of 3.3mm (interior) and 4.5mm (exterior). Thermal conductivities of phosphor bronze and 6061-T6 aluminum are given in table 4.6 :

	k [W/m.K]	reference
Phosphor bronze	75	ECSS Q-70-71A[18]
6061-T6 aluminum	152 - 169	CES EduPack

Table 4.6 – *PCBs links materials thermal conductivities*

The ratio between the link through spacers and the link through connector is:

$$\frac{4\ S_{spacers} k_{spacers}}{104\ A_{1pins} k_{pins}} = \frac{4 \times 7.35\ 10^{-6} \times 160.5}{104 \times 0.508\ 10^{-6} \times 75} = 1.2$$

This means that conduction through the spacers is as well important as conduction through the connectors.

PCBs stack links with the structure

The PCBs stack has 8 contact point with the external structure : four at the top with the COM PCB and 4 at the bottom with OBC PCB. The top links are ensured bu the "*midplane standoffs*" as presented on the exploded view in chapter 2. Two midplanes ensure the fixation with the face 5 and two with face 2. The conductive link through is not easy to evaluate and, as for the aluminum frame links, a finite element model has been created within SamcefField. Again, perfect contact is assumed between the PBC and the frame.

Figure 4.9 illustrates the temperature distribution inside a midplane standoff when a gradient of 10°C is imposed between the two perpendicular faces involved. The equivalent thermal conductance is obtained by dividing the resulting flux by the difference of temperatures.

Concerning the bottom link of the PCBs stack, OBC PCB is supported by four stainless steel threaded loose fasteners (in which the endless screws are screwed) inserted in the bottom frame face. Once again, perfect contact is assumed.

4.3.4 The batteries

The two LiPo batteries are located on a secondary smaller PCB itself fixed on the EPS PCB as shown by the exploded view (figure 1.11). The

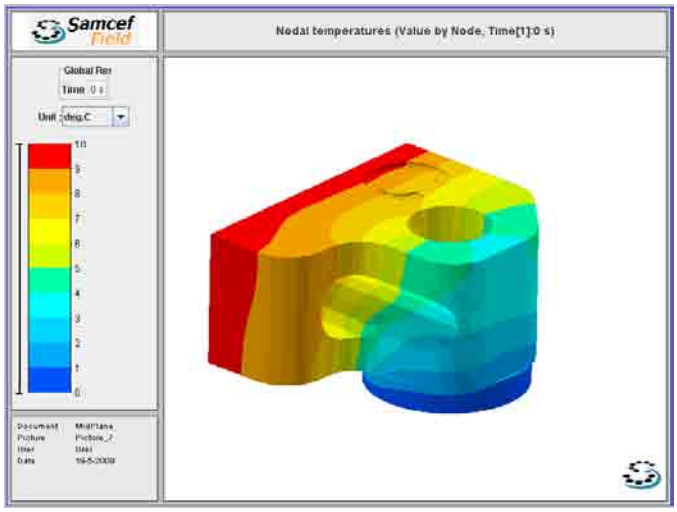

Figure 4.9 – *Conductive link computation through a finite element analysis within SamcefField of a midplane standoff*

	GL [W/K]
Structure - OBC	0.12
OBC - OBC2	0.58
OBC2 - EPS	0.58
EPS - BAT PCB	0.35
EPS - EPS2	0.35
EPS2 - COM	0.58
COM - face 2	1.42
COM - face 5	1.42

Table 4.7 – *PCBs links*

conductive link between the batteries' PCB and the EPS PCB is also ensured by four spacers. The material of these spacers is not yet defined and is kept as parameter. aluminum conductivity will be assumed as initial value.

Concerning the specific heat of the batteries, we used the one of Varta PoLiFlex® available in the SwissCube Phase C technical report [35], keeping in mind that the model used is not yet defined.

4.4 Worst cases definition

As introduced in the previous chapter, thermal analysis is subjected to a worst cases approach.

The assumptions about cold and hot cases are the same as the one described in the preliminary analysis :

- Hot case : maximum environmental fluxes, orbit permanently illuminated, electrical collected power entirely dissipated into heat. Now that PCB are modelled, the internal power is distributed between the two PCBs containing the most dissipative components : COM (amplifier) and EPS (dissipation circuit, voltage converter). Without

accurate information about these components, an equal distribution between COM and EPS has been assumed.

- Cold case : minimum environmental fluxes, maximum eclipse time (apogee in eclipse involving more than 35 min in eclipse for a period of 104 min), no internal dissipation.

The effect of thermo-optical properties degradation is only taken into account for the Kapton® used on the panels, its absorptivity increasing over time, and the solar cells efficiency, decreasing over time, since aluminum surface treatments are relatively stable over a lifetime such as the one expected for OUFTI-1 (about one year). As the absorptivity of Kapton®, measured by EADS Astrium, is already high (0.87) the End-Of-Life value is set to 0.9. Concerning the solar cells efficiency, a diminution of 10% is considered : 30% BOL and 27% EOL.

4.5 Results

4.5.1 Hot case

Figure 4.10 shows the different contributions to the total absorbed power during one orbit. The total power is represented by the black dotted line and the effective thermal power, obtained by subtracting the electrical power collected by the cells from the total power, is the continuous black line. As explained above, all the electrical power is redistributed inside the CubeSat as internal heat loads so that the total power (dotted line) finally contributes to the heating of the CubeSat. The rapid variations are the consequence of rotation of the CubeSat around its axis aligned on Earth's magnetic field, here set at one degree per second.

Figure 4.11 shows associated ESATAN results. It is obvious that they are quite different from those exposed in the preliminary analysis. The bar plot on the right shows the maximal temperature reached at the main nodes during the orbit. They are all comprise between 30 and 35°C. But, considering the maximal allowable temperature of the batteries (45 °C), this simulation confirms the result obtained in the preliminary analysis : the safety margin is narrow and other solutions may be foreseen. A possible solution could be imagined by analyzing the graph in the bottom left corner. It shows that the EPS2 PCB is quite cooler than the EPS PCB since no power is dissipated on EPS2. Actually, according to [33] and [55], the dissipated energy on EPS2 will be smaller in any case. A possibility could then to attach the batteries' PCB to EPS2 PCB instead of EPS PCB. This solution will be studied in details in the low level model.

The other reasons for which EPS2 is cooler is deduced from the same graph. It shows that even if half of the collected power is dissipated on the COM PCB, it remains cooler than the others mainly because it is linked with two opposite faces (2 and 5) and when the first one is in sunlight, the other is consequently turned to deep space. The other fact involving cooler temperatures of COM and EPS2 PCBs is that the conductive links with the structure is greater than the one linking the OBC to the structure (the midplane standoff are made of aluminum, nearly ten times more con-

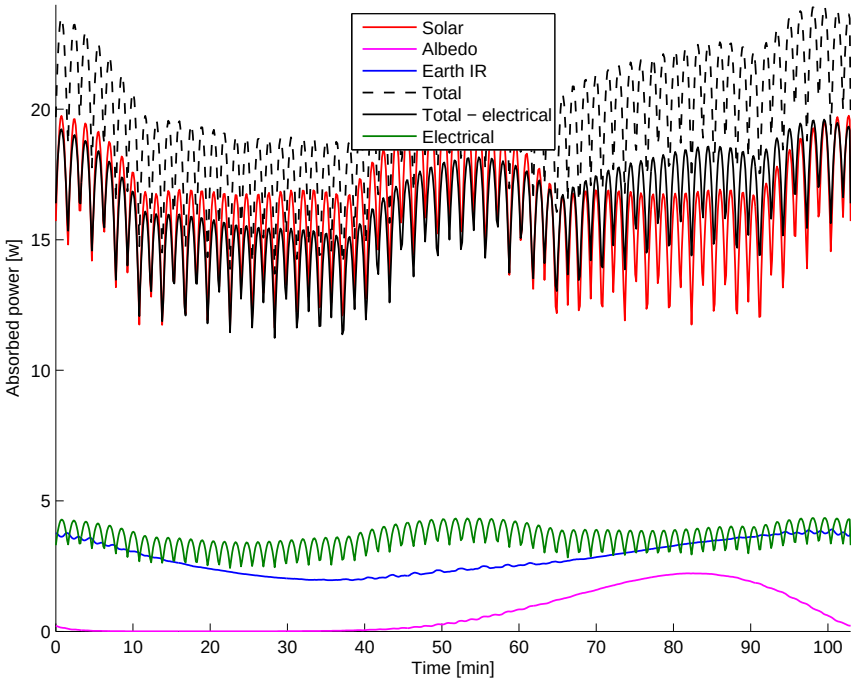

Figure 4.10 – *Hot case absorbed power*

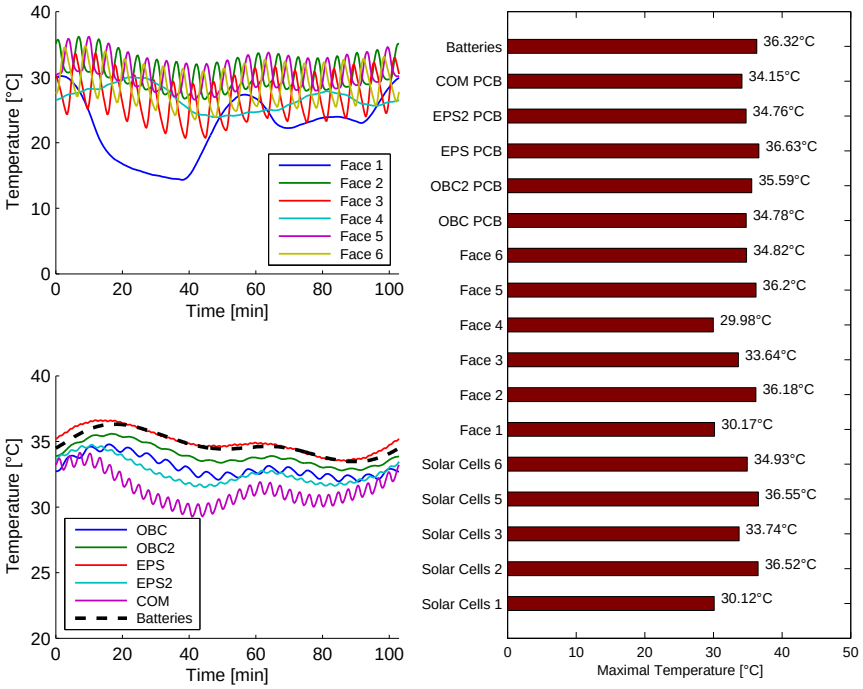

Figure 4.11 – *Hot case temperatures*

ductive that stainless steel used for bottom spacers, as it was indicated in the table 4.7).

Another intuitive consequence of the PCB configuration is that central PCBs (EPS, EPS2) are less sensitive to external temperature variations than OBC and COM PCB. This is intuitive since central PCBs are more insulated from the external structure.

One must keep in mind that those temperatures are averaged temperatures which are then not able to represent of local hot spot that may occur, especially on the PCBs.

The graph in the top right corner illustrates the temperature evolution of the faces. Face 1 and 4 have a different comportment than the others : this is a consequence of the passive alignment of one axis of the CubeSat on Earth's magnetic field. The rotation about this axis is clearly visible through the fast variations of faces 2,3,5 and 6 while faces 1 and 4 spends more time in sunlight or shadow.

Globally, one can see that internal components undergo relatively lower temperature variations than the external structure. Moreover, the rotation rate considered here is 1 deg/s. ADCS simulations [25] shows that the CubeSat will certainly undergo higher rotation rates, depending on the initial condition after being released from the P-POD and on the moment generated by the deployment of the antennas. Figure 4.12 illustrates the consequence of a rotation rate of 5 deg/s. The variations are then too fast compared to the thermal inertia of the faces and PCBs. These ones do not undergo anymore fast variations and are almost constant. A steady state analysis considering the mean incident fluxes would then be suitable and more computation-time effective, especially for the next model, much more complex.

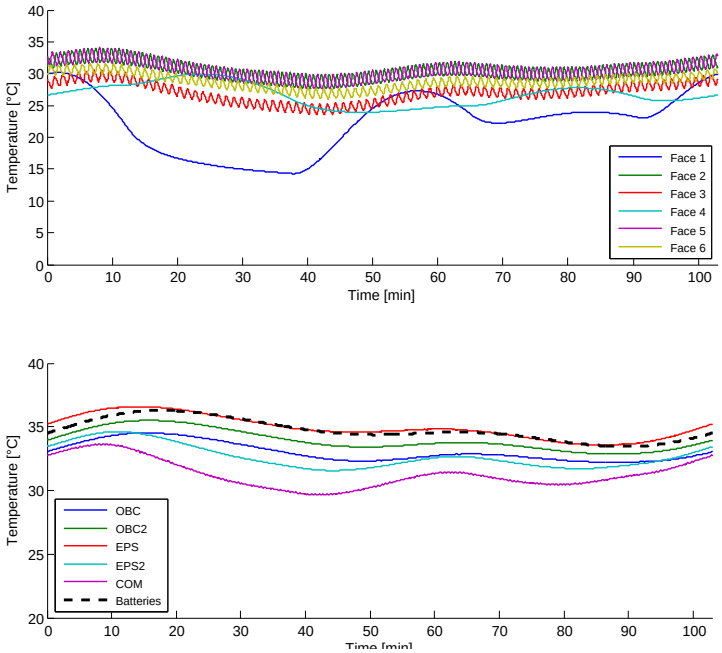

Figure 4.12 – *Evolution of the temperatures during one orbit for a rotation rate of 5 deg/s*

4.5.2 Cold case

Now that the hot case has been analyzed, it is time to examine the cold one. Once again, the evolution of absorbed powers along the orbit is represented at figure 4.13. A first difference with the hot case, excluding the evident eclipse time, is a higher albedo since the CubeSat get over the subsolar point[1]. The second feature visible is the presence of two off-peaks around 10 and 90 minutes. These off-peaks occurs when the face 1 (first one) or 4 (second one) is perpendicular to sun rays, the projected area being much lower. The second off-peak is lower than the first one because of the lower absorptivity of face 4, not covered with solar cells.

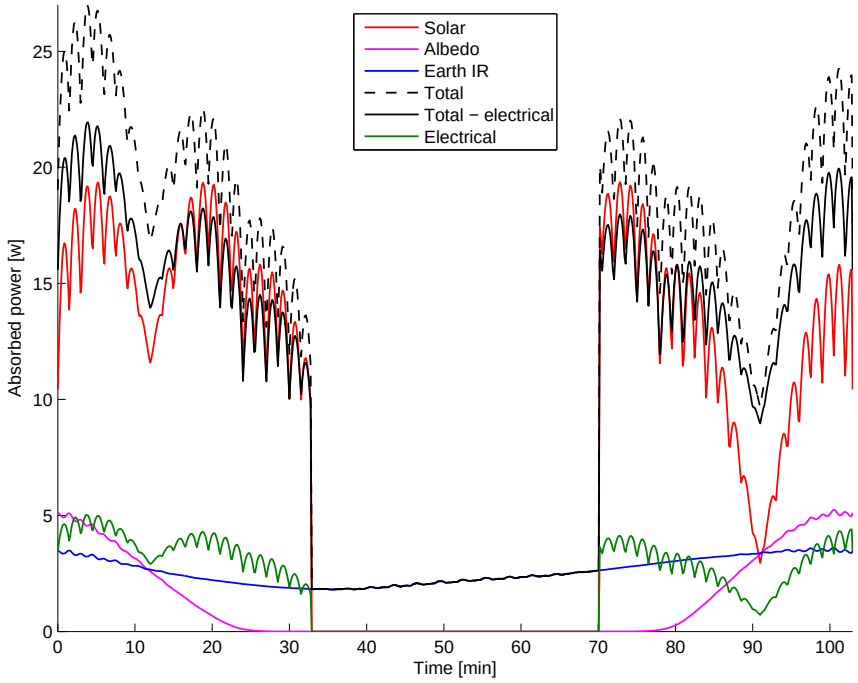

Figure 4.13 – *Cold case absorbed power*

Concerning the temperatures, results are illustrated by the figure 4.14. The off-peaks visible in the absorbed power are turned here into peaks: shortly after 10 minutes, the upper left graph shows that face 1 undergoes a rise of its temperature.

But the important fact is not there: the temperature of the batteries drops below -20°C while its allowable minimal temperature in charge is 0°C! Obviously, a heater will be needed to raise the temperature of the batteries. But one must pay attention to the limits of the model : as each PCB is modelled with one node, no transverse conduction is taken into account in the link between the EPS PCB and the PCB sustaining the batteries. Furthermore, the assumed material of the spacers between the EPS and

[1] As it has been studied in the preliminary analysis, the higher albedo present in the cold case and not in the hot case does not affect significantly our worst case definition

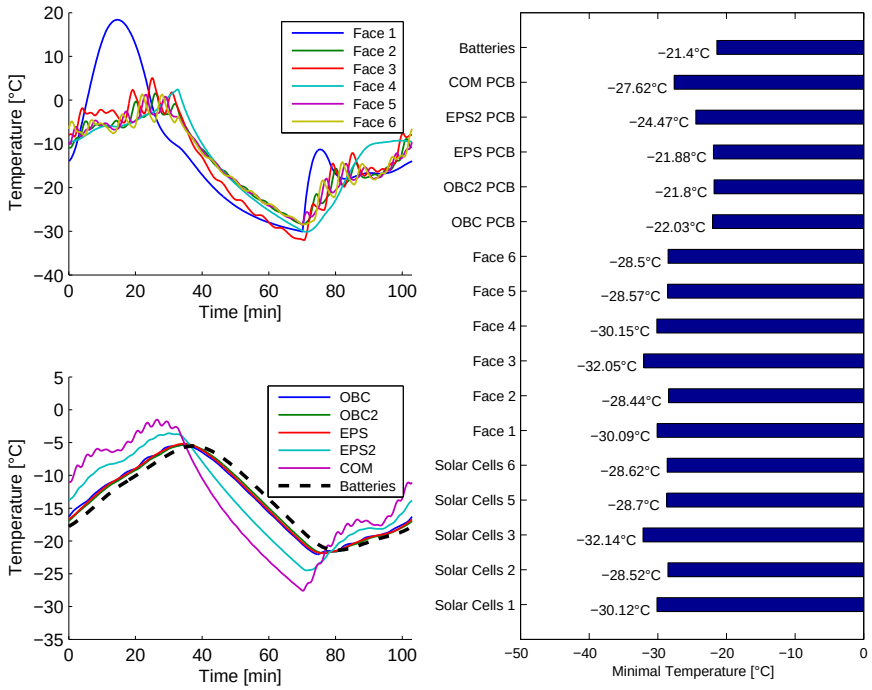

Figure 4.14 – *Cold case temperatures*

BAT PCB is aluminum which is a good conductor. These two assumptions are not favorable to the batteries. The influence of the EPS-BAT spacers conductivity

Again, the COM PCB is cooler than the others for the same reasons that those previously presented.

4.5.3 Sensitivity analysis

Cold case has shown that the batteries had approximatively the same temperature as the EPS PCB one. But this was for EPS-BAT spacers in aluminum. The scope of this sensitivity analysis is then to evaluate the effect of reducing the thermal conductivity of these spacers.

Figure 4.15 shows that insulating the batteries has a positive effect: reducing the conductivity from 150 to 5 W/mK increase the minimal temperature reached by the batteries from -21 to -17°C. The graphic on the right shows that the efficiency of this effect is maximum between 1 and 100 W/mK. Considering the definition of a conductive link $GL = \frac{kS}{L}$, increasing the length or reducing the area would have the same effect but structural constraints must be taken into account (resistance, rigidity, density,...). Again, materials having very low thermal conductivity are thermoplastics or thermosets but not compatible with structural aspects. Using CES EduPack, titanium and titanium alloys appeared to be a good choice and having a thermal conductivity about 10 W/mK with a high Young's modulus and high tensile strength.

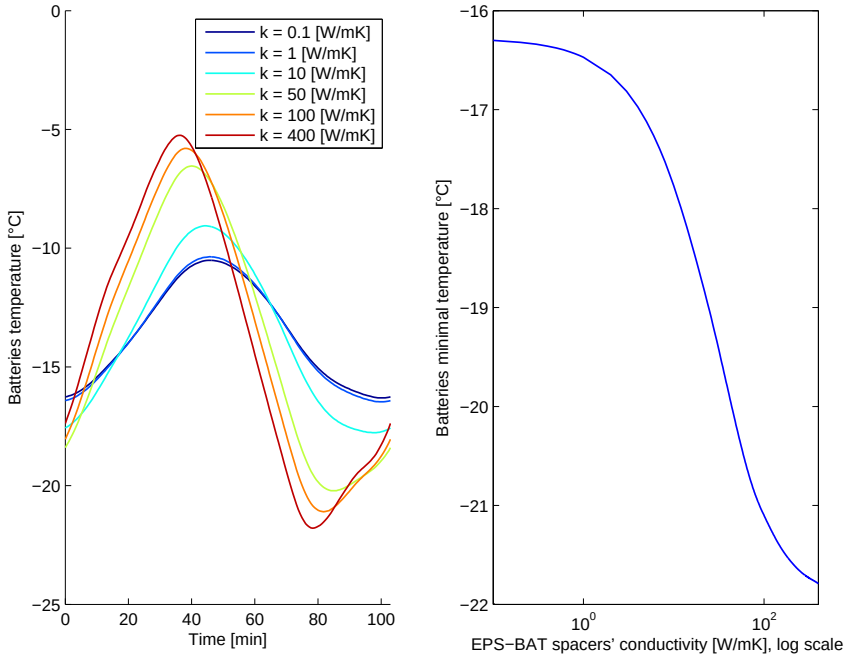

Figure 4.15 – *In uence of the EPS-BAT spacers conductivity on batteries' temperature*

Once again, further analysis will be developed with the low level model because some important effects neglected here such as transverse conduction through PCBs will be taken into account.

Nevertheless, a combined solution, both passive, through batteries insulation, and active with small heaters, will certainly be required to maintain the batteries in their safe range of temperatures.

Summary

This Simplified Thermal Model has allowed to evaluate the average temperatures of each PCB and confirmed the potential problems considering the batteries for both hot and cold cases. However, even if it allowed to foresee some possible solutions to these problems, several assumptions has to be removed in order to properly design suitable solutions. This is the aim of the Detailed Thermal Model. However, before presenting the Detailed Thermal Model, some measurements are required and discussed in the next chapter.

Measurements 5

This chapter describes several measurements performed at the Centre Spatial de Liège, notably about the batteries. The thermal design of a satellite involves a good knowledge of thermo-optical and materials properties, as it has been shown previously. But in a student project, only few measurements can be performed. In this chapter, several experiments will be done to determine different properties of the aluminum frame and the batteries.

5.1 Why and which measurements ?

Li-Po batteries thermal properties are not well known and difficult to find. Yet, as already spotted, they are the more critical unit seeing their narrow range of temperatures and measurements seemed necessary. Moreover, the data used in the previous models were based on SwissCube model but their batteries are packed in small aluminum boxes. That is the reason why the first experiment concerns the determination of the thermal properties (conductivity and the specific heat) of a typical LiPo battery such as the one probably used in our CubeSat.

The second measurement focuses on the thermal emissivity of the aluminum frame's two coatings : alodine and hard anodizing. This test is based on a thermographic measurement. This is also the case for the third one about the thermal contact between the top and bottom faces with the lateral frame, around the screws.

5.2 The Battery

The goal of this test is thus to evaluate the thermal capacitance and transverse conductivity. These two properties are crucial when designing heaters : how much power will be required to maintain the two batteries above a given threshold and where to put the control sensor. Indeed, the combination of thermal capacitance and conductivity gives us a delay between the time the heater is turned on and the sensor response. It acts like an hysteresis and prevent the heaters from too fast pulsing.

5.2.1 Experimental setup

This test will be performed on a battery Kokam SLPB-554374-H which is representative since the foreseen models (Varta, Kokam, Panasonic) are all of approximately the same size and made upon the same technology.

The principle of the test is to heat one side of the battery while imposing the temperature of the opposite side. By this way, the temperature of the heated side will rise up to its constant steady state value. To impose the temperature of the "*rear side*", the battery is fixed on an interface plate which is itself strongly fixed with bolts on a massive steel bench. Seeing its large capacitance, the temperature of the bench is assumed to remain constant and equal to the ambient temperature. Thermal compound[1] is used between the interface plate and the battery to ensure a good contact. As shown on the figure 5.1, the battery is then strongly pressed on the interface plate with two pieces of CFRP. CFRP has been chosen for its high rigidity to thermal conductivity ratio. As all the test is performed under ambient conditions, heaters are covered with aluminum tape to prevent heat flux from escaping radiatively and all the setup is covered with MLI[2] again to diminish radiative losses and reduced convective exchanges.

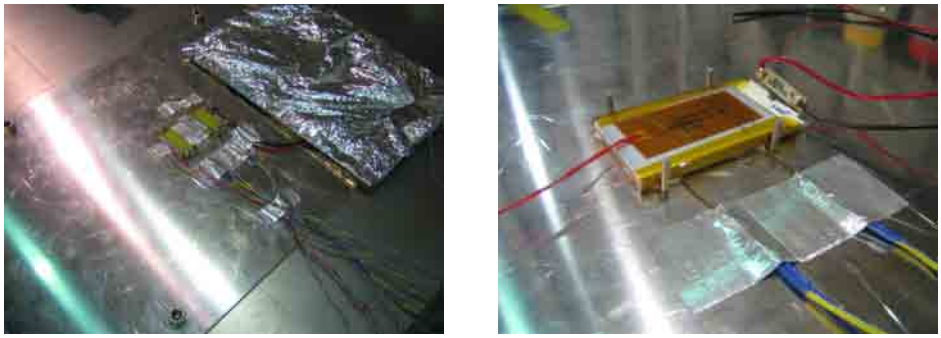

Figure 5.1 – *Battery test setup*

Concerning the heater used is a Minco HK5164R39.2. Unfortunately, the heater does not cover the entire area of the battery as shown on the right picture of the figure 5.1 but this will be taken into account in the model. To reduce errors, multiple consecutive heating cycles are performed and the model will be adjusted for all the cycles. Acquisition is made through thermocouples and PT100 sensors linked to a PC equipped with a Keithley 2700 datalogger.

5.2.2 The model

In order to determine the two desired properties, a Simulink™ model fitting at best the setup has been created. Simscape™ toolbox available in Matlab™ Simulink™ R2008 is used, allowing to create transient thermal model with simple constitutive elements: thermal masses, conductive/radiative/convective links, heat and temperature sources and sensors etc... Our model is shown on the figure 5.2. It contains four thermal masses : two for the top and bottom side of the battery, one for the interface plate and one for the bench. Indeed, seeing the results, the temperature of the battery bottom side is no more imposed to model the observed local heating of the interface plate and bench. This model takes also into

[1] Wakefield Engineering Thermal Compound n°126-4

[2] Multi Layer Insulation with Dacron netting or "bridal veil" between the layers to reduce contact

account the conduction through the thermal compound between the bottom side and the interface plate.

The same consecutive powers really injected in the heater is set as input and the three measured temperatures are set in output: battery both sides and the interface plate.

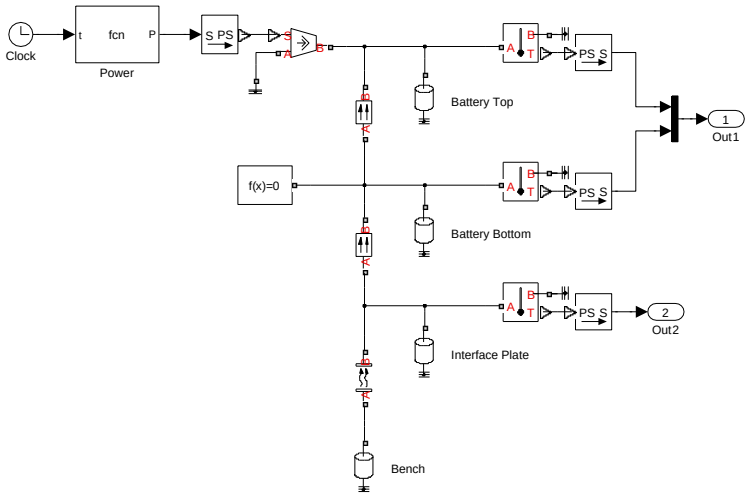

Figure 5.2 – *Battery test Simscape™ model*

5.2.3 Model adjustment & results

The SLPB-554374 real dimensions differed somehow from the one mentioned in the datasheet : the real ones were $65 \times 40 \times 5$ [mm] (instead of $70 \times 42.5 \times 5.6$ [mm]) which leads to a volume of 13000 [mm^3] for a weight of 34g.

As the heater does not covered all the area and thanks to the different sensors[1] used, it has been observed that the temperature of the top side was of course not uniform. Intuitively, one decided to consider that the heat flux propagates through a reduced area equal to mean area between the heater and the bottom side ($\frac{65+50}{2} \times \frac{40+25}{2}$ [mm]). It is such as the heat flux propagates according to a truncated pyramid shape whose bottom face would be the bottom side and top face the heater.

The measured temperatures presented at the figure 5.3 results from an averaging between the temperatures measured by the different sensors. The thermal inertia of the interface plate has its importance: it acquires and releases energy and contributes to the damping of the system. At the same time, if the bench had not been modelled and replaced by a fixed temperature, the global heating of the system could not have been represented (the temperature ad the end of the test is greater than the initial one because the bench absorbed some energy and did not have the time to release it seeing its large thermal inertia). By adjusting the different parameters of the model, the measured temperatures are finally

[1] We had 4 sensors on the top side, 2 on the bottom side and 2 on the interface and bench

fitted and the desired properties are determined: the specific heat is about 1350 [J/kgK] and the conductivity 1.55 [W/mK] (through the reduced area which is equivalent to 1.11 [W/mK] through the entire area).

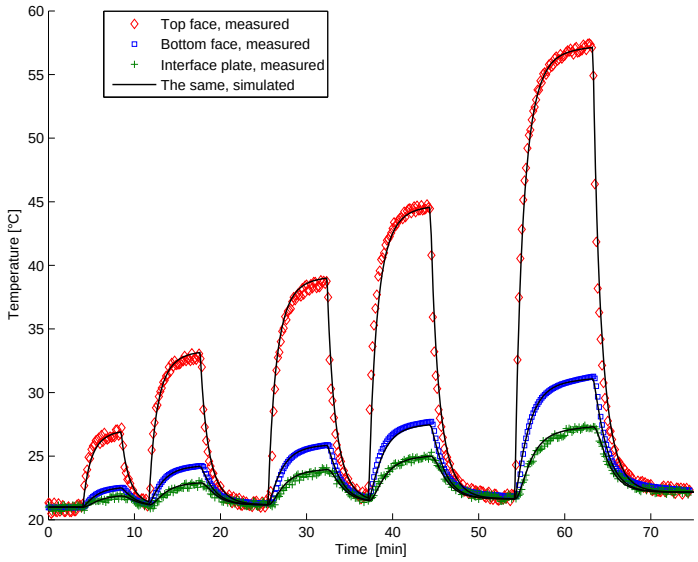

Figure 5.3 – *Battery test comparison between measurements and adjusted model*

This involves a heat capacity of 45.9 [J/K]. Although the internal composition of the battery is difficult to known, it appears that the electrolyte of Li-Po batteries is held in polymer composites such as polyethyleneoxide (PEO) or polyacrylonitrile. Such materials have high specific heat about 1800 [J/kgK]. On the other hand, the cathode, anode and packaging shell have lower specific heat. This leads us to believe that the determined value is not too far from reality. The results were also compared with data from specific measurements on other Li-Po batteries [60].

One must keep in mind that the employed method relies on some assumptions : radiation and convection losses were neglected even though limiting their effects. The representativeness of the test compared with the real configuration is also limited since larger heaters will probably be used to cover all the available area and batteries will not be fixed on aluminum plate but on CFRP (PCB).

5.3 ALUMINUM FRAME EMISSIVITY

5.3.1 Anodizing vs Alodine

The second test mentioned concerned the measurement of the emissivity of the Pumpkin structure. The frame has two different surface treatments: the rail are hard anodized and the remaining surface is alodyned and here are a few words about these two processes. The purpose of both coatings is to improve corrosion resistance but while Alodine maintain electrical conductivity, anodized surfaces have a enhanced protective ox-

ide layer which is also a poor electrical conductor. Anodizing is an electrolytic passivation process increasing the oxide layer thickness. Alodine is a chemical conversion coating (also known as Iridite or Chromate Conversion). Both treatments improve adhesion for paint primers and glues. In our case, the rail were anodized to prevent galling (as a reminder, the rails are the only part of the CubeSat in contact with he P-POD). According to Adam Reif from Pumpkin, here are the military specifications (MIL-spec) reference of these two processes: MIL-A-8625F, TYPE III, CLASS 1 [38] for the anodized process and MIL-DTL-5541F Type II, CLASS 1A for Alodine [39]. Type III CLASS 1 means non-dyed hard anodizing and Type II, CLASS 1A for alodine means that no hexavalent chromium (environment friendly) is used in the process (Type II) and that maximum protection against corrosion is provided (class 1A).

Nevertheless, precise data about alodine and hard anodized emissivity were quite difficult to find and optical properties are highly surface treatment dependent. For example, figure 5.4 excerpt from a NASA report about thermal control coatings, shows how the chemical reaction time of a chemical conversion coating on aluminum affects its optical properties.

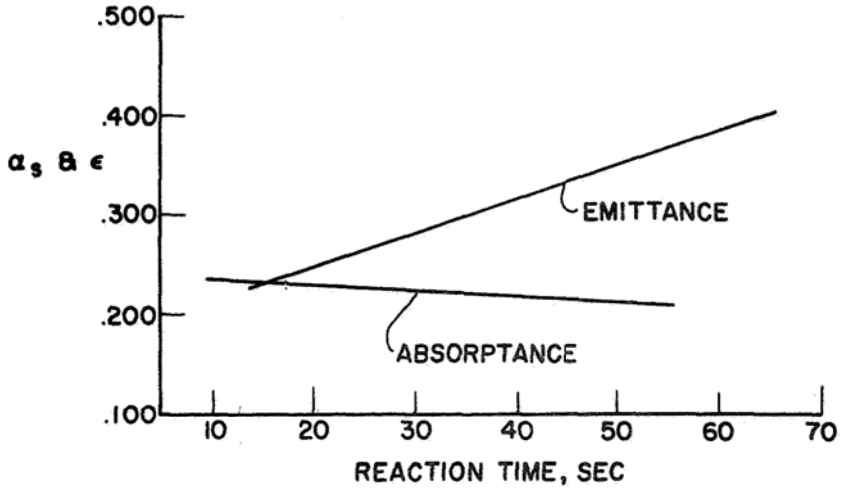

Figure 5.4 – *Evolution of the emissivity and absorptivity of aluminum sample subjected to a conversion coating surface treatment in function of the reaction time [61]*

So, emissivity measurements were planned. Many thermal emissivity measurements method already exist but they often required specific setups and expensive apparatus. A simple and relatively convenient way of doing this is to use a thermographic camera.

5.3.2 Measuring emissivity with a thermographic camera

Here is a brief theoretical recall about thermographic measurements. As depicted in Figure 5.5, one must be very cautious on how to interpret the measured data. Indeed, the total input power collected by the camera, W_{tot}, has different contributions:

1. emission from the object we are looking at;

2. reflected emission from ambient sources;
3. atmosphere emission.

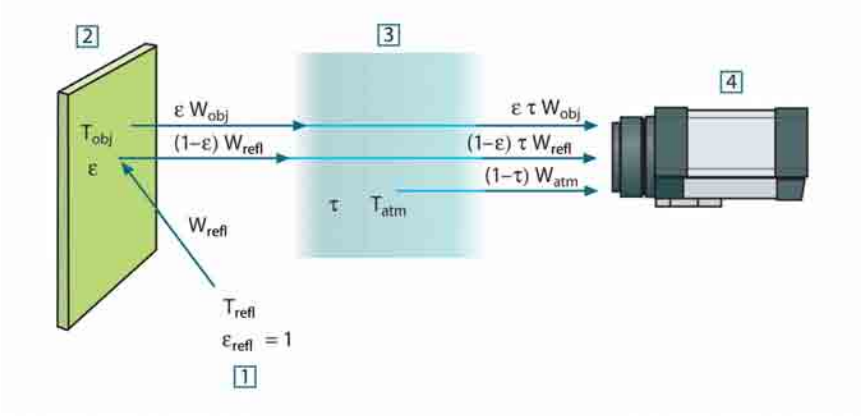

Figure 5.5 – *A schematic representation of the general thermographic measurement situation from the ThermaCAM User Manual [21]. 1: Surroundings; 2: Object; 3: Atmosphere; 4: Camera*

These contributions involve four main parameters the user has to supply:

- the object emissivity ϵ
- the atmosphere transmittance τ depending on the distance between the object and the camera, the atmosphere relative humidity and its temperature
- surroundings average reflected temperature
- surroundings effective emissivity

Concerning, the surrounding effective emissivity, all radiation emitted from the object is assumed to never come back so that the environment can be considered as a blackbody and its effective emissivity is one.

The total collected radiation power seen by the camera is then :

$$W_{tot} = \epsilon\tau W_{obj} + (1-\epsilon)\tau W_{refl} + (1-\tau)W_{atm}$$

and the radiation power effectively emitted by the object is given by:

$$W_{obj} = \frac{1}{\epsilon\tau}W_{tot} - \frac{1-\epsilon}{\epsilon}W_{refl} - \frac{1-\tau}{\epsilon\tau}W_{atm}$$

These equations show that to determine the effective object emitted power, the camera has to subtract the two unwanted contributions. But as the emissivity decrease, the contribution coming from the reflected temperature of the surroundings increases according to $\frac{1-\epsilon}{\epsilon}$ and so does the sensitivity to reflected environment parameters. A way to reduce this sensitivity is to increase the ratio between object and surroundings emitted radiation. The emitted radiation is proportional to the temperature at the fourth power and the ratio is thus equal to $\frac{1-\epsilon}{\epsilon}\frac{T_{refl}^4}{T_{obj}^4}$. The influence of these

two parameters are represented in Figure 5.6. The lower the emissivity, the more important is the influence of temperature. For example, with an emissivity of 0.1, heating the object up to 80°C reduces the ratio from 9 to 4.

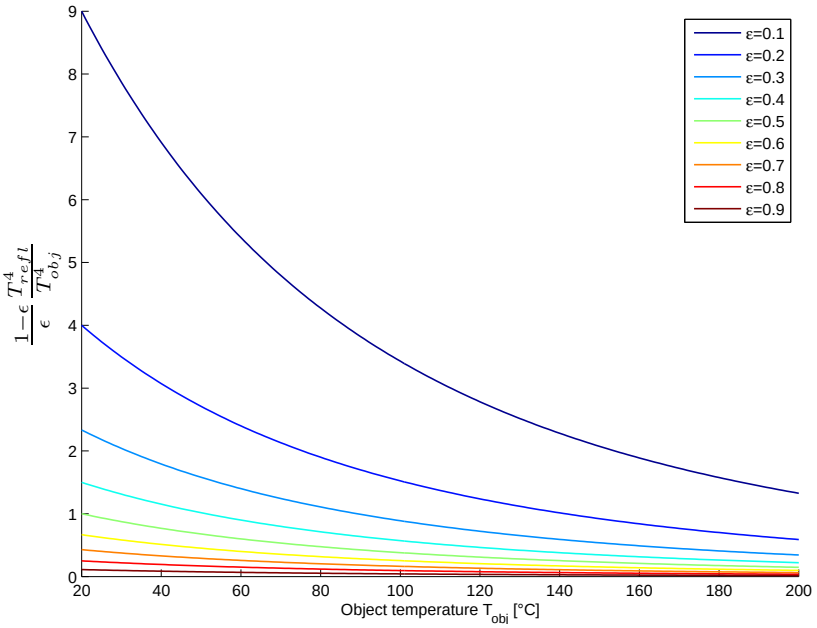

Figure 5.6 – *In uence of the object temperature and emissivity for a thermographic measurement*

For this reason, several measurements shall be performed at different temperatures. In practice, for each temperature, the object emissivity parameter in the software shall be varied, noticing the resulting temperature given. If the temperature calculated by the software is equal to the one measured by the sensor then the corresponding emissivity must be close to the real one.

5.3.3 Experimental setup

The camera used was a ThermaCAM® S40 from FLIR Systems equipped with a 320 × 240 microbolometer array.

In order to have a uniform surrounding environment, we enclose the structure with a high emissivity box of known temperature. We placed the camera close to the structure to limit atmosphere effects (Relative humidity was 47% and distance 30cm) and tilted the frame to avoid camera's own emitted radiations reflection like looking in a mirror (figure 5.7, left). The structure was heated through a plate on which we fixed heaters, as shown the the right picture of the figure 5.7.

Figure 5.8 shows the infrared picture of the structure heated up to 90°C. The two considered areas for the emissivity calculation are the one enclosed by green rectangles, close to which sensors are set as shown in figures 5.7 and 5.8.

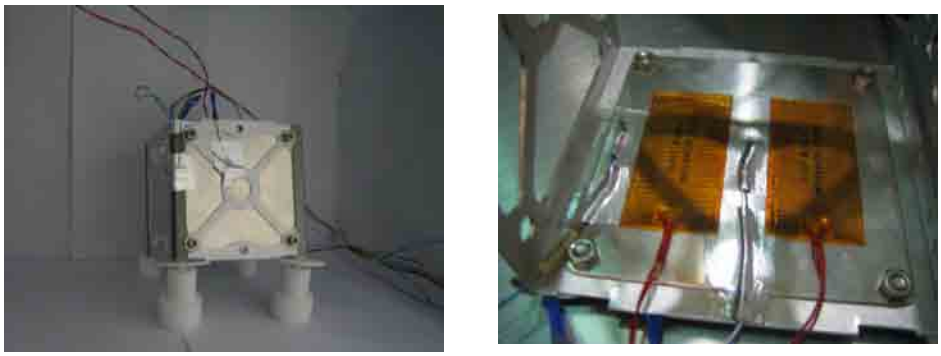

Figure 5.7 – *aluminum frame emissivity test setup*

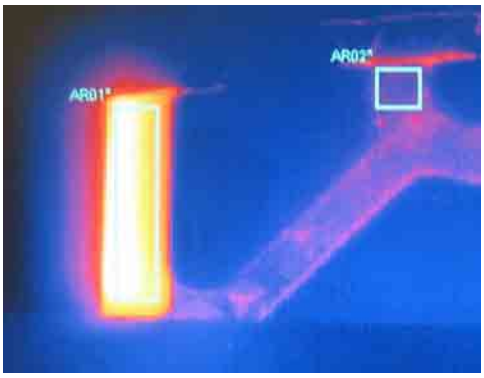

Figure 5.8 – *Infrared capture of the structure heated up to 90°C*

5.3.4 Results

First, the method has been validated by measuring samples whose emissivity were well known : 3 mil kapton foil on aluminum backing ($\epsilon = 0.81$, [52]), common aluminum plate ($\epsilon \cong 0.1$, [21]) and white paper sheet ($\epsilon \cong 0.8$, [21]).

Then, as previously said, measurements were performed at different temperatures and for each of them, the emissivity is varied and a relative error can be deduced between the measured value and the infrared calculated one:

$$\frac{T_{IR} - T_{mes}}{T_{mes}}$$

The evolution of this error in function of the measured temperature and emissivity is represented in Figure 5.9. The left plot represents the hard anodized results while the right plot displays the Alodine ones.

The Alodine curves are more emissivity sensitive and that confirms the theoretical curves of Figure 5.6 showing that when the emissivity was low, two consecutive curves were well spaced. Figure 5.9 also confirm that as the measurement temperature increase, the emissivity leading to a zero error seems well to converge.

Seeing these graphs, we can finally conclude that the emissivity of the Alodine and hard anodized coatings are respectively about 0.14 and 0.69.

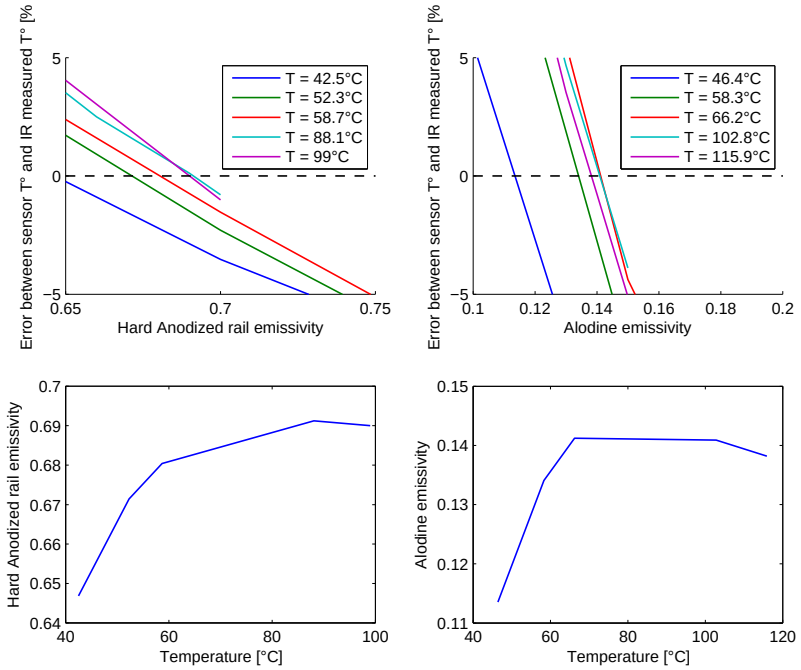

Figure 5.9 – *aluminum frame emissivity test results*

5.4 ALUMINUM FRAME CONTACT RESISTANCE

The third experiment concerns contact between top and bottom face screwed on the lateral frame. The contact phenomenon between frame elements is clearly highlighted in Figure 5.10 which presents some screwed-joints in front of a bright background: only a fraction of the surface area contributes to heat flow path between the faces.

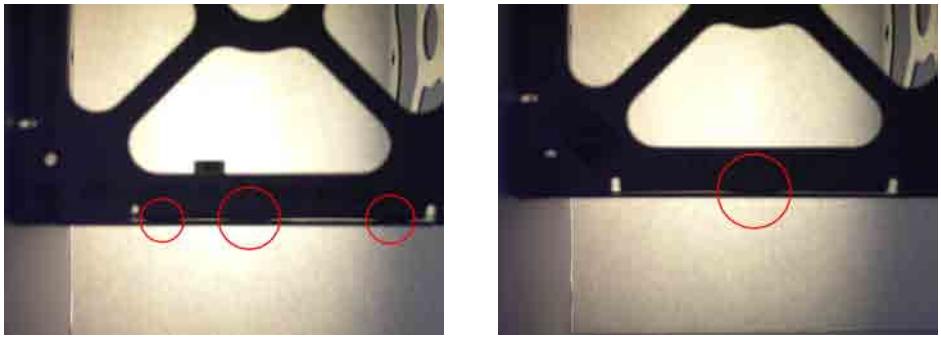

Figure 5.10 – *Aluminum frame contacts in front of bright background. On the left, face 6 and 4, fastened with 3 screws and on the right, face 6 and 1, fastened with one screw*

The experiment is done under ambient conditions so that convective losses are absolutely not negligible and difficult to take into account. Then, the aim of this experiment is not to compute accurate thermal conductances values but rather to evaluate the importance of the phenomenon. For this purpose, infrared imaging is again used.

The method consists in imposing a heat flux between faces 3 and 6 through the contact. To do this, face 6 is heated up while face 3 is strongly fastened to a large bench (high thermal inertia) to prevent its temperature from rising. By this way, all the heat (except convective and radiative losses) must flows through the contact resistance. IR imaging can then show if the contact area is strongly localized or well spread across all the area of the bracket. Figure 5.11 shows the IR pictures of the contact between faces 6 and 1 (left) and between faces 6 and 2(right). The first one confirms that the contact is well localized: the area below the screw is hotter meaning that only this part of the surface contributes to the contact resistance and that constriction phenomenon occurs (shrinkage and concentration of the heat flow lines around the contact area). On the contrary, the right picture is less convincing: heat flows seems to be more distributed on all the surface.

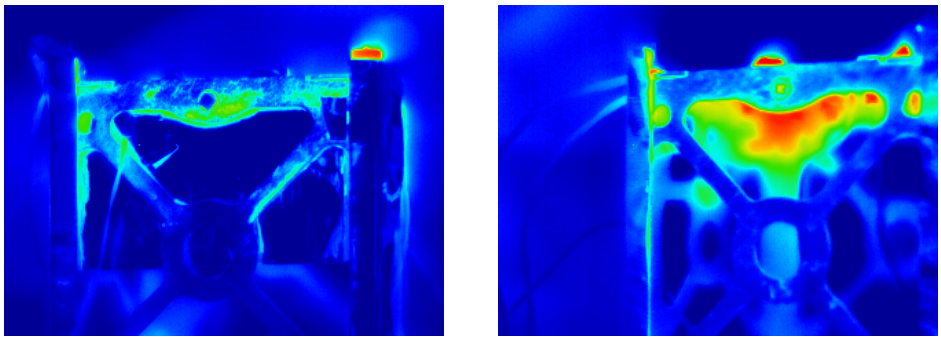

Figure 5.11 – *Infrared images Battery test setup*

In the same way, the other contact areas were also studied leading to the same conclusions: contact is present but difficult to estimate and varies from one screwed-joint to another.

Summary

The preliminary analysis and simplified thermal model showed that thermo-optical properties were important and that the batteries thermal inertia contributes largely to the global thermal of the CubeSat. Measurements allowed us to determine relatively accurate values for the emissivity of the aluminum frame and for the thermal properties of the battery. For instance, the emissivity of the frame rails is in reality lower than the assumed values : 0.7 instead of 0.8 and the heat capacity of the battery is quite greater: 1350 [J/kgK] instead of 960 [J/kgK]. These new values will be used in the newt chapter describing the detailed thermal model of OUFTI-1. Even if the third experiment did not lead to concrete values, it demonstrated the presence of contact phenomenon between the lateral frame and bottom/top faces. This phenomenon will then be taken into account through data found in the literature and finite elements analysis.

Detailed Thermal Model 6

Introduction

Up to this point, two models have been developed. Both revealed the need of an active thermal control to keep the temperature of the batteries above its lower limit. But the Simplified Thermal Model (STM) was too limited to allow a convenient and realistic design of a heater.

As already pointed, the STM was also unable to represent the potential hot spots due to low efficiency electronic components such as the amplifier. Moreover, as the model detail evolves along with the design maturity of the CubeSat, especially electronic circuits, the dissipation system introduced in the previous chapter also evolved. The new design is composed of a dissipation transistor in series with a resistance instead of resistances alone. This means that the heat load will probably be strongly localized.

All these issues suggest to develop a more precise model allowing concrete decisions and solutions. This is the aim of the present chapter presenting the Detailed Thermal Model (DTM). It is divided into four main parts : developing, checking, analyzing and optimizing the model.

6.1 Geometric Mathematical Model

Like the Simplified Thermal model and any other thermal model, the DTM consists of a GMM, used for the computation of the radiative exchange factors and environmental absorbed powers, and a TMM, modelling the conductive network between the nodes, their thermal inertia and dealing with the internal dissipated power distribution.

6.1.1 Nodal breakdown

aluminum Frame

In the Simplified Thermal model, each face of the aluminum frame was considered isothermal. But as represented in Figure 6.1, the midplane standoffs, linking the aluminum frame with the COM PCB, are connected at the top of faces 2 and 5, near the face 3. This was thus not taken into account in the STM. For this reason, each face of the aluminum frame is now into several elements.

Actually, to model at best the point where the midplane standoff is fastened, the face is divided into nine nodes, unequally distributed : the

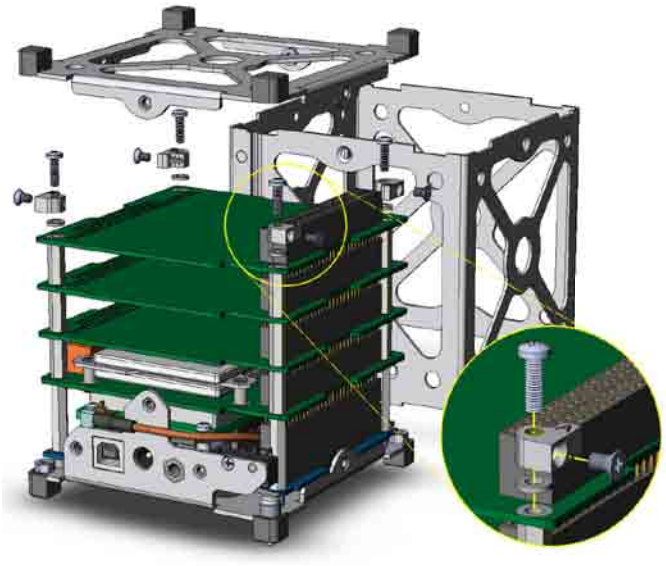

Figure 6.1 – *Midplane standoffs fastening to the aluminum frame*

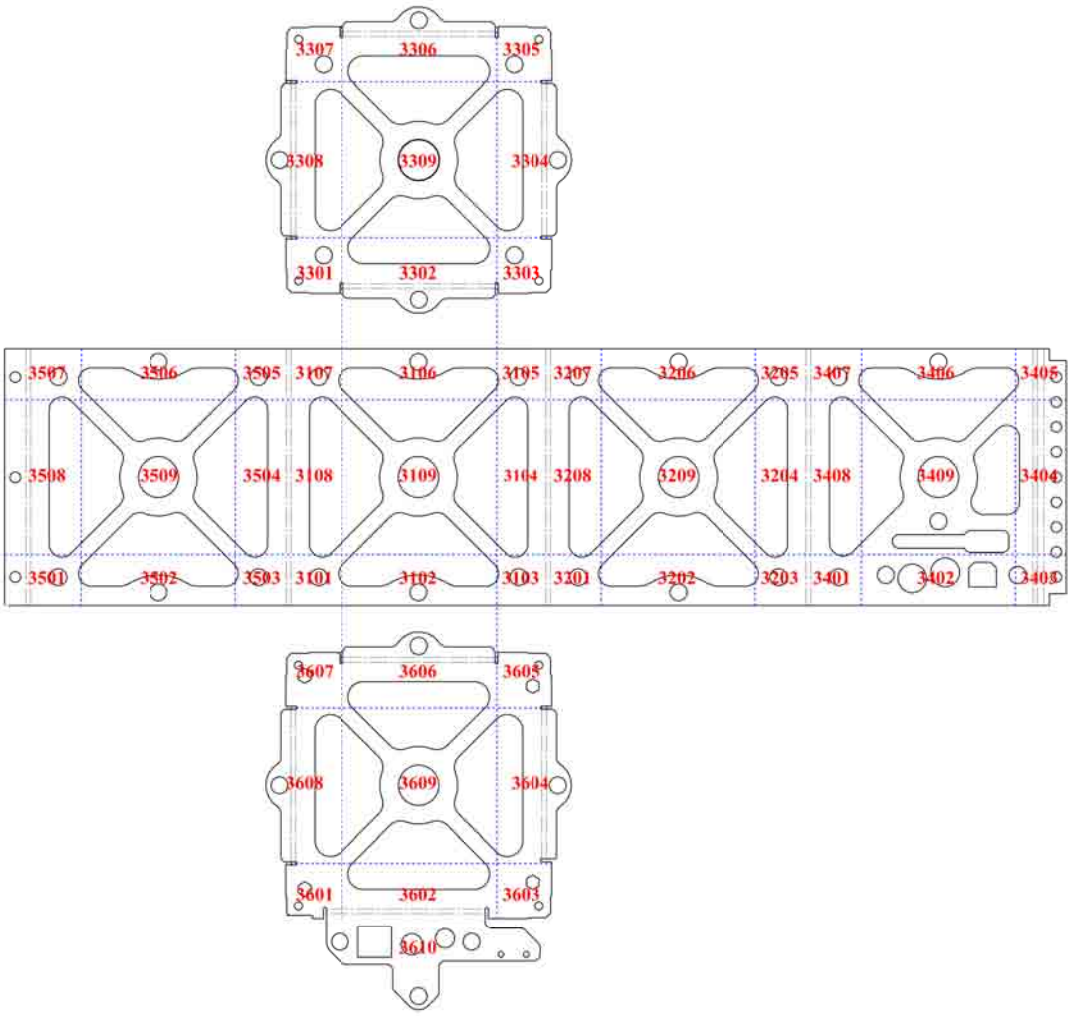

Figure 6.2 – *Detailed Thermal Model nodal breakdown of the aluminum frame*

nodes at the corners are smaller. The boundary between the corners and adjacent nodes is defined by the notch at the extremities of the folds of the faces 3 and 6, where it is narrower.

Figure 6.2 shows the nodal breakdown of the frame. The complete numbering convention is available in appendix **??**.

CubeSat's feets, visible in figure 6.1, are also modelled and included in nodes 3301, 3303, 3305 and 3307 for the upper face and 3601, 3603, 3605 and 3607 for the bottom face.

aluminum panels

To be consistent with the division of the frame, the aluminum panels are as well divided but in nine equal elements. Equal elements imply easier computation of the conductive links within the panel but more difficulties for the transverse links with the frame as this will be exposed later.

Solar cells

In the same way, each solar cell has now its own node. This model takes into account the cell efficiency variation but this will be treated in the TMM.

PCBs

Concerning the PCBs, their level of discretization depends on their components: high localized dissipative components requires a finer discretization. Another criterion was already spotted when considering the link with the secondary PCB sustaining the batteries : the transverse conduction within the PCB from main spacers at the corners has to be modeled.

And here are the level of discretization of each PCB, based on these two criteria:

- OBC & OBC2 : few nodes required because of low power, low dissipation ICs (integrated circuits) 2×2 elements.
- EPS : more nodes required because of transverse conduction modeling and high power, high dissipation ICs 10×10 elements such as the elements are about 1cm wide, approximatively the size of the dissipation transistor[51].
- EPS2 : because the case of hanging the battery PCB on EPS2 will be studied, more nodes are also required for transverse conduction modeling, even if it contains lower power ICs 10×10.
- COM : the only critical and high dissipation IC known at the moment is the amplifier. Nevertheless, the dissipated power level is such that a finer discretization is also required 10×10.

In this model, the connectors are modeled and added to the corresponding node as well as the spacers.

In practice, Matlab routines have been developed to make the discretization of each PCB entirely automatic and autonomous (both for the GMM and TMM) with only one input: the number of elements desired.

Antennas

This model includes the two antennas: the 17 cm and the 50 cm one. Once again, they are divided into several elements. Both antennas are 0.25 mm thick and 3.5 mm wide and are made of copper [63]. Since the antenna deployment mechanism panel geometry was not yet clearly defined when the model was created, it is only modelled with two nodes: one for the exterior and one for the internal side.

6.1.2 Thermo-optical properties

Thermo-optical properties are mainly the same as the ones used for the Simplified Thermal Model. The differences comes from the new elements taken into account :

- the emissivity of the batteries, set as parameter : the effect of covering the batteries with a low emissive tape will be investigated;
- the emissivity of the rails : the measured value of 0.7 (see previous chapter) is now used.
- antennas (copper) thermo-optical properties are: $\epsilon = 0.03$ and $\alpha = 0.3$ [24],[50]. Seeing their high α/ϵ ratio, antennas will probably be relatively hot.
- spacers (made of 6061 aluminum, machine finish) thermo-optical properties are set to $\epsilon = 0.05$ $\rho_{d,IR} = 0.15$ $\rho_{s,IR} = 0.8$.

6.1.3 ESARAD considerations

The nodal breakdown defined above suggests us to split up the ESARAD geometry in 3 main parts :

- an external skin comprising the solar cells, the aluminum panels, the antennas and the remaining visible aluminum frame (mainly the rails and the feet);
- an internal skin representing the environment seen by the PCBs : the aluminum panels and frame;
- the PCBs stack.

Figure 6.3 illustrates the GMM in ESARAD. As shown by the lower left picture, the particular geometry of the frame has been modelled. In this way, the aluminum panels and frame radiative coupling are consistent with reality.

6.2 Thermal Mathematical Model

6.2.1 Conductive network

aluminum frame

All the conductances of the frame have been determined through finite element analysis. The detailed procedure is available in appendix B.

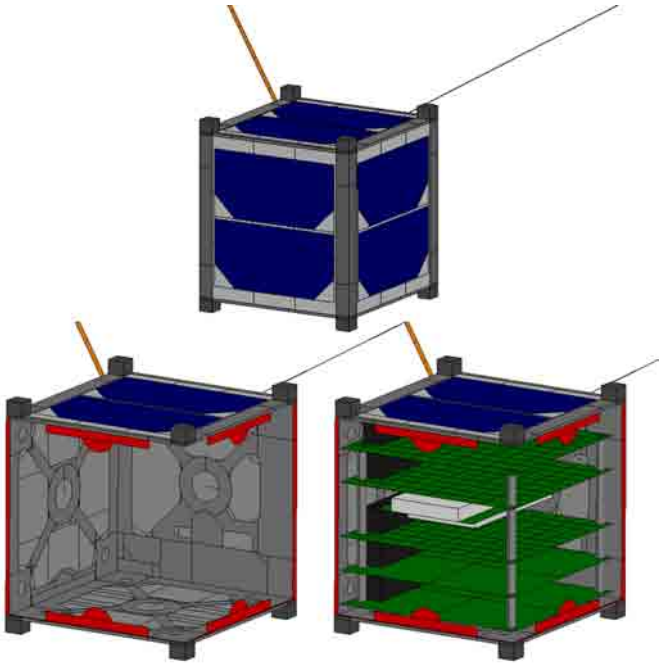

Figure 6.3 – *Geometric Mathematical Model in ESARAD*

Measurements confirmed the presence of contact phenomenon between the lateral frame and faces 3 and 6. Data about screwed-joints are difficult to find because they are often developed within companies and seldom published. The table of figure 6.4, coming from *Spacecraft Thermal Control Handbook* by D. Gilmore, shows contact resistance data[1] for various bolt size and plate thickness.

		Resistance Values from Several Sources (°C/W)[a]					
		TRW Large	LM Plate Thickness (mm)[c]				TRW Small
Bolt	Diam (mm)	Thin Surfaces[b]	(1.57)	(3.18)	(6.35)	(9.53)	Stiff Surfaces[b]
2-56	—	9.48	—	—	—	—	4.74
NC 4-40	2.8	7.59	12.6	—	—	—	3.79
NC 6-32	3.5	5.69	6.61	2.2	—	—	2.37
NC 8-32	4.2	3.79	4.5	1.5	0.75	—	1.25
NF 10-32	4.8	1.90	3.0	1.0	0.5	0.333	0.76
NF 1/4-28	6.4	0.95	2.1	0.7	0.35	0.233	0.28
NF 5/16-24	7.9	—	1.5	0.5	0.25	0.167	—
NF 3/8-24	9.5	—	—	0.39	0.194	0.128	—
NF 7/16-20	11.1	—	—	—	0.16	0.106	—
NF 1/2-20	12.7	—	—	—	—	0.089	—

[a]Bolted aluminum interface in vacuum, bare clean mill rolled surface finish (LM), standard steel bolts torque to specification (LM), primary heat transfer through compressed area near bolt (LM).
[b]TRW, March 1984.
[c]LM, George D. Rhoads, 20 July 1988.

Figure 6.4 – *TRW and Lockheed Martin Bolted-Joint Resistance Data [24]*

The fastening screws used are NC 4-40 (corresponding to M3 metric standard) and give, for thin plates (1.57 mm), a 12.6 [K/W] contact resistance.

[1] from TRW and Lockheed Martin

Aluminum panels

There are nine nodes per panel, except for the antenna deployment mechanism panel, equally distributed in both directions. The three lateral panels (faces 1, 2 & 5) are identical, as the top and bottom panels (faces 3 & 6). Horizontal/vertical conductances (respectively R_H and R_V) determination is then straightforward:

$$R_H = \frac{w}{k\,(th)} \qquad R_V = \frac{h}{k\,(tw)}$$

where $w = W_{panels}/3$, $h = H_{panels}/3$ and k the thermal conductivity of the 7075 aluminum panel.

Transverse links

The thermal modelling of transverse links between the frame and the panels and between the panels and the solar cells is relatively complex, mainly because the nodes are not directly opposed due to their different cross sections. But as the different layers are thin, one can assume that the flux lines remains perpendicular to the cross section, neglecting their extension (and thus the increase of the local cross section) in the larger layer. Therefore, the surface area involved in the thermal conductance formula ($GL = \frac{kS}{L}$) is taken as the smallest cross section of the two nodes. For example, considering the case of the figure 6.5 where the heat flux flows from the upper plate to the lower one, the surface S would be equal to S_1 and the length $L = (t_1 + t_2)/2$ (the nodes are set in the middle of each plate thickness).

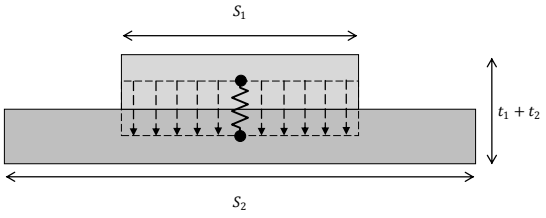

Figure 6.5 – *Thermal conductance between two thin plates of different section*

In practice, as the integration layouts (solar cells/panels and frame/panels) are the same for all the nodes, the transverse conductance is calculated according to the figure 6.6:

$$\frac{1}{GL_{ij}} = R_{ij} = \frac{1}{S_{effective}} \left(\frac{t_{cell}}{k_{cell}} + \frac{t_{adhesive}}{k_{adhesive}} + \frac{t_{Kapton}}{k_{Kapton}} + \frac{t_{adhesive}}{k_{adhesive}} + \frac{t_{panel}}{2k_{panel}} \right)$$

for the solar cells/panels links and

$$\frac{1}{GL_{ij}} = R_{ij} = \frac{1}{S_{effective}} \left(\frac{t_{panel}}{2k_{panel}} + \frac{t_{adhesive}}{k_{adhesive}} + \frac{t_{frame}}{2k_{frame}} \right)$$

for the frame/panels links where $S_{effective}$ is the common area between nodes i and j, as defined above, and is computed through CATIA V5 CAD software.

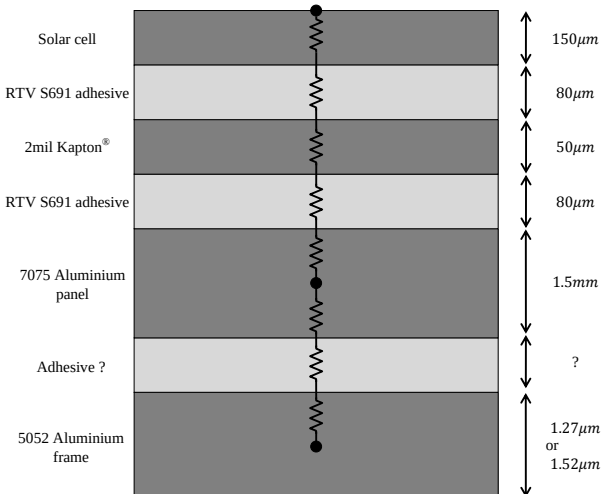

Figure 6.6 – *external layout and corresponding thermal conductance*

The adhesive thickness between the frame and the panels is not yet defined and the same values as the other adhesive layers are assumed.

Inner PCBs links

Now, the PCBs are divided into several elements, to take into account conduction inside the PCBs.

$$GL_x = \frac{k_{PCB}\left(t_{PC104} l_y\right)}{l_x} = \frac{k_{PCB}\left(t_{PC104} L_{PC104}\right)}{W_{PC104}}$$
$$GL_y = \frac{k_{PCB}\left(t_{PC104} l_x\right)}{l_y} = \frac{k_{PCB}\left(t_{PC104} W_{PC104}\right)}{L_{PC104}}$$

where $l_x = \frac{W_{PC104}}{N}$ and $l_y = \frac{L_{PC104}}{N}$ with N the number of elements in which the PCB is divided in both directions.

Inter PCBs links

Like in the STM, both spacers and bus conductances are taken into account. The drill holes at the corners of the PCBs consist of copper washers for heat rejection and structural purposes as depicted in figure 6.7.

The contact between the spacers and the washers is only ensured by the vertical pressure applied at the bottom of each endless screw, at the midplane standoffs. A contact resistance is thus added between the spacer and the PCB washer. The copper being a good thermal conductor ($k \approx 400$ [W/mK]), conduction through the washer is neglected, compared to the other resistances. Figure 6.7 describes the inter PCBs conductive model. Contact resistance is also added between the midplane standoff and the aluminum frame. OBC PCB is supported by steel inserted threaded spacers into which endless screws are fastened.

Conduction through the endless screws is neglected (large clearance with spacers and washers) but their heat capacity is distributed on the 4 corresponding spacers.

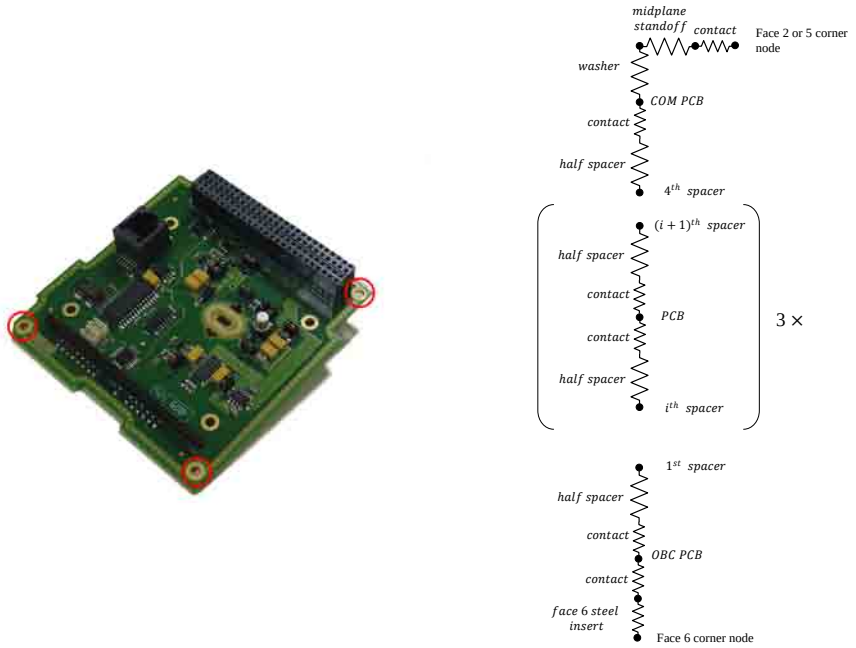

Figure 6.7 – *On the left, inserted copper washers in EPS2 engineering model. On the right, the inter-PCBs conductive model*

Concerning the connector, only the pins contributes to the conduction and perfect contact is assumed between the pins of consecutive connectors.

EPS PCB to battery PCB links

The way the BAT PCB is fastened to the other PCB was considered as aluminum spacers in the STM, with perfect contact. STM showed that insulating the BAT PBC by using spacers made of materials less conductive would be worthwhile. On another hand, STM also showed that the possibility of fastening the BAT PCB on the EPS2 instead of EPS should be investigated. Therefore, the conductance between the BAT PCP and the EPS or EPS2 PCB is kept as a parameter. The parameter who vary is the conductivity of the spacer, its geometry remaining unchanged. The default value corresponds to aluminum spacers.

Antennas

Antennas being divided into several elements, each node is linked to the previous and next node with the same conductance. The contact between both antennas and the panel is assumed to be perfect. The antennas are also linked to the amplifier through a coaxial wire. The corresponding conductance consist of a 5 cm long copper wire with a 1 mm diameter for both antennas.

6.2.2 Internal power

This section is devoted to the description of the internal power distribution which only concerns the hot case. But before distributing the

power, it must be collected: no power can be created out of nowhere and the section begins thus with the description of the solar cells.

Solar cells ef ciency

The way the electrical power is subtracted has already been exposed in the STM. But as previously introduced, this model takes into account the temperature dependence of the solar cells efficiency along with their degradation over time. The efficiency is assumed to vary linearly with temperature[1] according to the following law:

$$\eta(T) = \eta_0 + \frac{\partial \eta}{\partial T}(T - 28°\text{C})$$

where η_0 is the nominal efficiency at 28°C. However, data about the new solar cells are not yet available and the temperature coefficient is based on the 28% cells data, summed up in table 6.1 :

$$\frac{\partial \eta}{\partial T} = \frac{\partial}{\partial T}\left(\frac{P_{max}}{C_S A_{SC}}\right) = \frac{1}{C_S A_{SC}}\left(V_{max}\frac{\partial I_{max}}{\partial T} + I_{max}\frac{\partial V_{max}}{\partial T}\right)$$

where A_{SC} is the cell area and C_S the solar constant

		BOL	2.5E14	5E14	1E15
			aging factors [-]		
Average efficiency η_0	[%]	28	0.95	0.92	0.86
Voltage at P_{max}, V_{MP}	[mV]	2371	0.96	0.94	0.93
Current at P_{max}, I_{MP}	[mA]	487	0.99	0.97	0.94
dV_{MP}/dT	[mV/°C]	-6.1	-6.8	-6.3	-6.4
dI_{MP}/dT	[mA/°C]	0.28	0.36	0.2	0.29

Table 6.1 – *28% solar cells efficiency parameters [7], for* $C_S = 1367\ [W/m^2]$

The last three columns represent the effect of aging due to the radiation environment: the cells efficiency deteriorates over time because the space radiation environment affects the materials used in the cells. For instance, the coverglass transmittance decrease with the absorbed dose. The column headers are the fluence of 1MeV electrons received by the cell expressed in $[Electrons/cm^2]$. In those columns are the coefficients by which the efficiency, V_{MP} and I_{MP} must be multiplied, representing the deterioration over time. Concerning dV_{MP}/dT and dI_{MP}/dT, the values does not decrease monotonically over time and their values in function of the fluence are directly available without the use of an aging coefficient. Spenvis simulations show that, over our mission duration of one year, the fluence is 4.3E11 while over the predicted lifetime ($\approx$ 4.8 years), it is 2E12. However, since our solar cells are new ones with new aging coefficients still unknown and since they have not yet been tested in real space conditions the worst case value are used for the hot case. Figure 6.8 shows both effects of temperature and aging on the solar cells efficiency. The effect of deterioration is mostly visible on the nominal value of the efficiency but

[1]Note that the linear temperature dependence must surely be valid only in a given temperature range.

the effect of temperature is clear : the cooler the solar cell, the higher its efficiency.

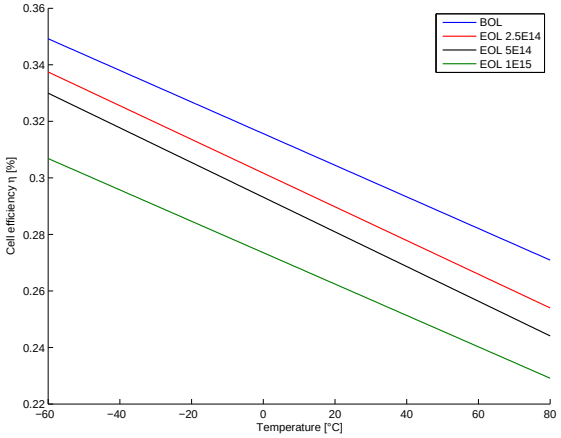

Figure 6.8 – *Effect of temperature and aging on solar cells efficiency*

Internal power distribution

Once the electrical power collected, a fraction is dissipated into heat because the electronic components are not perfect and have their own efficiency. However only the more dissipative and less efficient components are modelled: the dissipation system and the amplifier. At the time the STM was being developed, the dissipation system was composed of four resistances dispatched at the corner of the EPS PCB. Since that time, it has evolved and consists now in one transistor. The position of both elements is not defined and so subjected to optimization.

The cold case assumptions are identical to the one of the STM: all the collected energy is stored under sunlight with no internal dissipation throughout the orbit.

The hot case is somewhat different: now that a more detailed power budget is available and that a more accurate distribution can be realized, two different hot cases are considered. The first one assumes that the CubeSat is nearly turned off and that, the batteries being fully charged, all the collected power is dissipated through the transistor of the dissipation system.

The second one assumes that D-STAR is turned on involving a full utilization of the amplifier. According to the COM subsystem [36] and [28] and based on the link budget developed by MIAS [9], the power required on the antennas is about 750 mW. Assuming that the efficiency of the amplifier, not yet determined, is at worst 30%, this means that the amplifier dissipates 1.75 W into heat. Following back the power path, the amplifier input power ($0.75/0.3 = 2.5$ W) is provided by the converter whose efficiency is about 80%. Once again, this means that a part of the input power of the converter is converted into heat ($2.5/0.8 - 2.5 = 625mW$). OBC and OBC2 have relatively low power consumption and only 2×0.05

W are uniformly distributed on the two PCBs. According to [33], the inovative EPS dissipation is about 0.3 W and the remaining power is finally dissipated through the dissipation system.

	Hot Case 1		Hot Case 2	
P_{OBC} [W]	0		0.05	uniform
P_{OBC2} [W]	0		0.05	uniform
P_{EPS} [W]	P_{tot}	diss. tansist.	$0.625 + P_{rem}$	uniform
P_{EPS2} [W]	0		0.3	
P_{COM} [W]	0		1.75	amplifier

Table 6.2 – *DTM Hot Cases internal dissipation*

By default, both amplifier and dissipation transistor are located at the center of their respective PCB

6.3 Checking the model

This section is devoted to the check of both GMM and TMM.

6.3.1 GMM

As for the STM, the number of rays fired by the MCRT method has been selected after a convergence analysis for different *seeds* but is not represented here. In addition to that, an analytical estimation of the REF between two PCBs is carried out using Gebhart's theory and then compared to ESARAD results. Gebhart factors B_{ij} take into account multiple reflections and depend no longer only on the geometry like the view factors but also on the thermo-optical properties of the different surfaces. REF are directly obtained from the Gebhart factors B_{ij} thanks to the following relation:

$$GR_{ij} = \epsilon_i A_i B_{ij}$$

The analytical model includes two PCBs facing each other and divided in 10×10 elements. The bus and the spacers are neglected. The radiative coupling with the aluminum structure is modelled by closing the assembly with aluminum sides joining PCB perimeter.

Gebhart factors B_{ij} are defined by the equation:

$$B_{ij} = F_{ij}\epsilon_j + \sum_k F_{ik}(1-\epsilon_k)B_{kj}$$

or, in matrix form:

$$\mathbf{B} = \boldsymbol{\beta} + (\mathbf{F} - \boldsymbol{\beta}).\mathbf{B} \qquad \beta_{ij} = F_{ij}\epsilon_j$$

Details about the view factors computation is available in appendix C.

Figure 6.9 compares ESARAD MCRT and analytical results for one node of EPS2 PCB (16054) viewing COM PCB nodes (EPS2 and COM have the same number of nodes). The maximum REF is obviously with the opposite node ($GR_{16054,18054}$). The main differences occur at the border

because the analytical model does not take into account the connector, the gap between the PCB and the aluminum structure and the spacers. The REF with the corners is indeed lower because the node does not see them directly and the corners have an area reduced by the presence of the spacer. Apart these local differences, both surfaces are relatively identical and confirm that the number of rays fired is sufficient and that the REF computation through MCRT method has converged.

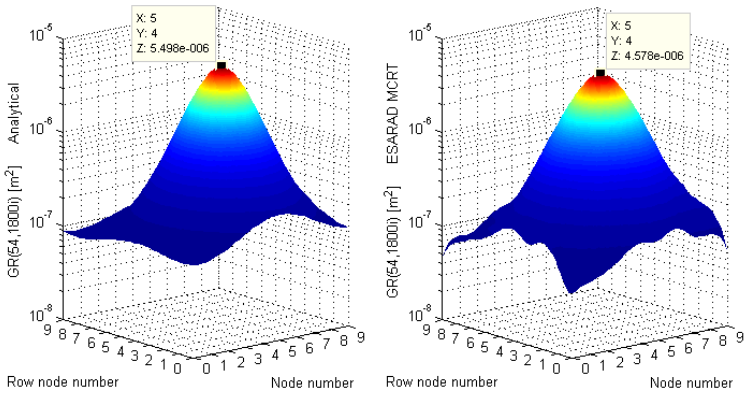

Figure 6.9 – *ESARAD radiative coupling check for one PCB node (left: analytical, right: MCRT)*

6.3.2 TMM

Moreover, being much more complex than the STM, checking the conductive network seemed necessary. For this purpose, three tests are carried out about different parts of the global conductive network: the lateral aluminum frame, the PCB inner links and the links between PCBs.

Aluminum frame

In order to check the lateral aluminum frame conduction, the temperature is prescribed on face 4 while power is injected on the opposite face. The temperature reached is then compared with a finite element model under the same conditions. The comparison is presented in figure 6.10[1]. It confirms that the way the nodes are distributed and connected is consistent with the accurate temperature distribution of the FEM.

PCBs

The PCB discretization is critical and therefore have to be tested. Three checks are indeed carried out to verify the good implementation of the conductive network. The first one concerns the verification of the links between the nodes inside each PCB. It is achieved by imposing a gradient across one diagonal of the PCB by prescribing the temperature of two opposite corners. By this way, one can verify the shape of the isotherms normally perpendicular to the heat flow. Figure **??** shows the results of

[1]For the sake of clarity, face 2 is undisplayed in ESARAD view.

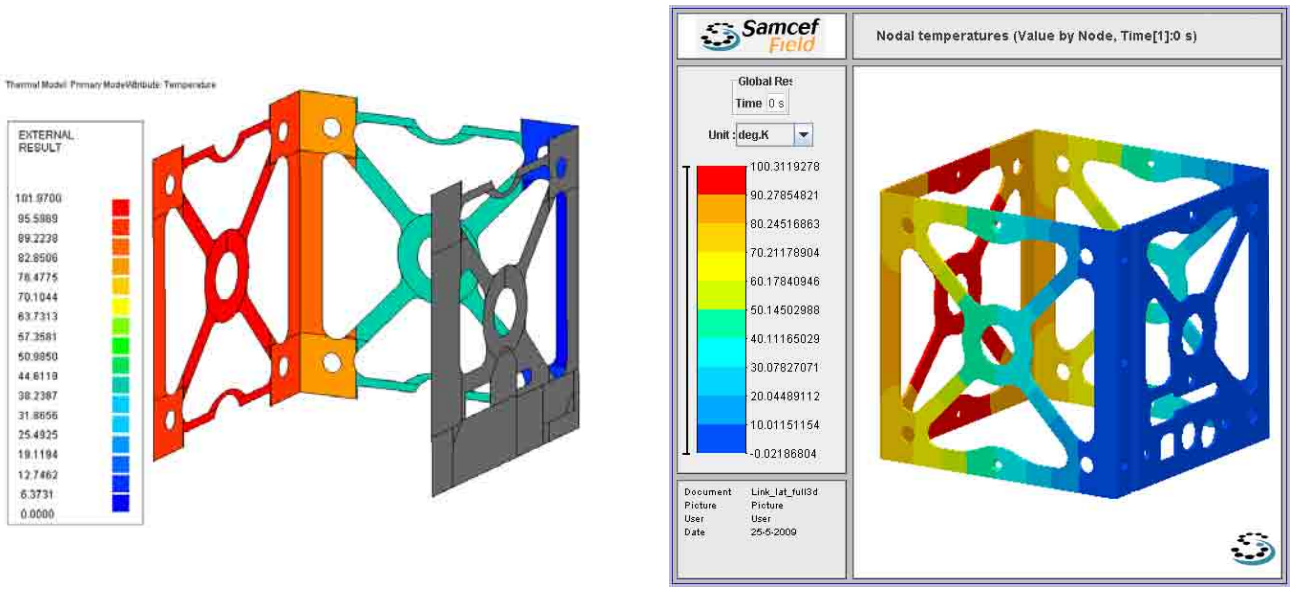

Figure 6.10 – *check*

this test. The shape of the isotherms are well as expected: nearly (because of the rectangular shape of the PCB) perpendicular to the diagonal of the PCB.

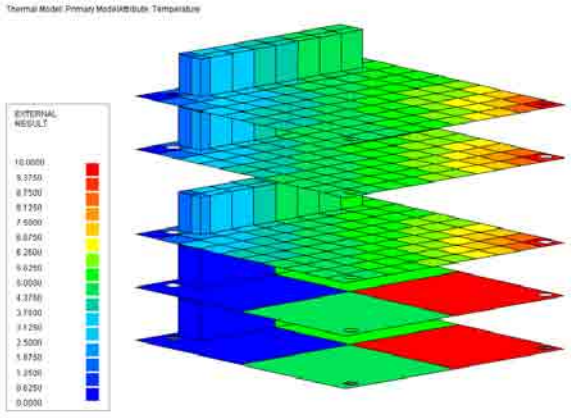

Figure 6.11 – *Checking the conductive links inside PCBs through isotherm shape*

The second test concerns the links through the connectors. The automatic implementation is quite difficult because the number of elements of two consecutive PCBs may be different (for instance, the links between OBC2-EPS). The way these links are tested is the following one: power is injected on EPS PCB while both OBC and COM have a prescribed temperature at their extremity. The temperature reached where the power is injected is then compared to an simple conductive network, depicted in figure 6.12. The temperature reached at the end of the EPS PCB, T_2, is obtained thanks to the following relation, deduced from the resistance model:

$$T_2 = T_1 + Q\left(R_{EPS} + \frac{(R_{OBC} + R_{s1} + R_{s2})\,(R_{COM} + R_{s3} + R_{s4})}{R_{OBC} + R_{s1} + R_{s2} + R_{COM} + R_{s3} + R_{s4}}\right)$$

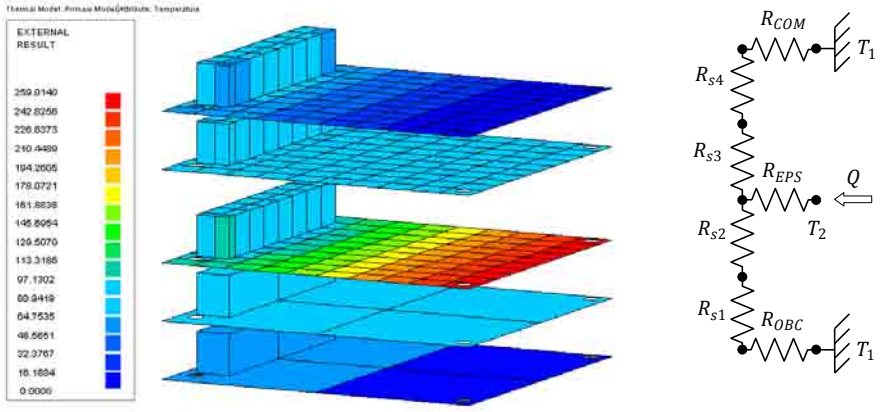

Figure 6.12 – *Check of the conductive links through the bus and equivalent resistance model*

where

$$R_{EPS} = R_{COM} = \frac{L_{PC104}\frac{n}{n-1} - W_{BUS}/2}{k_{PCB}t_{PC104}} \qquad n = 10$$

$$R_{OBC} = \frac{L_{PC104}\frac{n}{n-1}}{k_{PCB}t_{PC104}} \qquad n = 2$$

$$R_{s1} = R_{s2} = R_{s4} = \frac{15\ mm}{k_{spacer}A_{spacer}}$$

$$R_{s2} = \frac{25\ mm}{k_{spacer}A_{spacer}}$$

For $T_1 = 0$ °C and $Q = 5$W one gets $T_2 = 261.2$ °C while ESATAN gives 259 °C.

The global convergence of the TMM has been analyzed through the different convergence parameters ()

6.4 Results

Now that the DTM is checked, concrete simulations can be launched to analyze this initial design.

6.4.1 Absorbed powers

Figures 6.13 and 6.14 show the different contributions to the total power absorbed by the satellite during one orbit in the cold and hot cases, respectively. They are nearly identical to those of the STM except that slightly more power (for instance, 20.2 W instead of 19.8 W in the hot case) is absorbed because of the antennas and feet contributions. Nevertheless, important differences will be observed in the temperatures thanks to the better accuracy of this thermal model.

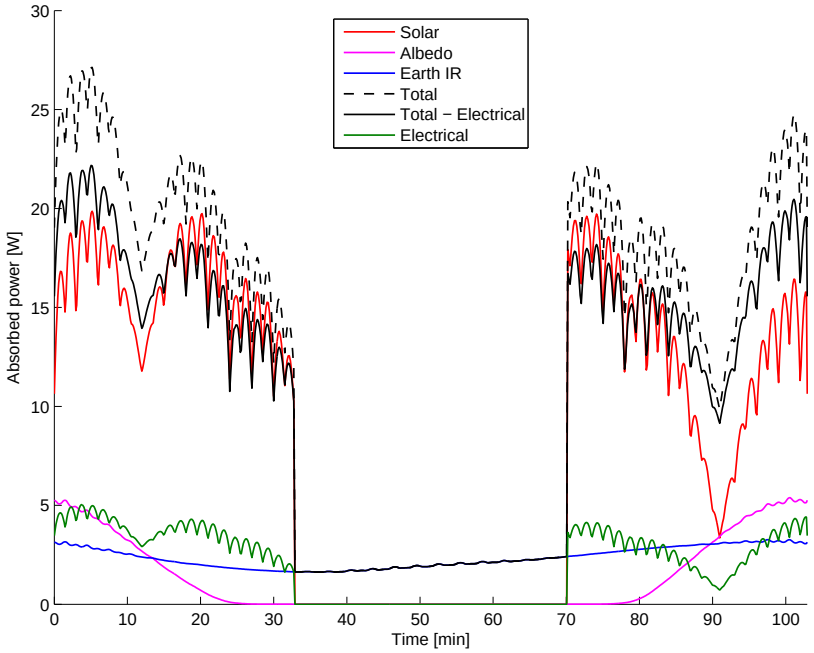

Figure 6.13 – *Cold case absorbed power*

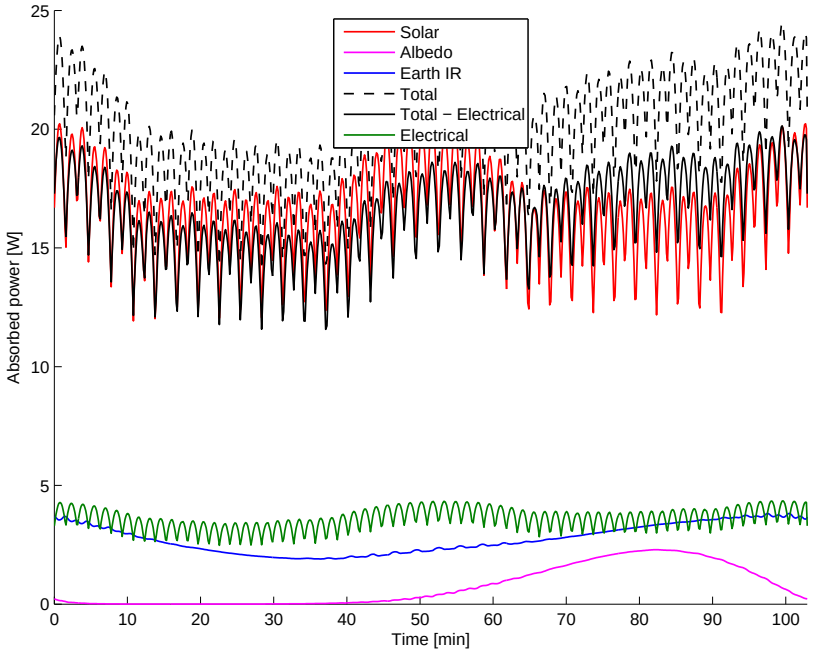

Figure 6.14 – *Hot case absorbed power*

6.4.2 Cold Case

Since the STM showed that the most critical components in the cold case were the batteries, they are the only internal part represented in Figure **??** showing also the temperature evolution and solar cells. The first key difference with the STM is clearly visible: if one reminds that the temperature of the batteries dropped to -21°C in the STM, it drops now only to -15°C. This translates the effects of transverse conduction within the PCBs (here the EPS) and contact with spacers both increasing the total thermal resistance between the batteries and the structure.

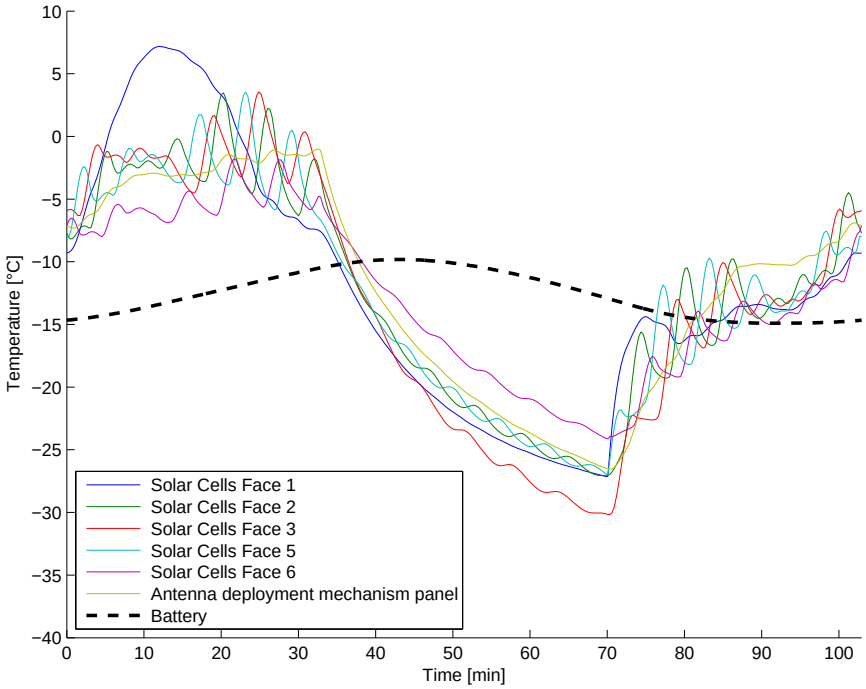

Figure 6.15 – *Cold case absorbed power*

Yet, this temperature is still too cold and heaters are required. But before beginning the design of the heater, the two hot cases have also to be considered to keep a global point of view and allow a global design.

6.4.3 Hot Case 1

The STM showed that a steady-state analysis using the mean absorbed powers would possibly be equivalent and much more time effective than a transient computation. Indeed, as expected viewing the similarities in the absorbed powers of STM and DTM, a comparison with transient analysis confirmed that the steady-state one was equivalent and that the fast variations of the absorbed powers does not influence the mean results. From now, steady-state analysis are then performed for the hot case instead of transient, requiring much more cpu time.

As described in the table 6.2, the first hot case assumes that all the collected power is dissipated through the dedicated transistor.

While the heat flow path are not critical in the cold case because there are no internal dissipation and because the structure does not undergo large thermal gradients, a heat flow map is more useful in the hot case. Therefore, we created a Matlab routine that generates automatically the heat flow map from ESATAN output file to synthesized the results.

Figure 6.16 summarized the results of the first hot case. Each of the twelve components represented in this diagram involves several underlying nodes so that temperatures and heat flows are averaged. All the external parts of the CubeSat are at the top while the PCB stack is at the bottom, encircled by the red dotted rectangle. The three red arrows represent the total effective power exchanged radiatively between the PCBs and the external parts. The different radiative exchanges occurring between the PCBs are not represented but can be estimated by differentiating the power incoming and leaving conductively one PCB being approximatively equal to the power evacuated radiatively by the PCB.

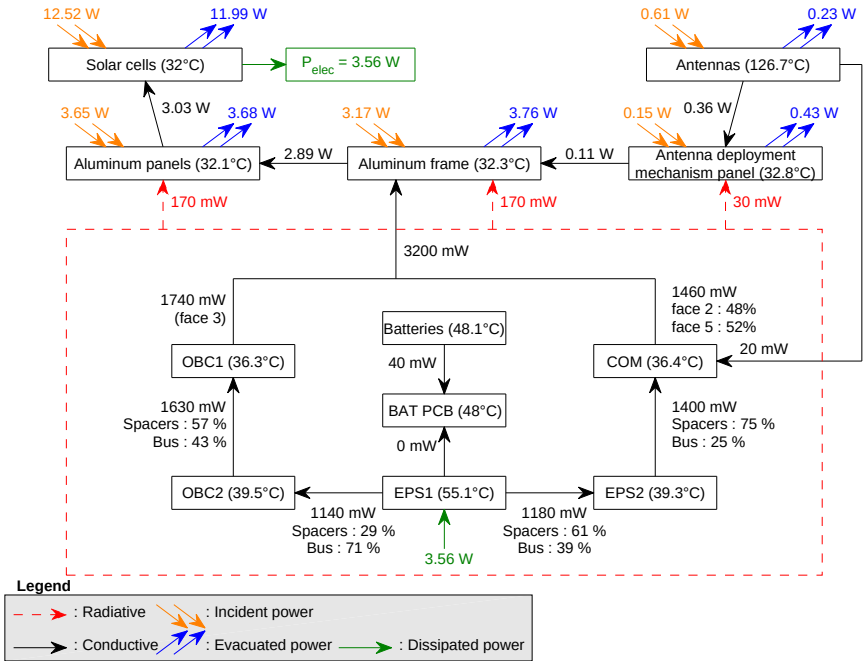

Figure 6.16 – *Hot case 1 heat ow map*

This diagram leads to the following observations:

- The links joining the PCBs gives also the distribution of the heat flow between the spacers and the connector. This highlights that both are as important as the other.
- The solar cells are the most exchanging surfaces rejecting nearly as much power as they receive (about 12 W).

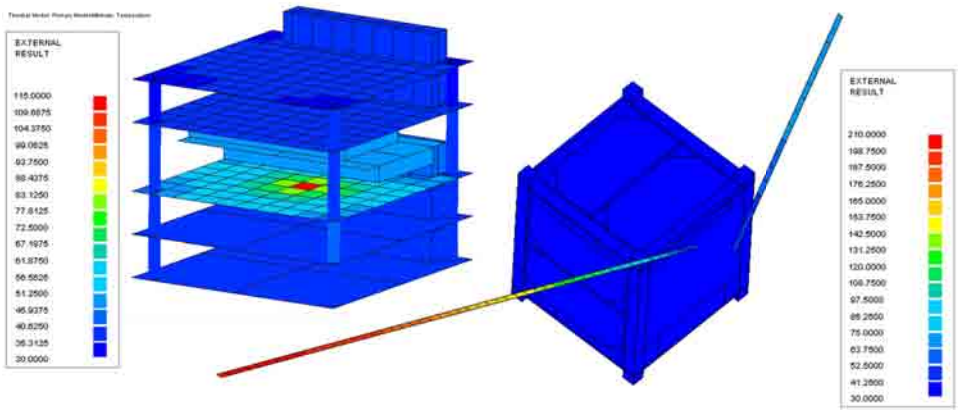

Figure 6.17 – *Hot case 1: Hot spot due to the dissipation transistor and temperature distribution on the antennas*

- The mean electrical power collected is more than 3.5 W and is directly and entirely dissipated on the EPS.
- The global radiative exchange between the PCB stack and the structure is small compared to conductive one: about 10% (0.37 W / 3.22 W).
- Antennas are quite hot: their mean temperature is about 125°C but the corresponding panel remains cold. 20 mW flow through the coaxial cable to the amplifier. Figure 6.17 (right) details the temperature distribution on the antennas and shows that the maximum reached temperature occurs at the extremity: about 200°C.
- Hot spots are not visible on this diagram but the mean temperature of the EPS PCB is 55°C while other PCB's temperature ranges from 35 to 40°C. The left picture of Figure 6.17 shows that the temperature near the transistor rises up to 115°C.
- The batteries are out of their allowed range of temperatures (in charge): 48°C. It is worst than that was predicted by the STM, mainly because the hot case is different (in the STM, the dissipated power was simply divided between the COM and the EPS because a more accurate distribution was not available)
- The conductive heat flux between EPS and BAT PCBs is null on average because the four spacers balance each other.
- The total conductive heat flux flowing through the bus and spacers increases from EPS PCB to the outer PCBs because the radiative heat flux between to consecutive PCBs is added at each step.

6.4.4 Hot Case 2

When analyzing the second hot case where the dissipated power is less localized, one observes that OBC, OBC2 and EPS PCBs are cooler on average while EPS2 and COM are hotter (Figure 6.18). Concerning the structure, it has approximatively the same temperature as the first hot case

except for the antennas panel being a little hotter, like the antennas. This is due to the amplifier and the coaxial cable, through which 300mW (of the 1750mW dissipated by the transistor) flows. These are approximate numbers because the coaxial cable is assumed to be directly connected to the amplifier.

The batteries are cooler than in the first case but yet remain unacceptably close to the 45°C allowed temperature in charge.

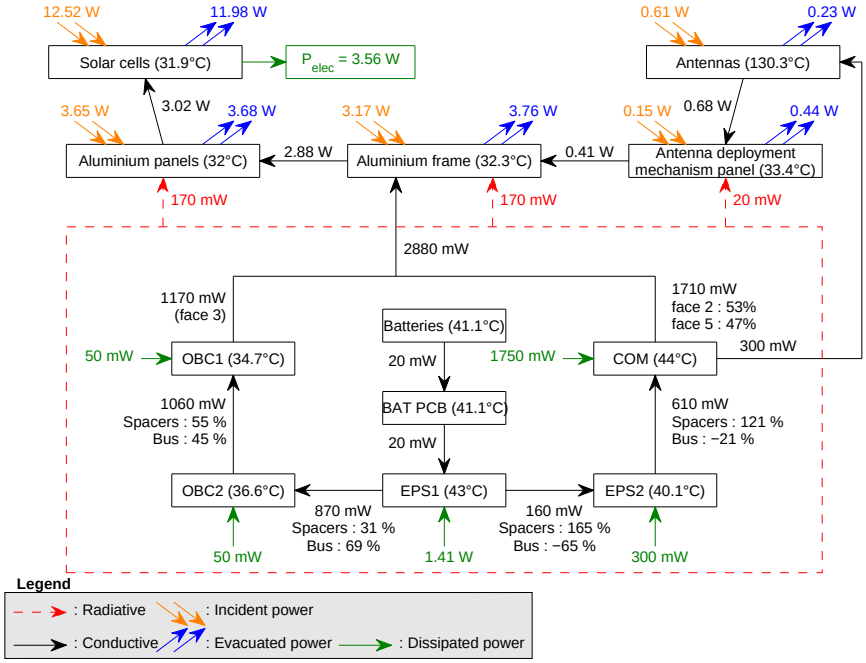

Figure 6.18 – *Hot case 2 heat ow map*

Little loops in the heat flow also appears, for instance between EPS1 and EPS2 where 160mW flows effectively from EPS1 to EPS2 but 264mW through the spacers and 104mW through the connector in the opposite direction. These local effects could not be revealed in the precedent thermal model.

Figure 6.19 shows the local hot spots on EPS and COM PCBs. By default, the amplifier is located at the center of the PCB. With its efficiency of only 30% involving a 1.75W dissipated power, the temperature of the amplifier reaches 70°C. Once again, this temperature is relatively close to the upper limit of the industrial temperatures range (+85°C) and must be carefully looked at.

6.5 Parametric analysis and design

Previous results have confirmed two problems already spotted thanks to the STM but revealed two others. The four issues for which solutions have to be found are namely:

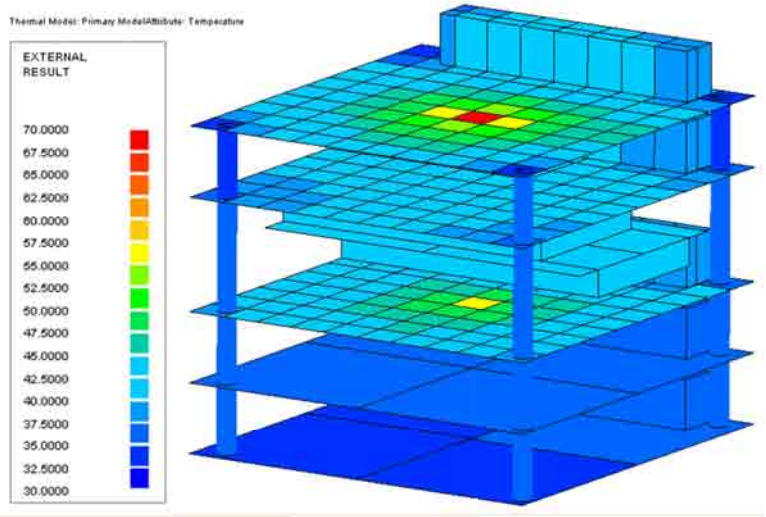

Figure 6.19 – *Hot case 2: Hot spots due to the dissipation transistor and amplifier on COM PCB*

1. In the cold case, the temperature of the batteries drops below its acceptable lower limit at the end of the eclipse. An this is indeed the more critical time: when they come into sunlight and get recharged, involving the narrower range of temperatures (0 +45°C). A efficient way of heating the batteries will thus be investigated in this section.

2. In the hot case, when maximal dissipation occurs, the temperature of the batteries is too high. A way to enhance heat rejection must be found to reduce the temperature reached by the batteries

3. The second issue concerns the dissipation transistor. According to its datasheet, the main problem is not the transistor itself because it is designed to support such temperatures but the components close to it. Nevertheless, avoiding hot spots and reducing the temperature of the EPS PCB would be favorable for the transistor as well as for the batteries.

4. In the second hot case, the amplifier reaches too high temperature. Nevertheless, as the amplifier is not yet determined and could be much more efficient (like the ADL5541 linear amplifier which has a constant 0.5 W power dissipation [4]), concrete measures should not be taken before a better definition of the amplifier because they could be inadequate if it was effectively more efficient. This problem will thus not be plainly investigated in this work but should be as soon as more information about the amplifier are available.

6.5.1 Cold case issues

The main problem of the cold case is the temperature of the batteries dropping to -15°C when the satellite comes out of the eclipse, time at which the batteries begin to charge again. This is thus the lower limit of the charge temperature range that must be considered *i.e.* 0°C.

The use of a heater seems the easiest and more convenient way to prevent the temperature from dropping below this limit. Nevertheless, when designing a heating system, several questions arise:

- How perform the control of the heater?
- What is the required power?
- Because the response is obviously not instantaneous, the batteries will keep getting cooler a short time after the heater is switched on. Then what is the optimal threshold below which it is turned on?
- The power generated by the heater is not entirely accumulated in the batteries: there are losses which does not participate to the heating of the batteries. How to reduce these losses and thus increase the heater efficiency?

Concerning the way to control the heater, two options are possible. The first one involves the On-Board Computer (OBC) and allow to take into account other criteria in addition to the temperature of the batteries such as their voltage. The decision of whether it is wise to heat the batteries when they are already nearly discharged is then more complex. The second way of control consist in bypassing the OBC and develop an independent and autonomous control loop. After many discussions with the other subsystems and other CubeSat teams, we preferred the second solution: a too cold battery is useless even if it has a low voltage and it is more reliable in case of OBC failure (the heating system is still operational and the batteries can still feed the beacon). Figure 6.20 illustrates the decreasing efficiency and capacity of a typical LiPo battery (here the KOKAM SLPB723870H4) with the temperature. The -10°C and 0°C curves illustrate than a heating system is well required.

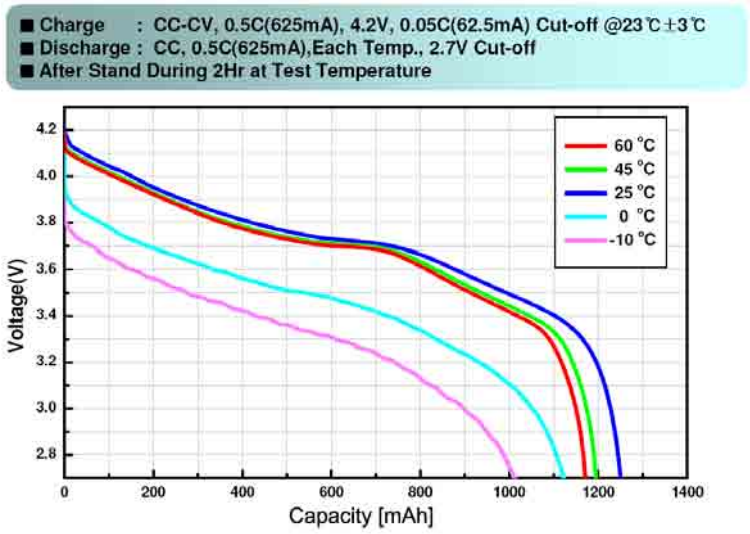

Figure 6.20 – *Battery temperature profile of a typical LiPo battery, here the KOKAM SLPB723870H4 [32]*

Moreover, EPS [55], EPS2 [33] designed the batteries in such a way that their capacity should not drop below 70%, and this has been confirmed by MIAS simulations.

Figure 6.21 shows the resulting control loop including the sensor and the heater: if the temperature of the batteries drops under a given threshold, the heater is switched on until the batteries are again within its allowable temperature range.

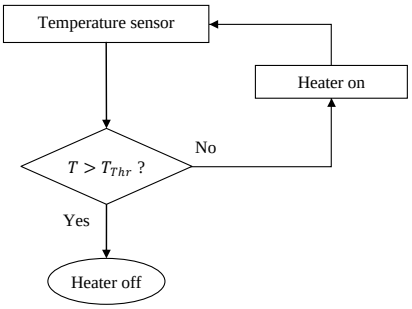

Figure 6.21 – *Heating system control ow chart*

As the batteries are located on either side of the BAT PCB, we decided to use two separated redundant heaters in parallel with two sensors to increase the reliability of the system. Actually, a third sensor should be used: if two sensors give different temperatures, the third one enables the defective sensor determination. On another hand, using two identical heaters in parallel ensures that if one fails, the other is still operational.

To answer the three other questions about the required power, threshold and losses reduction, parametric analyses are performed. Diminishing the losses is achieved by insulating the batteries and their PCB. As early presented in this work, only two ways of heat transfer occur in space: radiation and conduction (except when considering aerothermal flux or specific thermal control means such as fluid loops or phase-change materials). From this observation, two corresponding ways of insulating the batteries have been foreseen and investigated:

- covering the batteries with an aluminum tape (low emissivity) to reduce radiative losses,
- and using insulating materials for the fasteners to reduce conduction losses.

Aluminum tape is easy to use and largely used in space applications. According the the Sheldahl Red Book p.33 [52], Sheldahl's first surface aluminized polyimide tape with 966 acrylic adhesive has a low emissivity ($\pm$ 0.03) is low outgassing and would be suitable.

Concerning the BAT PCB fasteners, usual insulating materials are thermoplastics such as PTFE (Teflon®) or PA (polyamide such as nylon) but these have poor structural properties and outgassing must be carefully looked at. Fully replacing the initial aluminum spacers by a thermoplastic materials must then be avoided because the BAT PCB undergoes strong dynamic amplifications (being in the center of the CubeSat, fastened to another PCB). Furthermore, structural integrity could be weakened because of the creep phenomenon. For those reasons, in agreement with STRU subsystem, here is the outcoming design depicted in Figure 6.22. Structural integrity is enforced by titanium spacers and screws (high tensile strength

and Young's Modulus to thermal conductivity ratio) in addition to thin nylon washers, reducing creep issues and increasing thermal insulation. Nylon has been preferred because of its higher Young's Modulus.

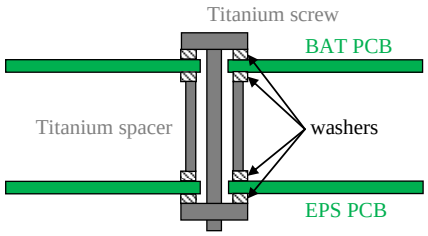

Figure 6.22 – *Batteries' PCB fastening concept*

The resulting insulation gain can easily be evaluated in considering only the main heat transfer through the spacer (conduction through the screw is neglected because of poor contact around the nut) and a perfect contact between the PCBs and washers. The equivalent resistance compared to an aluminum spacer of the same dimensions is far much greater:

$$R_{alu} = \frac{L_{spacer}}{k_{alu}\ A_{spacer}} \quad \& \quad R_{eq} = \left(\frac{L_{spacer} - 2\ t_{washer}}{k_{titanium}} + \frac{2\ t_{washer}}{k_{washer}} \right) \frac{1}{A_{spacer}} = \frac{L_{spacer}}{k_{eq}\ A_{spacer}}$$

This defines the equivalent thermal conductivity which will be used as parameter:

$$k_{eq} = \frac{k_{washer}\ k_{titanium}}{k_{washer}(1-\gamma) + k_{titanium}\ \gamma}$$

where $\gamma = \frac{2\ t_{washer}}{L_{spacer}}$. According to CES software, the thermal conductivity of PA (nylon 6.6) is 0.24 W/mK. Based on this value, the Figure 6.23 shows the influence of the washer thickness and thermal conductivity of the spacer. The left plot demonstrates that 0.5 to 1 mm thick washers already reduce efficiently the conduction and using thicker washers would be useless. The right plot shows that for thick washers (above 1 mm), the thermal conductivity of the spacer is less influent than for thinner washers. For instance, considering 0.5 mm thick washers replacing aluminum ($k = 150$ W/mK) by titanium ($k = 10$ W/mK, CES Edupack value) reduce the equivalent thermal conductivity from 3.5 to 2.7 W/mK, *i.e.* a 23% gain.

Eventually, considering 0.5 mm thick PA washer combined with titanium spacer, the global thermal conductance is now equal to 1.32 10^{-3} W/K while the initial one, with the aluminum spacer, was 73.5 10^{-3} W/K. The conductance is thus divided by a 55 factor.

Now that solution have been proposed, their concrete effects are studied. After implementing the heating system in ESATAN, the insulation benefit is quantified. The threshold is set to 5°C and the heater power is varied (the total heater power for the two batteries). Figure 6.24 shows the minimum temperature reached on the batteries in function of the heater power for different insulating configuration. The effect of radiative insulation is clearly observed: for a same equivalent thermal conductivity

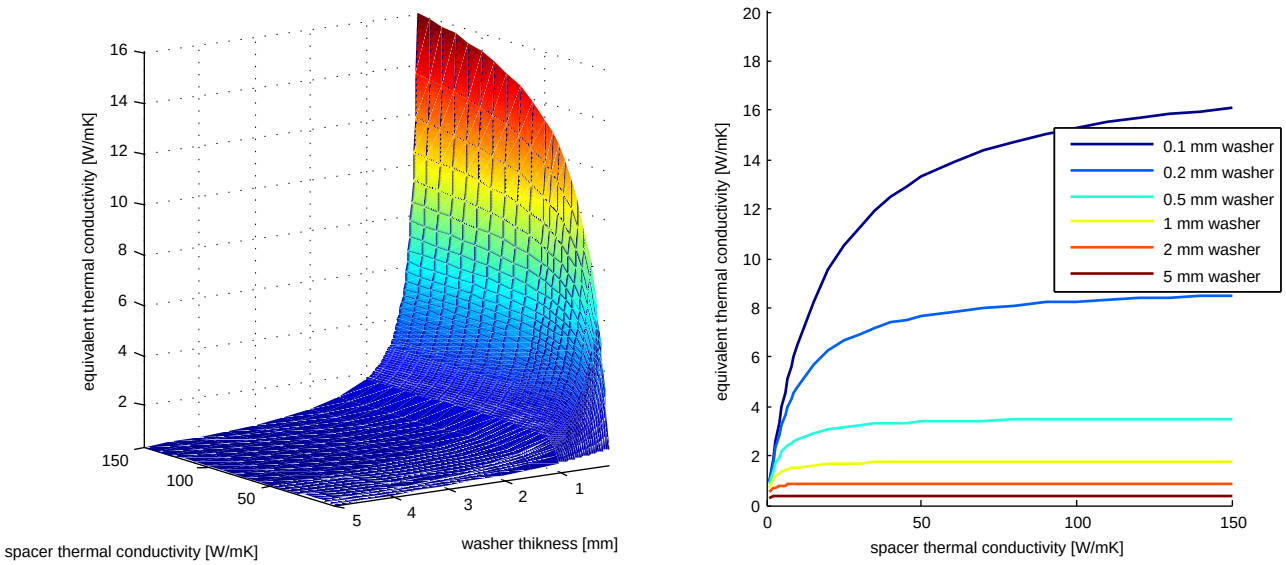

Figure 6.23 – *Equivalent conductivity of BAT PCB fastening in function of the PA washer thickness and thermal conductivity of the spacer*

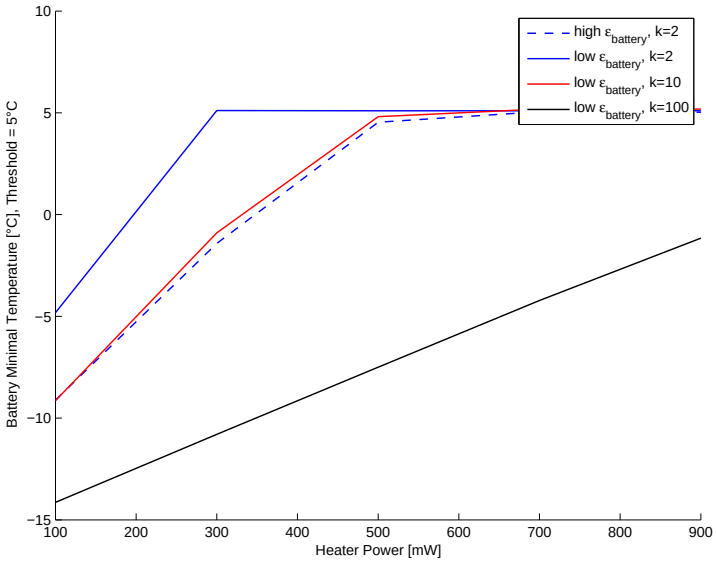

Figure 6.24 – *Effect of insulating the batteries on the heater required power for a given threshold [5°C]*

(2 W/mK) the blue doted line corresponding to the high emissivity (the initial value considered for the batteries was 0.8 *i.e.* plastic) shows that a more than 500 mW heater is required to reach the threshold. On the other hand, reducing the emissivity of the batteries through aluminum

tape ($\epsilon = 0.03$) lowers the required power to 300 mW. Not reducing the emissivity of the batteries is nearly equivalent to increase the equivalent thermal conductivity to 10 W/mK as shows the red curve. Finally, the black curve demonstrate that even a 1W heater would not be sufficient if the conductive insulation is not achieved. Figure 6.24 also shows that increasing the insulation of the batteries increases the heater sensibility ($\frac{dT_{batteries}}{dP_{heater}}$): the slope of the 2 W/mK curve (blue) is greater than the slope of the 10 W/mK or 100 W/mK one (before the threshold is reached).

Two of the four initial questions have been answered. The remaining two questions concern the required power and the switching threshold. Three parameters are looked at in this study:

- the minimal temperature reached by the batteries to verify that the power is sufficient,
- the time during which the heater is turned on,
- and the consumption of the heating system.

The consumption of the heating system is computed as follows: the energy of the battery is given by its capacity, given in mAh. The power generated by the heater is thus multiplied by the time during which it is turned on and then divided by the voltage.

$$C = \frac{P\ t}{U}\ [mAh]$$

The heater will be directly connected on the batteries to enhance reliability. The voltage is therefore not constant because it is not converted by one of the EPS converter. Figure 6.20 showed that the maximum voltage is 4.2 V while cut-off voltage is 2.7 V. The worst case corresponds therefore to the minimum voltage: a 2.5 V has been assumed to be conservative.

Figure 6.25 shows the evolution of the three parameters presented above in function of the power and for different thresholds. Top plot confirms that the lower the threshold, the low the require power to reach it. Bottom plot shows that reducing the threshold and increasing the power reduces the time the heater is turned on. For a 500 mW heater, the time it is turned on can be reduced to 35 to 50 min, depending on the threshold, *i.e.* $\approx$ 35 to 50% of the orbital period (104 min) while the maximum eclipse time is about 35 % of the orbital period. The middle plot shows that the increase power resulting in a reduced consumption time balance each other once the threshold is reached: the capacity curves are approximatively horizontal (due to computation error of the consumption time[1]) after that point. Middle plot also shows that reducing the threshold from 5 to 0°C allows to save 40 mAh.

Nevertheless, the thermal sensors and heater have a finite accuracy and LiPo battery's characteristic curves illustrated in Figure 6.20 suggest therefore that sufficient safety margins to cope with these uncertainties combined to the model and environmental uncertainties. The 40 mAh consumption that could be saved by reducing the threshold remains quite

[1]The time the heater is on is obtained through the post-processing of the ESATAN output file. The time the heater is turned on consequently depends on the output time step, set here to 360 points per orbit

small compared to the nominal 1000 to 1500 mAh capacity of the foreseen batteries, recalling that the worst case has been assumed with the 2.5 V voltage.

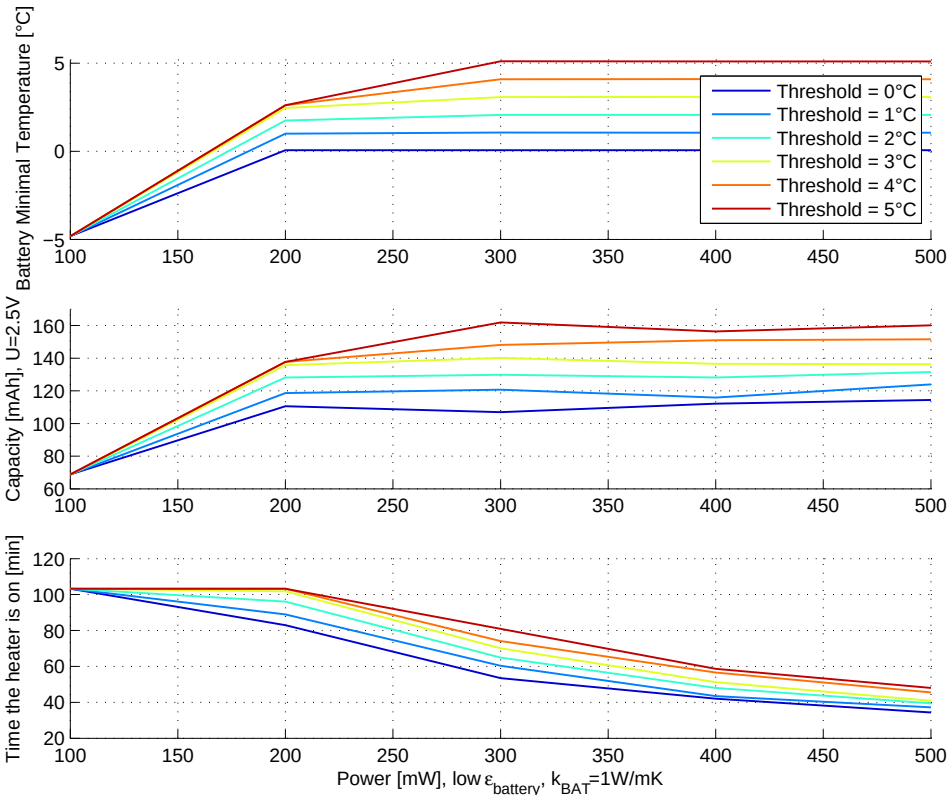

Figure 6.25 – *Evolution of the battery minimal temperature, batteries' capacity decrease (worst voltage U=2.5 V) and time the heater is turned on in function of the heater power for different thresholds*

For the sake of reliability, the threshold shall be set to 5°C and we shall use a 500 mW heater. For the same reason, instead of using one heater for the two batteries, each battery shall have its own heater as previously stated. The 500 mW have to be divided into two 250 mW heaters. Figure 6.25's top plot shows that even if one fails, the remaining 250 mW are able to ensure that the batteries' temperature will not go below 0°C.

Moreover, vacuum tests have been conducted by EPS subsystem on different batteries (KOKAM and Varta) to verify their functionality in their allowable temperature range. Results are available in the test report [34]. A persistent deformation has been noticed on both models so that batteries should be packed. In addition to that, even if this was not the subject of these tests, heating has also been noticed under discharge. Figure 6.26 illustrates increase of temperature: about 5°C whereas the batteries are fastened to a temperature controlled panel through a nitrogen loop. The same phenomenon has been observed for the VARTA PoLiFlex® battery. However, the determination of the generated power is impossible through this data because this was not the purpose of this test. Nevertheless, the conclusion is that the batteries undergo a self heating during discharge

which is favorable: when supplying the heaters, additional heat is automatically generated inside the batteries.

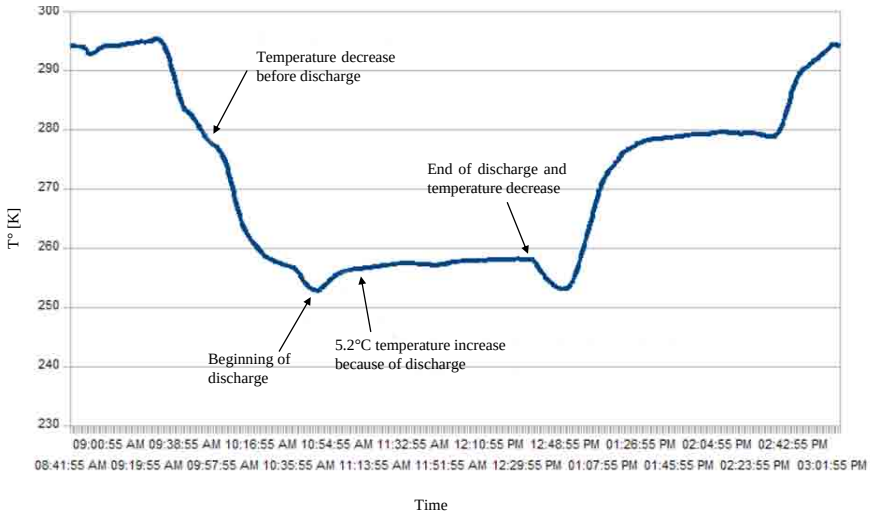

Figure 6.26 – *Temperature of a SLB 603870H KOKAM battery during the cold test [34]*

To determine the resistance of the heaters, the lowest voltage is once again assumed. Using Ohm's law, the electrical resistance is equal to

$$R = \frac{U^2}{P} = \frac{2.5^2}{0.25} = 25\ [\Omega]$$

As the battery model is still unknown, it is difficult to determine the heater model. However, based on the typical dimensions of the different foreseen models, we found the following MINCO reference [40]: XHK5377R26.3L12B where

- X means low outgassing ink
- HK stands for polyimide heater
- 5377 specifies for the model size and shape: 35.6 $\times$ 59.4 mm rectangular shape
- R26.3 specifies the resistance value : 26.3 ω (This was the closest value from the one defined above corresponding to the dimensions of the batteries)
- L12 is the lead length in inches (12 inches is the standard length, other length are possible on demand).
- B specifies Pressure-sensitive adhesive (PSA)

If it appears that the batteries should be packed in a thin aluminum box with epoxy resin, adhesive could possibly be removed (XHK5377R26.3L12A).

6.5.2 Hot case issues

In order to deal with the hot case issues, three solutions have been investigated:

1. In agreement with the EPS subsystem, we suggested to relocate a part of the power initially dissipated through the transistor by adding a resistance in series with the transistor and fastening it onto the antenna deployment mechanism panel. For this purpose, the use of an adhesive Minco Thermofoil™ heater [40] seamed convenient thanks to their easy integration and wide range of shapes. The EPS subsystem determined that the ideal resistance to prevent the transistor from depolarizing was 2.4 Ohms. Because this resistance value was not available among suitable shapes, we decided to use two 4.7 Ω resistances in parallel, involving a equivalent resistance of 2.35 Ω. With this configuration and according to the EPS subsystem, the power distribution between the equivalent resistance and the transistor is depicted in Figure 6.27. The bottom plot shows that the power dissipated by transistor is already divided by two for the 3.5 W mean collected power computed and shown in Figures 6.18 and 6.16.

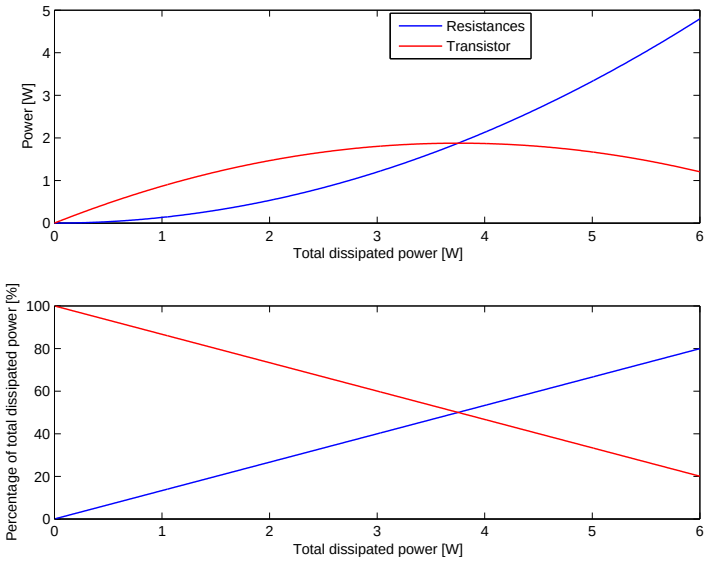

Figure 6.27 – *Power distribution in the equivalent resistance and the transistor of the dissipation system*

2. To reduce the temperature of the batteries, the second possible solution investigated, as already introduced, is to fasten the batteries' PCB to the EPS2 PCB instead of the EPS one because the EPS2 PCB is less dissipative and cooler. The effect of insulating batteries' PCB, as introduced above for the cold case issues, is also investigated. Two equivalent thermal conductivities are considered: 150 W/mK (full aluminum spacers) and 2 W/mK (combination of titanium screws

and spacers with Nylon or PTFE washers). As radiative insulation has proved to be useful in the cold case, low emissivity is assumed (batteries covered with aluminum tape).

3. The third solution is to use a thermal strap between the transistor and the antenna deployment mechanism panel, in agreement with STRU and MECH subsystems. We designed a copper angle bracket that would be strongly bolted on the EPS PCB with two M3 bolts, encircling the transistor, then located close to the face 4. Figure 6.28 shows the angle bracket in red encircling the transistor (left) on EPS PCB engineering model and a CATIA model illustrating the two adhesive resistances and angle bracket configuration.

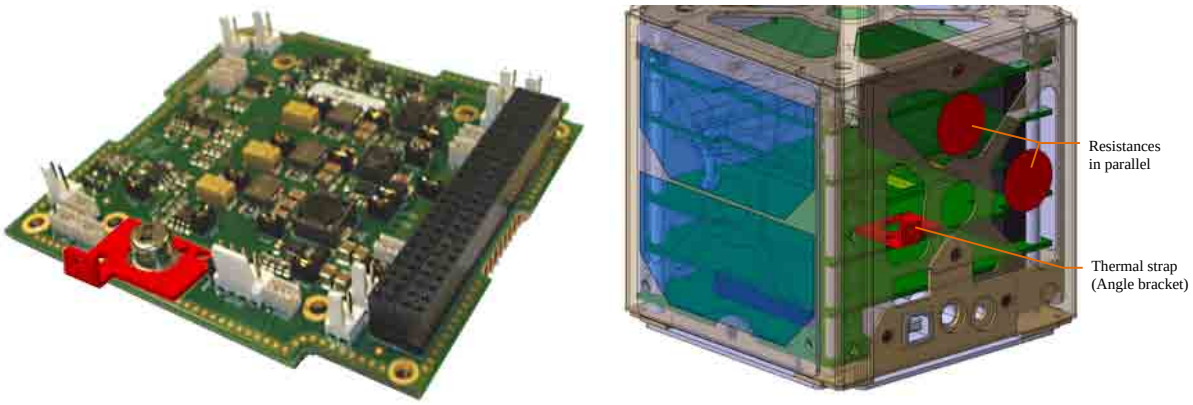

Figure 6.28 – *Thermal strap (angle bracket in red) design on engineering EPS PCB (left) and its fastening configuration with the relocated resistances on antenna panel (CATIA Model on the right)*

The effects of these three solutions are summarized in Table 6.3 for the different combinations. A combination is described through the first four columns in which are given the PCB to which the BAT PCB is fastened (EPS/EPS2) and the fastening equivalent thermal conductivity (k_{BAT}) the strap column shows whether the transistor is strapped to the antennas' panel or not. The different combinations are compared through the batteries and transistor temperatures. The effect of relocating a part of the power through the two Minco resistances is given in the last two columns.

The first row recalls the initial design (first two columns) and shows the effect of the relocated power without any other change. The transistor temperature is reduced by a 1.5 factor while a 7°C battery temperature decrease is already achieved.

The next eight rows assumes that the batteries are covered with aluminum tape as it has proved to be useful when examining the cold case. Among these eight rows, the first half gives the temperature for the different combinations without strap. The effect of the equivalent thermal conductivity starts to be significant when the BAT PCB is fastened to EPS2

and a higher thermal conductivity would be preferred if it should not be avoided for the reasons exposed in the cold case analysis. This can be easily explained: the heat radiatively received by the batteries must be evacuated to reduce their temperature. A slight increase of the transistor temperature is also noticed.

The second half of the table shows the results when the thermal strap is added and demonstrates that the combination of the strap with the Minco resistances can reduce the temperature of the batteries to 35°C and the temperature of the transistor to 67°C, *i.e.* less than 60% of its initial value. Even if fastening the batteries' PCB to EPS2 does not appear to be anymore worthwhile when strapping the transistor, reliability and uncertainties suggest to combine both solutions.

				without resistances		with resistances	
	strap	EPS/EPS2	k_{BAT} [W/mK]	$T_{batteries}$ [°C]	$T_{transistor}$ [°C]	$T_{batteries}$ [°C]	$T_{transistor}$ [°C]
high ϵ_{bat}	no	EPS	150	**48**	**114**	41	75
low ϵ_{bat}	no	EPS	150	48	115	41	76
	no	EPS	2	47	115	40	77
	no	EPS2	150	39	115	36	77
	no	EPS2	2	45	115	39	77
	yes	EPS	150	38	94	37	67
	yes	EPS	2	37	95	35	67
	yes	EPS2	150	35	95	34	67
	yes	EPS2	2	36	95	**35**	**67**
	high aluminum panel ϵ (0.8)						
high ϵ_{bat}	no	EPS	150	46	112	43	80
low ϵ_{bat}	no	EPS	150	47	113	43	80
	no	EPS	150	35	94	34	66

Table 6.3 – *Effects of the different solutions to the hot case issues*

To make the temperature more uniform inside spacecraft, black paint is usually used on internal structure elements to increase their emissivity (being low because spacecraft's structure is usually made of aluminum). On OUFTI-1, only the aluminum panels can be coated with a black paint because Pumpkin Kit's Structure is not intended to be modified. The emissivity of the 6 aluminum panels has therefore been set to 0.8 (inside) and the results are available in the last three row of Table 6.3 for three combinations: the nominal case, the nominal case with batteries covered with aluminum tape and the final design.

High emissivity on both aluminum panels and batteries allow a 2°C decrease of the batteries and transistor temperatures in the nominal design and a 1°C decrease if the batteries are covered with aluminum tape.

In the last combination, black paint enables another 1°C decrease. A black coating of the aluminum panels implies therefore not enough significant changes in the temperature to be worthwhile.

Finally, Figure 6.29 shows the heat flow map resulting from the modifications discussed above *i.e.* strapping the transistor to the antennas' panel, relocating of a part of the dissipation system power and insulating the

batteries with aluminum tape. It shows that nearly one half of the power is relocated and that 1 W of the 1.78 W remaining dissipated power on the transistor is directly evacuated through the strap and less than 1 W has still to be evacuated through the spacers. The power incident to the amplifier is however slightly increased because the antennas' panel is hotter (80 mW instead of 20 mW)) but this has no significant effect on the temperature of the amplifier. Table 6.4 summarized the achieved temperatures. We also verified that EPS2 fastening has no significant effect on the heating system.

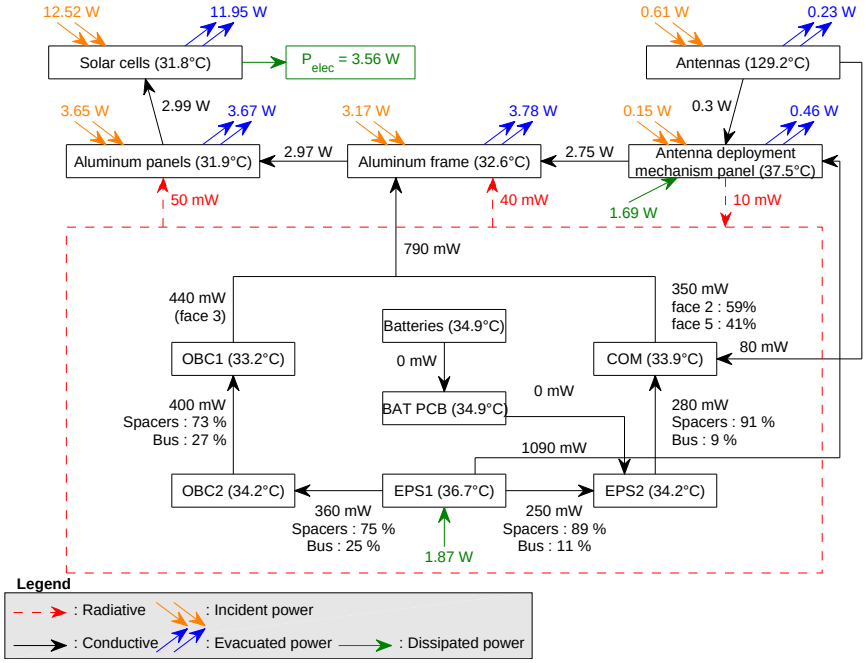

Figure 6.29 – *New design hot case heat ow map*

Concerning the COM amplifier, because too high uncertainties remains about the dissipated power, no design modifications were investigated. We only studied the effect of the location of the amplifier on the PCB and its dissipated power. To avoid numerous costly ESATAN simulations, the parametric analysis has been carried out through some simplifications. Radiation is neglected and the PCB is assumed to be an insulated plate subjected to some boundary conditions and internal heat loads. Using the finite difference method, this kind of problems can be reduced to a single matrix equation:

$$\underline{\underline{A}}\,\underline{T} = \underline{g}$$

where $\underline{T}$ is the $1 \times n$ vector containing the n temperatures of the discretized problem, $\underline{g}$ the heat loads incident on each node and $\underline{\underline{A}}$ is a $n \times n$ matrix represents the conductive coupling between the nodes. For the sake of clarity, the underlying equations are not detailed here but are available in appendix E.

Element	T°before [°C]	T°after [°C]
Solar cells	32	32
Aluminum panels	32	32
Aluminum frame	32	33
Antennas' panel	33	38
Antennas	127	129
OBC PCB	36	33
OBC2 PCB	40	34
EPS PCB	55	37
EPS2 PCB	39	34
COM PCB	36	34
Batteries	**48**	**35**
Dissipation Transistor	**114**	**67**

Table 6.4 – *Comparison of hot case temperatures before and after modifications*

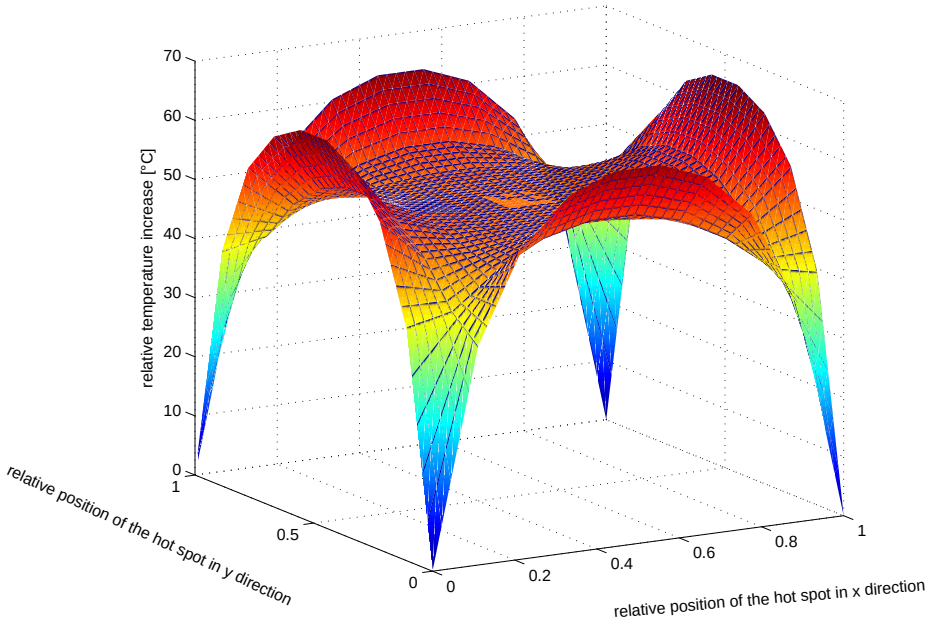

Figure 6.30 – *Amplifier temperature increase in function of its relative location on the COM PCB*

Based on this model, the COM PCB has been discretized and the temperatures of its four corners are supposed to be constant which is not far from reality. The effect of local heat dissipation has been studied in function of its location on the PCB. Figure 6.30 shows the temperature increase on the amplifier in function of its relative position on the PCB. The dissipated power is maintained at 1.75 W. The worst locations involving the greater increase of temperature are the center of the four edges of the PCB. But getting closer to the corners reduces the temperature of the amplifier. It is worthwhile to notice that setting the amplifier at the center of the PCB is not the worst situation (50°C temperature increase in comparison to the

corner's temperature) and that this corresponds indeed to the temperature observed in ESATAN results (Figure 6.19), 75°C while the temperature of the corners is about 30°C, *i.e.* a 45°C increase. One must bear in mind that the bus has been neglected as well as the radiative exchanges, which explains the difference.

The use of another amplifier such as the ADL5541 linear amplifier which dissipates a constant 0.5 W power [4] has also been investigated. The resulting temperature increase drops down to only 15°C at the center of the PCB (and the reached temperature given by ESATAN is about 45°C).

Summary

The Detailed Thermal Model, far much complicated and computation-time costly than the previous one, has however proved worthwhile. The issues already revealed by the Simplified Thermal Model became more tangible and evident. On another hand, the present model enable new issues detection, especially in the hot case. The four issues that have been confirmed or revealed are namely:

- the too cold batteries in the cold case;
- their too high temperature in the hot case;
- the hot spot due to the dissipation transistor;
- the too high temperature reached on the amplifier.

Concrete measures have been taken to solve three of these four issues. Only three because too many uncertainties still surround the COM amplifier. However, we stated that the efficiency of the amplifier should be taken into account when selecting the amplifier. For instance, using the ADL5541 could reduce the temperature down to 45°C.

A heating system has been designed to cope with batteries' too cold temperature. Two 250 mW heaters in parallel, one for each battery, are required to maintain the temperature above the threshold, which shall be set to 5°C because of sensor and comparator finite accuracy. Bearing in mind the problems encountered by Compass-1, we suggest to use three temperature sensors for reliability purposes. Insulating the batteries has proved to be required to reduce losses and consequently increase the heating system efficiency. The foreseen Minco heaters has not yet been ordered because the definitive battery model is not defined. However, even if the batteries are not defined, comprehensive tests should be conducted to validate the design a evaluate the sensors and comparator accuracy.

Concerning the hot case, the problems were involved by the dissipation system. Two main measures have been investigated to reduce both batteries and dissipation transistor temperatures: an angle bracket encircling the transistor and fastened to antennas' deployment mechanism panel already allows a 10°C temperature decrease of the batteries (from 48°C to 38°C) and 20°C of the transistor (from 115°C to 95°C). In addition to that, a part of the dissipated power is now relocated through two resistances in parallel also fastened to the antennas' panel. This involves another 3°C and 30°C temperature decrease of the batteries and transistor, respectively

reduced to 35°C and 67°C. Once again, tests should be conducted to evaluate the real efficiency of these measures.

Testing 7

In the previous chapters, the different models revealed that the temperatures of some components go beyond their limits. Thanks to the Detailed Thermal Model, proper measures have been taken to ensure those components remain within their temperature limits. However, unlike electronic equipments that can be ground tested, the thermal behavior of a satellite is very difficult to verify on Earth. This behavior can thus only be predicted by thermal analytical methods and can only be fully verify once it is in orbit.

Consequently, thermal modeling involves many assumptions and uncertainties and the design relies on a worst case approach. Tests are thus essential for the verification and to ensure the satellite achieves all the requirements.

This chapter intends to describe the tests that shall be performed at the Centre Spatial de Liège (CSL). First, the different test and model philosophies are presented. The chosen one is then detailed and the corresponding temperature ranges are defined. Next, the typical test hardware is explained along with the foreseen set-up.

7.1 Test and model philosophy

For several decades, many documents have been written to standardize definitions, tests requirements and methods, especially for military space vehicles. Those documents also introduced test categorization and levels. Today, three test categories are established:

1. Engineering or Development Tests are conducted throughout a satellite design in each subsystem to validate new design concepts or perform measurements to reduce uncertainties.

2. Qualification Tests are conducted to demonstrate that the design implementation and manufacturing process have resulted in hardware and software that meets specification requirements with sufficient margins.

3. Flight Acceptance (FA) Tests are conducted to verify conformance to specification requirements and provides quality-control assurance to detect workmanship deficiencies, manufacturing errors or any latent defect that would be detected by by normal inspection techniques. Acceptance tesing is less severe than qualification testing and

are conducted under environmental conditions no more severe than those expected during the mission.

It is important to note that items which have undergone qualification testing are usually not eligible for flight because the remaining life regarding fatigue and wear is not demonstrated. However, tight schedules, budgetary constraints are such as a dedicated nonflight qualification model is not always feasible. For this reason, alternative test strategies and tradeoffs have been developed to reduce the risks involved by this situation. These alternative strategies introduce higher risks compared to the nominal test program constituted of the acceptance test following the qualification one but increasing safety factors and development tests can mitigate the induced risks.

The main alternative strategy is protoqualification (or protoflight) testing. The tested protoflight model (PFM) is thus considered eligible for flight. Protoflight testing accomplishes thus in one test the combined purposes of design qualification and flight acceptance and results from a combination of the two strategies. Protoflight eliminates the redundancy of building a qualification hardware, enables significant cost saving and is thus well suited for student projects. This is the adopted strategy for OUFTI-1. However, a second Pumpkin's CubeSat Kit have been bought for the engineering tests and model. It is therefore on the second CubeSat Kit that measurements of chapter 5 were performed.

The above strategies concerned both thermal and vibration tests. More specifically, thermal test are divided into three tests:

1. a Thermal Vacuum Test (TV) is performed under vacuum and subjects the satellite (or equipment) to worst hot/cold temperatures including adequate margins. Its purpose is the performance verification through functional testing because it is the most realistic ground simulation of the in-orbit environment.

2. a Thermal Cycling Test (TC), that can be performed under ambient pressure, subjects the satellite (or equipment) to a series of cycles of hot and cold temperature plateaus. Its main purpose is to reveal latent workmanship defects due to environmental stress.

3. a Thermal Balance Test (TB) is generally conducted as a part of the thermal vacuum test. It has two primary purposes: demonstrate the ability of the thermal control system to maintain temperatures within the specified operational limits and provide data for the TMM correlation.

These three tests can be combined in one test called thermal vacuum cycling test during which the TB test is also performed.

7.2 Tests specifications

Now that the tests have been introduced and before describing them in details, temperature ranges and margins terminology is presented. As previously introduced, the thermal model relies on several assumptions and uncertainties. They can be categorized in three main classifications:

1. Environmental uncertainties: albedo, Earth IR and direct solar fluxes depending for instance on solar activity, clouds coverage...

2. Spacecraft physical uncertainties: thermo-optical and thermal properties of the materials, interface conductances...

3. Mathematical models (both GMM and TMM) uncertainties: the temperatures of the spacecraft are governed by a set of nonlinear differential equations for which no closed integration solution is available and numerical solutions are employed based on finite difference methods. These methods have intrinsic uncertainties:

   - The definition of finite, isothermal elements is physically incorrect.
   - Conductive and radiative exchange between these isothermal elements are only approximated (Monte-Carlo Ray Tracing, thermal resistance across different section...).
   - Numerical integration of the differential equations system is subjected to tolerances and consequently has only a finite accuracy.

To account for these uncertainties, safety margins are applied to the worst case predicted temperatures. The resulting temperature forms the basis for the acceptance temperature range. To this acceptance temperature, extra margin are added for protoqualification testing. Qualification temperature range are usually the same as the protoqualification one but additional qualification margins can be added to increase environmental conditions over that expected during the lifetime. Qualifications margins may also include the cycles duration as well as any other increase in severity to demonstrate the robustness of the design.

Figures 7.1 and 7.2 illustrates the different temperature range and margin terminology for European and NASA/JPL programs respectively. They are quite identical in the fact that acceptance range is obtained by adding thermal control uncertainty margins (thermal design margins) and residual margins (FA thermal reliability margin in NASA/JPL). The qualification range accounts for a 10°C to 15°C additional margin.

Now that the qualification temperature range is clearly defined, two other temperatures are used in the following figures and need to be defined: the non-operating temperature (max and min) which are the highest/lowest temperature for an equipment to survive unpowered and the start-up temperature which is highest/lowest temperature of the equipment, at which it can be switched on.

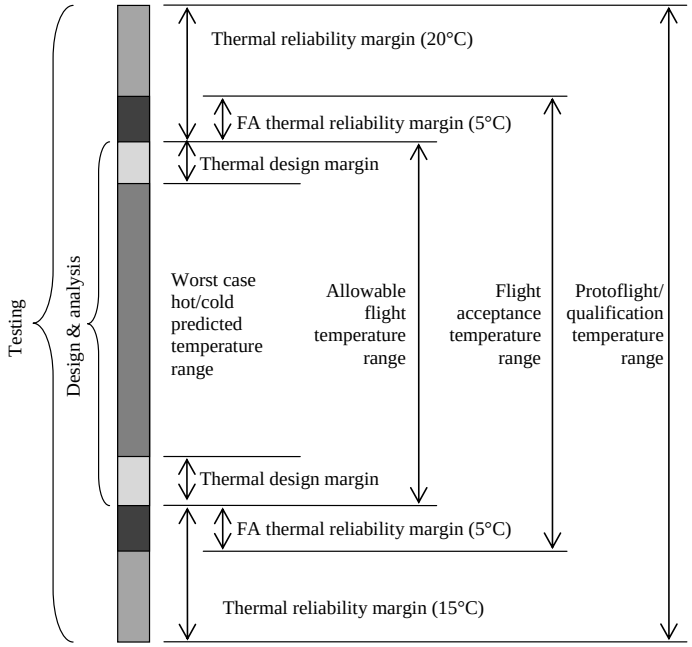

Figure 7.1 – *Thermal margin terminology for NASA/JPL programs [24]*

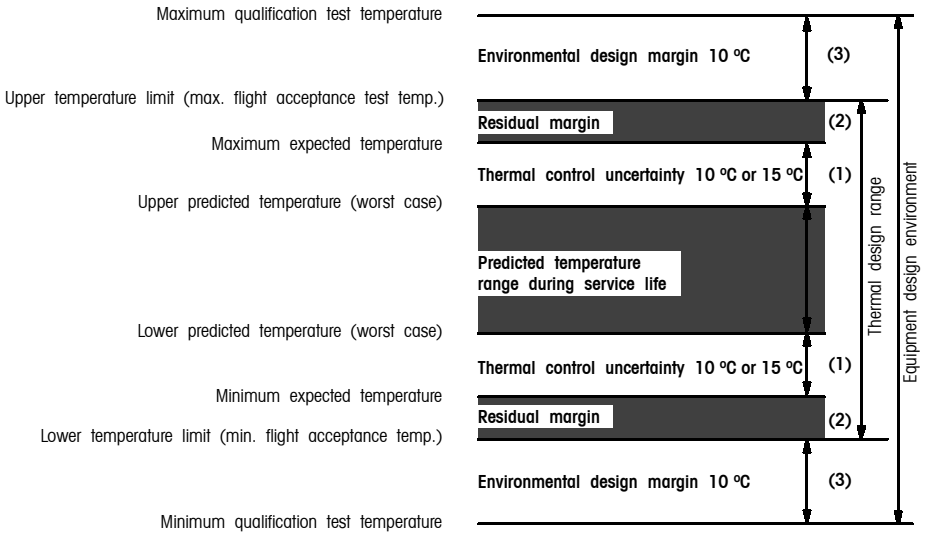

Figure 7.2 – *Thermal margin terminology from ECSS-E-10-03A standard [17]*

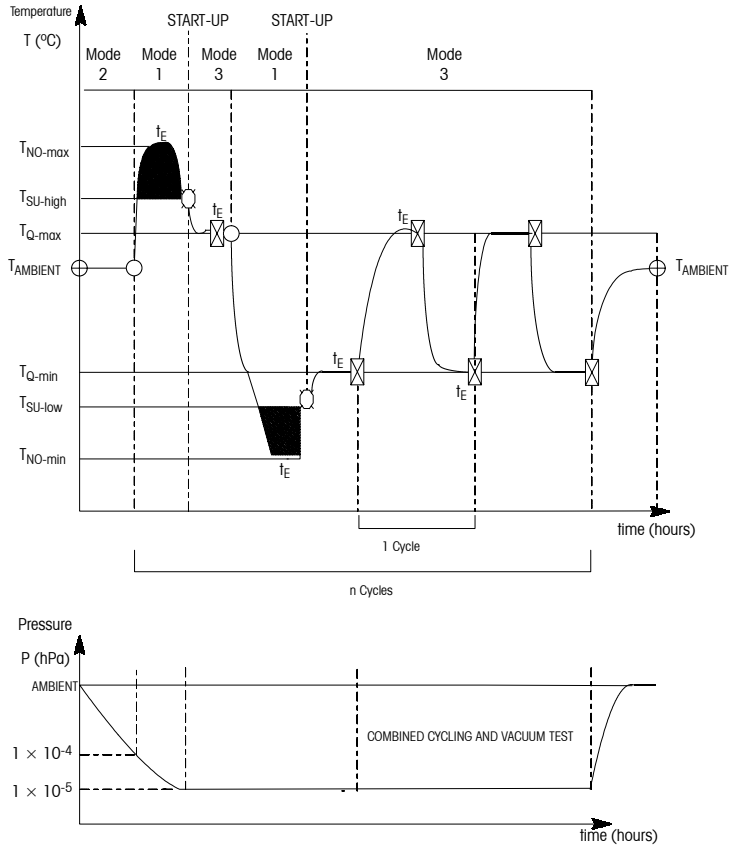

Figure 7.3 – *Thermal vacuum cycling test sequence [17]*

Figure 7.3 illustrates a typical thermal vacuum cycling test sequence. The test begins and ends with a functional test at ambient temperature. Then, at the pressure of of 10^{-4} hPa, the test always starts with a temperature increase up to the high non-operating level ($T_{NO,max}$) to accelerate outgassing (baking sequence). After a dwell time t_E, the temperature is decreased to the maximum start-up level ($T_{SU,high}$) and is then stabilized at the high operating temperature ($T_{Q,max}$). Once the temperature is stabilized (time t_E) the functional and performance tests (including TB) are performed and after that it is switched off again to decrease and maintained at the minimum non-operating temperature ($T_{NO,min}$) during a time t_E. The temperature is then increased to the minimum start-up temperature and the equipment is switched on. When stabilized at the low operating level (TQ_{min}), and after the time t_E, the functional tests in cold case are performed.

The spacecraft is then cycled between $T_{Q,max}$ and $T_{Q,min}$ until the number of cycles specified in Table 7.3 is achieved. Functionally tests are again performed during the last cycle at $T_{Q,max}$ and $T_{Q,min}$ after which the temperature is raised to ambient conditions and the final functional and performance test can be performed. All the symbols are summurized in Table 7.1

As defined above, the protoflight approach combines acceptance and qualification: levels are the qualification ones while duration are as acceptance ones [17]. Nevertheless 6 cycles could be performed.

Symbol	Description
T	Test item temperature
$T_{AMBIENT}$	Ambient temperature
T_{NO-max}	Maximum non-operating temperature (highest design temperature for the equipment to survive not powered)
T_{NO-min}	Minimum non-operating temperature (lowest design temperature for the equipment to survive not powered)
$T_{SU-high}$	Maximum start-up temperature (highest design temperature of the equipment, at which the equipment can be switched on)
T_{SU-low}	Minimum start-up temperature (lowest design temperature of the equipment, at which the equipment can be switched on)
T_{Q-max}	Maximum qualification temperature (highest design temperature at which the equipment demonstrates full design ability)
T_{Q-min}	Minimum qualification temperature (the lowest design temperature at which the equipment demonstrates full design ability)
P	Pressure
MODE 1	Functionally inert (test item not energized). Normally applicable to the non-operating condition.
MODE 2	Partially functioning. Conditions as detailed in applicable design specifications, but normally applicable to conditions during launch.
MODE 3	Fully functioning (test item fully energized and fully stimulated). Normally applicable to conditions during orbit.
⊕	Initial and final "functional and performance test"
⊠	Intermediate reduced functional and performance test
t_E	Dwell time
⦻	Switch-on (Start-up)
◯	Switch-off

Table 7.1 – *Legend and symbols for thermal vacuum (and cycling) test sequences (Fig. 7.3) [17]*

Parameter	**Condition / Value**
Start cycle	Hot
n (number of cycles)	8
t_E (dwell time at T_{hot}/T_{cold}) [a, b]	2 h
dT/dt (temperature rate of change)	< 20 °C/min
Stabilization criterion	1 °C/h
[a] $T_{hot} = T_{Q-max}$ or T_{NO-max}.	
[b] $T_{cold} = T_{Q-min}$ or T_{NO-min}.	

Table 7.2 – *Thermal cycling test parameters (qualification) (Fig. 7.3) [17]*

Levels		Duration	
Qualification margins	Acceptance margins	Qualification	Acceptance
10°C	5°C	8 cycles	4 cycles

Table 7.3 – *Qualification and acceptance test levels and durations according to ECSS-E-10-03A standard [17]*

All the previous curves and tables comes from standards considering conventional spacecraft. Regarding OUFTI-1, some modifications will be provided to meet the particular CubeSat thermal design.

OUFTI-1's TMM results and operating/non operating (NO) temperature ranges showed that the batteries were the more critical components. Their NO temperature range, identical to the discharge one is only -20°C to +60°C while their operating one is reduced to 0°C to +45°C. On another hand, all the other units (structural and electronic) have a wider operating (and non-operating because they are identical) range at least equal to the -40°C to +85°C industrial temperature range. The dissipation transistor whose temperature range is even wider: from -65 to +200°C (operating or non-operating).

	Predicted (op)		Qualification		Non-operating		Start-up	
	Min	Max	Min	Max	Min	Max	Min	Max
Batteries	5°C	35°C	0°C	45°C	-20°C	60°C	5°C	35 °C
Other	-30°C	35°C	-40°C	45°C	-45°C	85°C	-	-

Table 7.4 – *OUFTI-1's test temperatures definition*

Table 7.4 confirms that the batteries are well the more restrictive components. The predicted temperature of the structure ranges from -30°C to +35°C but measures have been taken to ensure that the temperature of the batteries does go beyond their limits. Thanks to the active and passive thermal control system, the batteries should now range between +5°C and +35°C. The non-operating lower temperature of the batteries (-20°C) is thus higher than the operating temperature of the CubeSat (-30°C): the temperature of the switched off CubeSat could only decrease to -20°C while if it is switched on, the heater are designed to maintain the batteries above 0°C when the temperature of the structure is -30°C. This is in contradiction with the above figure 7.3

Two solution are proposed to deal with this problem:

1. The first solution is therefore to keep the CubeSat switched on after the first functional test and decreasing the temperature down to the low qualification operating temperature $T_{Q,min}$ instead of the non-operating one. The CubeSat should also be operational (at least the heaters) during all the subsequent cycles. The number of cycles should thus take into account the level of charge of the batteries. A separate test should be performed on the batteries for their non-operating qualification.

2. The second solution consist in decreasing the temperature down to the non-operating one of the batteries during the first cycle with the CubeSat switched off. Then raise the temperature to the low start-up temperature $T_{SU,low}$ before switch on the CubeSat and decrease its temperature again to the operating one. Here again, the CubeSat should be kept switched on to allow the heating system to maintain the batteries above 5°C and the number of cycles should be defined by taking into account the level of discharge of the batteries resulting from the heaters consumption.

7.3 Test set-up

Thermal testing involves specific equipments such as vacuum chambers allowing active thermal control. Moreover, vibrations testing which are not discussed in the present thesis (but in the STRU subsystem [42]) are also required and usually performed before thermal testing. Both will be performed at the Centre Spatial de Liège (CSL) which is one of the four Coordinated European Environmental Test Facilities (CETeF) of the European Space Agency (ESA). CSL has six vacuum chambers called FOCAL (Facility of Optical Calibration at Liège) whose diameter range from 0.25 to 6.5m (with 1.5m, 2m, 3m and 5m). While the satellite Planck have been tested in FOCAL 5 during nearly two months, the foreseen vacuum chamber for OUFTI-1 thermal testing is FOCAL 1.5.

Nevertheless, many test parameters have still to be defined in addition to the different temperature ranges of the thermal vacuum cycling. The following questions need to be answered:

- How is fastened the CubeSat in the vacuum chamber?
- How to impose the temperature variation on the CubeSat?
- How the low pressure levels are achieved and is-it harmful to the CubeSat?
- Is solar simulation feasible?
- What are the functional test that will be performed and how to collect the data?
- Shall the batteries be charged during the tests?
- ...

While some of these questions will remain partially unanswered because the overall design is not yet defined, some answers can already be given.

As explained in test specification section, the required pressure level is 10^{-5} hPa. Actually, the pressure required depends on the size of the vacuum chamber: the bigger the chamber, the lower the required pressure. The key parameter is to ensure that the mean free path of remaining molecules in the chamber is greater than the chamber characteristic size (diameter). The pumping phase is divided in two stages: a first one performed through classical pump down to 10^{-2} mbar and the second using a turbomolecular pump to decrease the pressure down to 10^{-5} mbar. Development tests demonstrate that such pressure levels were harmful to the batteries that inflates under mechanical stresses.

The first two questions are not independent because the way a satellite or instrument has its temperature imposed influence the way it is fastened to the chamber and conversely. Each thermal tests set-up has its own dedicated set-up and heating/cooling method. There is no universal method. Nevertheless different heating and cooling methods are available each with its own advantages and drawbacks. They can be classified in two categories: radiative and conductive methods and are presented in Table 7.5

	Method	Advantages	Drawbacks
Radiative	Solar simulation	- Does not assume a prior known environment - Accurately simulates solar environment - Allow GMM error detection	- Solar simulation chamber not available at CSL - Cannot simulate non-solar heat loads - Parallel illumination required large set-up
	Heating lamps	- lamps can be placed efficiently and are independent, providing good flexibility	- many lamps required and interfering with each other
	Heater plates	- environment accurately known and allow independent surface control	- requires knowledge of absorbed fluxes and cooling in heater plates
Conductive	heater	- good for appendages such as antennas, booms etc.	- requires knowledge of absorbed fluxes and test blanket are required of heaters are mounted to them
	heater plates	- direct and independent surface control	- limited flexibility

Table 7.5 – *Thermal testing heating/cooling methods [24]*

Solar simulation would have been appropriate to simulate the real thermal loads on the CubeSat and would have allowed the use of the solar cells. However solar simulation is difficult to implement because the heat generated by the halogen is difficult to cope with unless the lamps are relatively far from the other cooler environment elements. It is not available for the moment at CSL.

However, because of its cubic shape, it seems convenient to use of heater plates, one for each face of the CubeSat. Moreover, the continuous rotation of the CubeSat involves relative uniform external temperatures of the sides and we can assume that all the faces have the same temperature. All the heater plates surrounding the CubeSat can then be controlled by a unique fluid loop. The fluid loop consist of a nitrogen thermally controlled inlet line that impose the temperature of the plates. The heater plates assembly is covered with MLI to reduce exchanges and losses with the walls of the chamber remaining at ambient temperature. The plates and MLI constitute the so-called thermal shroud. Figure 7.4 shows the shroud used for Planck testing in FOCAL 5. The internal sides of the shroud are panted in black (here it is black opened honeycomb) to enhance exchanges between the satellite and the shroud. Sometimes, thermal straps between the satellite and the shroud are used to enhance heat exchange and increase the heating or cooling phase. However, seeing the relative low thermal inertia of the CubeSat, such measure should not be necessary.

The CubeSat has five of its six faces covered with solar cells. Conse-

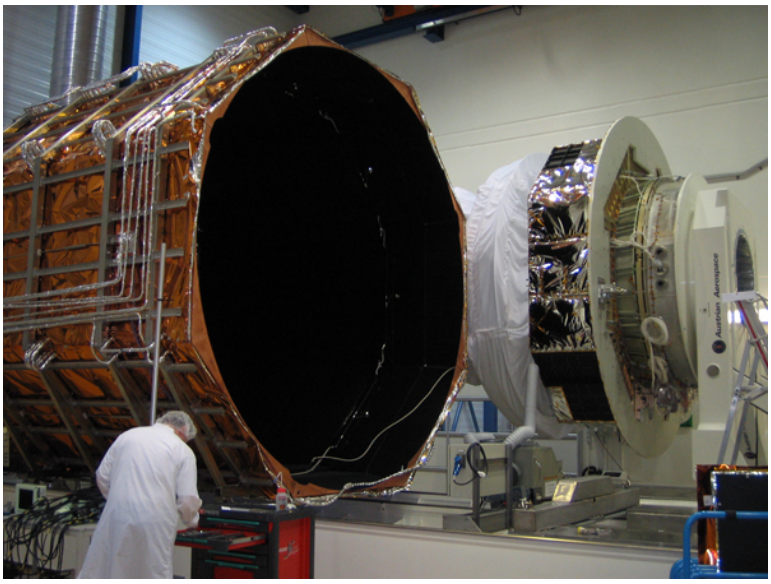

Figure 7.4 – *Example of thermal shroud used for the testing of Planck in FOCAL 5*

quently, the only remaining face available to fasten the CubeSat in the chamber is the antennas' face. Again, the mounting interface should be insulating from the chamber walls ambient temperature. Figure 7.5 illustrates the foreseen set-up with fluid loop controlling the shroud.

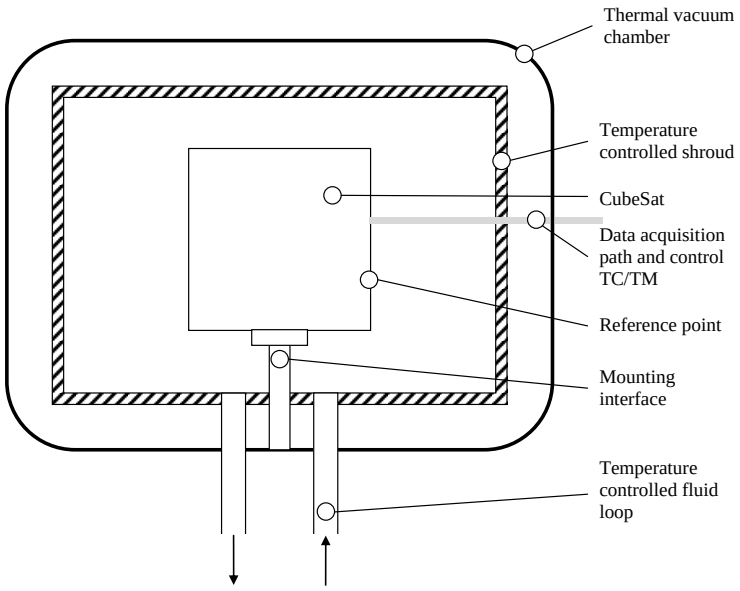

Figure 7.5 – *Thermal vacuum cycling test set-up*

Figure 7.5 also shows that a way to communicate with the CubeSat and collect data must be provided. At any time, all the parameters must be available to allow a comprehensive understanding, monitoring and con-

trol of the CubeSat behavior. The thermal cycling curves presented above require to define a reference point temperature that is representative of the mean temperature level of the equipment. A temperature sensor shall be located at the reference point. During the test, the shroud temperature are controlled by the operator in such a way that the reference point temperature follows the thermal cycling specification curve. In the present case, two reference points are defined and located as follows:

1. on the structure. This reference point shall be representative of the global temperature of the CubeSat. The sensor must obviously not be located on solar cells nor anodized rails. Therefore, the more convenient place is again the antennas' face (face 4). However, it shall be placed far enough from the mounting interface.

2. the second reference point is the batteries. As the batteries will already be equipped with temperature sensors, these sensors will be used as reference point to monitor the batteries temperature. In any case the temperature of the batteries would go beyond their limits, proper measures shall be taken to bring it back within its safe range.

Concerning the performance and functional tests that are performed during the first (TB) and last cycles, they are difficult to be clearly defined at this development phase. However, we can already assume that the following tests should probably be conducted:

- Each defined mode should be tested. Among these, full D-STAR transmitting and receiving. As the CubeSat is inside the vacuum chamber, communication through the antennas are useless and suitable testing procedures shall therefore be defined without the use of the antennas. Moreover, the thermal vacuum cycling test will be performed in stowed configuration. Nevertheless, during transmission, the amplifier shall be used normally and its temperature shall be carefully monitored especially during the hot case.

- Extensive beacon functional and performance tests shall be conducted in hot and cold cases.

- The dissipation system shall be switched on with full power. If necessary, additional power is provided through the USB interface to meet the predicted dissipated power with 10% margins [**?**]. The dissipation transistor and batteries temperatures shall carefully be monitored.

- In the cold case, the heating system of the batteries shall demonstrate that the design implementation fully meets the requirements.

- All the housekeeping parameters shall be monitored and saved, especially the temperatures to allow the correlation of the Thermal Model.

As a comprehensive test is not possible, separate tests should be conducted, under ambient pressure:

- Simulations have shown that the antennas could undergo relatively high temperatures (up to more than 200°C at their free extremity). For this reasons, specific functional tests should be conducted in the deployed configuration with dedicated thin heaters located on the antennas' free extremity. Heaters should be designed to cope with the convective losses.

7.4 Summary

Thermal testing is a compulsory step in the development of a satellite. Concerning OUFTI-1, the tests shall be conducted at the Centre Spatial de Liège. As the CubeSat development is not terminated, a detailed test description was tot possible. However, foreseen set-up and functional tests have been described. Once the CubeSat will be fully designed, a test procedure document shall be written in agreement with the Centre Spatial de Liège and all the subsystems to carefully define the functional tests that should be performed on the CubeSat.

Conclusions

Throughout this work, different thermal models with different purposes and complexity have been carried out. The first models brought to light that issues would occur in both cold and hot cases. Nevertheless, only the Detailed Thermal Model enabled a comprehensive investigation of these issues. As the thermo-optical properties of the structure and thermal properties of the batteries were subjected to some relatively high uncertainties, measurements have also been conducted through which the heat capacity and transverse conductivity of a typical LiPo battery were determined, as well as the emissivities of the two coating of the aluminum frame. Moreover, contact phenomenon in the structure have been confirmed through IR imaging. Those results were therefore included in the DTM.

It has been presented that both hot and cold cases had a strong impact on the design of the CubeSat.

In the cold case, simulations showed that the batteries would undergo too low temperatures and that they were out of their temperature ranges when coming out of the eclipse. A heating system has therefore been designed: two 250 mW Minco heaters, set in parallel combined with three temperature sensors (to avoid the problem encountered by Compass-1), will ensure that the temperature of the batteries will remain within its allowable range. The heaters will be switched on when the temperature reached 5°C. To reduce losses and increase its efficiency, the DTM showed that insulating the batteries is required. Covering the batteries with a low emissive tape such as aluminum thermal tape is planned and Nylon washers combined to titanium spacers shall be used to fasten batteries' PCB. Even in the worst case, we verified that the consumption of the heating system remains acceptable compared to the capacity of the batteries: up to 150 mAh compared to the 1000 mAh typical capacity of one LiPo battery (and therefore 2000 mAh for both batteries). However, as the battery model is not yet fully defined, the heaters have not yet been ordered, depending on the dimensions of the batteries. On another hand, we contact the company Moss Plastic Parts to order some sample nylon washers because creep phenomenon should be carefully studied to ensure structural integrity of the batteries' PCB fastening.

Concerning the hot case, the dissipation system developed by EPS subsystem was the cause of nearly all issues: involving too high temperatures on the batteries and the dissipation transistor. To solve these problems, drastic measures had to be taken in order to reduce temperatures: we showed that a thermal strap encircling the dissipation transistor would be required and fastened to antennas' deployment mechanism panel, involving a 10°C temperature decrease of the batteries (from 48°C to 38°C) and 20°C of the transistor (from 115°C to 95°C) . In addition to that, relocating

a part of the dissipated power through two Minco resistances (reference XHK5377R26.3L12B) in parallel also fastened to the antennas' panel involves another 3°C and 30°C temperature decrease of the batteries and transistor, respectively reduced to 35°C and 67°C. Finally, for reliability purposes, batteries' PCB should be fastened to EPS2 PCB instead of EPS one because it contains less dissipative components and is therefore cooler. The Minco resistances have been ordered to evaluate the feasibility of their integration on antennas' panel, which has been confirmed.

The third issues occurring in the hot case involves the COM amplifier, because of its quite low efficiency and therefore high heat dissipation. No concrete measures have been taken to solve this problem because too many uncertainties still surround its definition. However, we stated that the amplifier should be localized either close to one corner of the COM PCB or it the center of the PCB. locating the amplifier on one edge should be avoided. Furthermore, its efficiency should be taken into account when selecting the amplifier. For instance, using the ADL5541 could reduce the temperature from 70 °C to 45°C because the ADL5541 only dissipates 0.5 W instead of 1.75 W assumed for classical amplifiers.

On the educational point of view, working on this project has been very enriching and its primary goal has been achieved: through it, we gained an invaluable hands-on experience in satellite design, especially in thermal design. Working within a CubeSat project has numerous advantages. Among them, in our opinion, working within a team is the main one and has been extremely constructive, it allows a global view of the project and highlights the strong interaction that may occur between the different subsystems.

Moreover, this project allowed us to present the project in different international events and workshops during which we met other CubeSat teams and exchanged ideas. Namely, we participated to the Second European CubeSat Workshop at ESTEC, we presented the project on the Space Days event in Liège and at the Redu Eurospace Center.

CubeSat project also allows to work within an industrial framework and to collaborate with famous companies or agencies such as the European Space Agency (ESA), EADS Astrium, Thales Alenia Space, Azur Space and many others.

Concerning the future developments, numerous tests should be conducted to correlate the model and because this is the only way to ensure that the design meets the specification requirements. Particularly, the heating system should be extensively tested. Tests should also be conducted on the heat rejection design to verify that the strap and relocated resistances play their role. The effect of hot antennas should be investigated to see the effect on their radiation pattern because the vacuum tests that will be performed et the Centre Spatial de Liège will probably be in the stowed configuration.

At last, according to Prof. Bob Twiggs, the CubeSat leitmotiv should be:

Test, test and test again !

Appendix

A Acronyms

ADCS	Attitude Determination and Control System
A&M	Department of Aerospace and Mechanical Engineering
BOL	Beginning Of Life
COTS	Commercial-Off-The-Shelf
CSL	Centre Spatial de Liège
D-STAR	Digital Smart Technologies for Amateur Radio
DTM	Detailed Thermal Model
EOL	End Of Life
EECS	Department of Electrical Engineering and Computer Science
EPS	Electrical Power Supply
ESA	European Space Agency
ESATAN	European Space Agency Thermal Analysis Network
ESTEC	European Space Technology Research Center
FE	Finite Element
FEM	Finite Element Model
FHTS	Fluid Heat Transport System
FOCAL	Facility for Optical Calibration at Liege
GMM	Geometric Mathematical Model
GND	Ground
IC	Integrated Circuit
MCRT	Monte Carlo ray-tracing
MLI	Multi-layer Insulation
OBC	On-Board Computer
OUFTI	Orbiting Utility For Telecommunication Innovation
P-POD	Poly-Picosatellite Orbital Deployer
PCB	Printed Circuit Board
REF	Radiative Exchange Factor
SSETI	Student Space Exploration and Technology Initiative
STM	Simplified Thermal Model
STRU	Structure & Configuration
TCS	Thermal Control System
TMM	Thermal Mathematical Model
ULg	University of Liège

OBC PCB	main on-board computer printed circuit board
OBC2 PCB	secondary on-board computer printed circuit board
EPS PCB	main electrical power supply printed circuit board
BAT PCB	secondary printed circuit board on which the batteries are attached
EPS2 PCB	innovative electrical power supply printed circuit board
COM PCB	communication subsytem on-board computer printed circuit board

B Aluminium frame faces links

This appendix explains how the links between the different nodes of the frame have been computed. The method is the same as the one used for the computation of the global links in the high level model : by imposing the temperature gradient across the desired geometry, a SamcefField finite element analyses gives the resulting flux from which the thermal conductance can be deduced. The thermal resistance/conductance does only depends on the geometry and conductivity of the frame links.

Face 3

Figure 6 describes the resistances network (in red) representing the heat flow path between the nodes of the face. For symmetry reasons, there are only two different resistances, R_1 along the diagonal and R_2 along the horizontal/vertical.

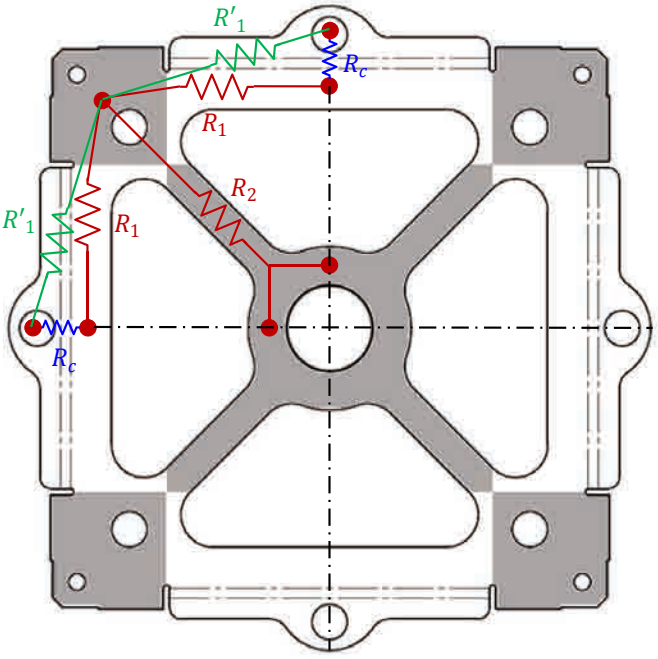

Figure 6 – *Conductance model of face 3*

R_1 and R_2 are easily determined: the first one is obtained by considering a quarter of the face and setting the boundary conditions on both extremities. By this way, the diagonal does not get involved in the conduction path (figure 7, left) and R_1 is equal to one half of the difference of temperatures divided by the resulting flux:

$$R_1 = \frac{1}{GL} = \frac{\Delta T}{2Q_{tot}} = \frac{0.5}{0.04094} = 12.21\ [K/W]$$

Then, R_2 is obtained by involving the diagonal in the flow path and setting one of the two temperature at its extremity (figure 7, right). The equivalent resistance is therefore equal to:

$$R_{eq} = R_1 + R_1//R_2 = R_1 + \frac{R_1 R_2}{R_1 + R_2} \qquad R_2 = \frac{R_1(R_1 - R_{eq})}{R_{eq} - 2R_1}$$

One finally gets: $R_2 = 33.29\ [K/W]$ with $R_{eq} = 21.14\ [K/W]$

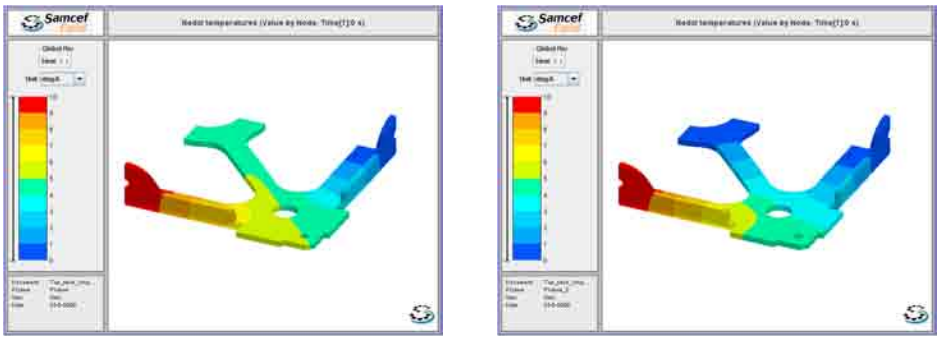

Figure 7 – *Face 3 conduction SamcefField results*

The previous model assumed perfect contact on all the bracket surface but experiments of chapter 6 showed the presence of contact phenomenon. Hence, the heat flow passing from face 3 to face 1,2,5 or 4 shrinks around the contact area, close to the screw. To take into account constriction effect around the screw hole, an additional resistance R_c (in blue) is considered between the nearby node and the screw hole. To determine this constriction resistance, the boundary conditions were set around the screw holes. The computed flux correspond to the green resistances R_1 of figure 6. R_c can then be approximated by differentiating R_1 and R_1. This leads to $R_C = R_1 - R_1 = 15.02 - 12.21 = 2.81\ [K/W]$.

Finally, after some simplifications, the total transverse resistance, from one side to the opposite one is equal to:

$$R_{tot} = R_c + R_1 + R_1//R_2 = 2.81 + 21.14 = 23.95\ [K/W]$$

while the finite elements global resistance, between to opposite screw holes, is 23.76 $[K/W]$

Faces 1, 2 and 5

Face 1, 2 and 5 are identical and but no longer symmetrical. This means that instead of two different resistances, there are three ones: R_1, R_2 and R_3 as shown on figure 8.

Using the superposition principle, one can perform three FE simulations to obtain a set of three equations for the three unknowns: one for $R_1 + R_2$, the second for $R_1 + R_3$ and the third one for $R_2 + R_3$. One finally gets $R_1 = 24.55\ [K/W]$, $R_2 = 24.62\ [K/W]$ and $R_3 = 37.04\ [K/W]$.

Face 6

Face 6 conductances are identical to face 3 except for the link with the additional node 3610, representing the bracket fastened to face 4.

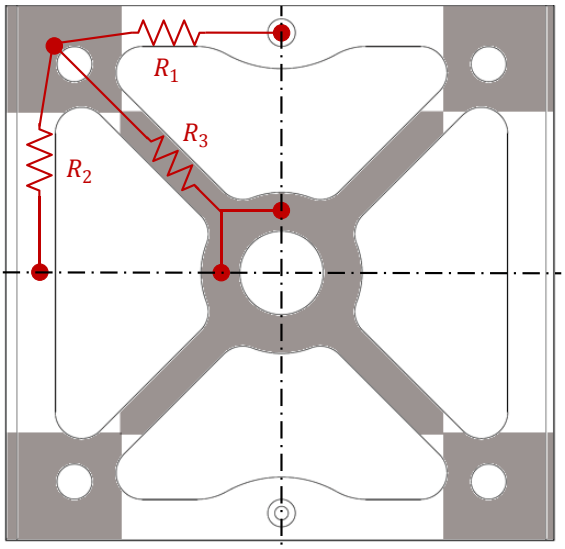

Figure 8 – *Conductance model of faces 1, 2 and 5*

Face 4

Face 4 links have all been determined by the same way, through FE models.

All the conductance are summarized in Table 6.

nodes	GL	nodes	GL	nodes	GL	nodes	GL
Face 1, 2 & 5 - 3100, 3200 & 3500 series							
1-2	4.07	3-2	4.07	5-4	4.06	7-6	4.07
1-9	2.69	3-9	2.69	5-9	2.69	7-9	2.69
1-8	4.06	3-4	4.06	5-6	4.07	7-8	4.06
Face 3 - 3300 series							
1-2	8.19	3-2	8.19	5-4	8.19	7-6	8.19
1-9	3.00	3-9	3.00	5-9	3.00	7-9	3.00
1-8	8.19	3-4	8.19	5-6	8.19	7-8	8.19
Face 4 - 3400 series							
1-2	5.50	3-2	10.8	5-4	4.06	7-6	8.19
1-9	3.17	3-9	5.56	5-9	2.69	7-9	3.00
1-8	64.9	3-4	3.85	5-6	4.07	7-8	8.19
Face 6 - 3600 series							
1-2	8.19	3-2	8.19	5-4	8.19	7-6	8.19
1-9	3.00	3-9	3.00	5-9	3.00	7-9	3.00
1-8	8.19	3-4	8.19	5-6	8.19	7-8	8.19
2-10	62.7						

Table 6 – *Aluminium frame faces conductances, in* $[W/K] \times 10^{-2}$

C Analytical computation of VF between parallel rectangles

Here is the formula used for the view factor computation in the verification process of DTM's Geometrical Mathematical Model. The view factors between each elements of the two opposite PCBs were indeed required in the Gebhart's formula. Figure **??** illustrates the different notation used.

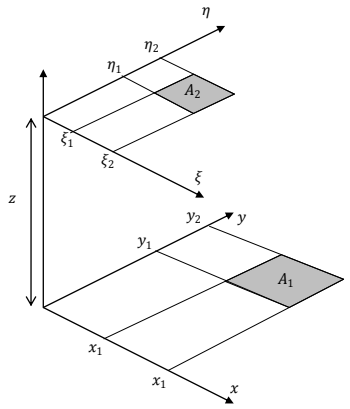

Figure 9 – *View factor between two parallel rectangles [15]*

$$F = \frac{1}{(x_2 - x_1)(y_2 - y_1)} \sum_{i=1}^{2} \sum_{j=1}^{2} \sum_{k=1}^{2} \sum_{l=1}^{2} (-1)^{i+j+k+l} G(x_i, y_j, \eta_k, \xi_l, z)$$

where the function

$$G(x, y, \eta, \xi, z) = \frac{a + b - c}{2\pi}$$

with

$$a = (y - \eta)\sqrt{(x - \xi)^2 + z^2} \arctan\left(\frac{y - \eta}{\sqrt{(x - \xi)^2 + z^2}}\right)$$

$$b = (x - \xi)\sqrt{(y - \eta)^2 + z^2} \arctan\left(\frac{x - \xi}{\sqrt{(y - \eta)^2 + z^2}}\right)$$

$$c = \frac{z^2}{2} \log\left((x - \xi)^2 + (y - \eta)^2 + z^2\right)$$

The view factors with the lateral aluminum panels representing the lateral frame were indirectly deduced from the reciprocity properties of the view factors ($A_i\, F_{ij} = A_j\, F_{ji}$) and from the energy conservation ($\sum F_{ij} = 1$ for a closed system) that is enforced by setting the aluminum panels such as they form a closed environment with the PCBs.

D Advanced Simulink Thermal Model

Here are the advanced Simulink model diagrams. First, the global one: on the left is the heat fluxes computation module already presented and on the left the thermal lumped parameter model which is described in the second diagram. Within this, the PCB stack block is detailed in the third and last module. The results obtained with this model are relatively well correlated with ESATAN/ESARAD ones.

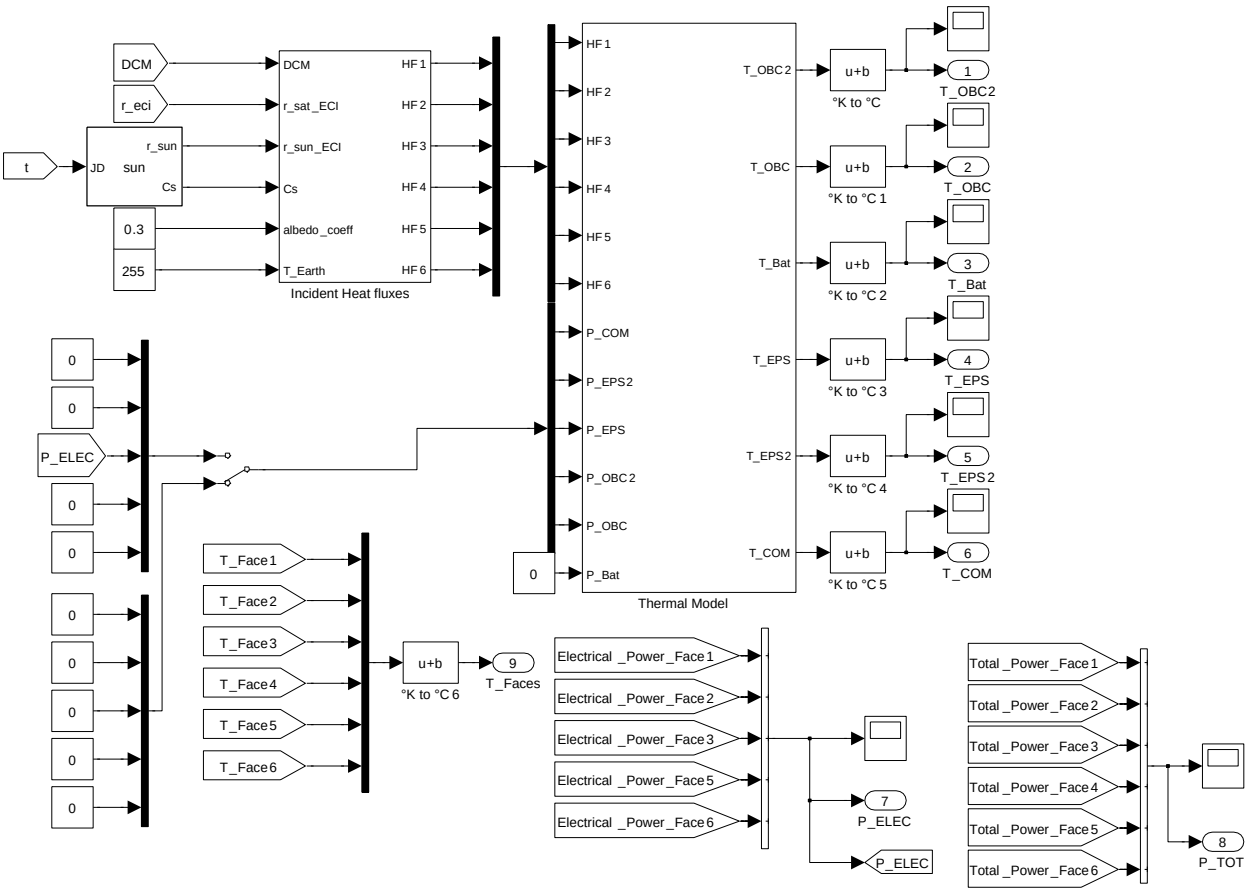

Figure 10 – *Advanced Simulink thermal model main high level diagram*

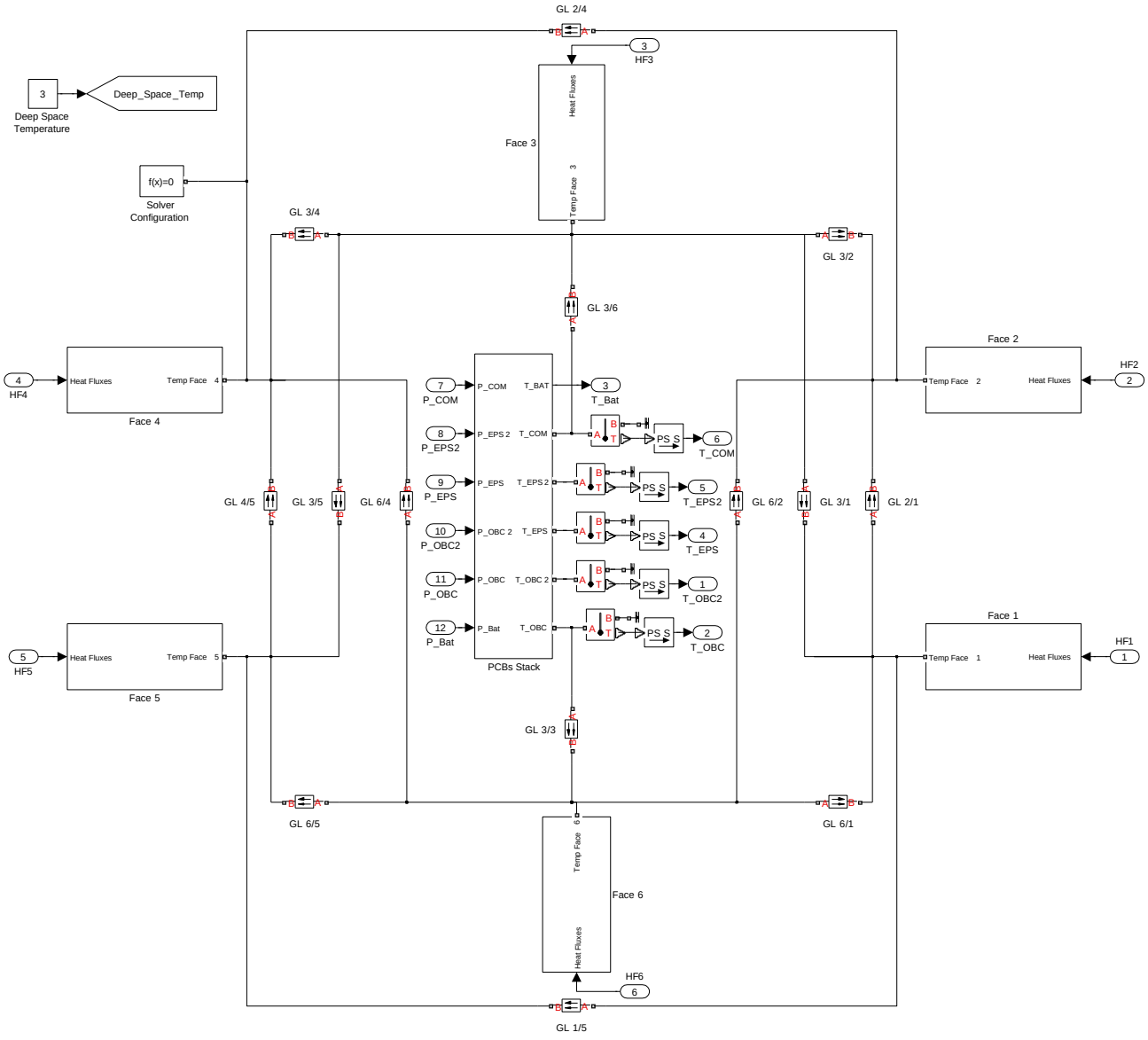

Figure 11 – *Advanced Simulink thermal model low level diagram: global model*

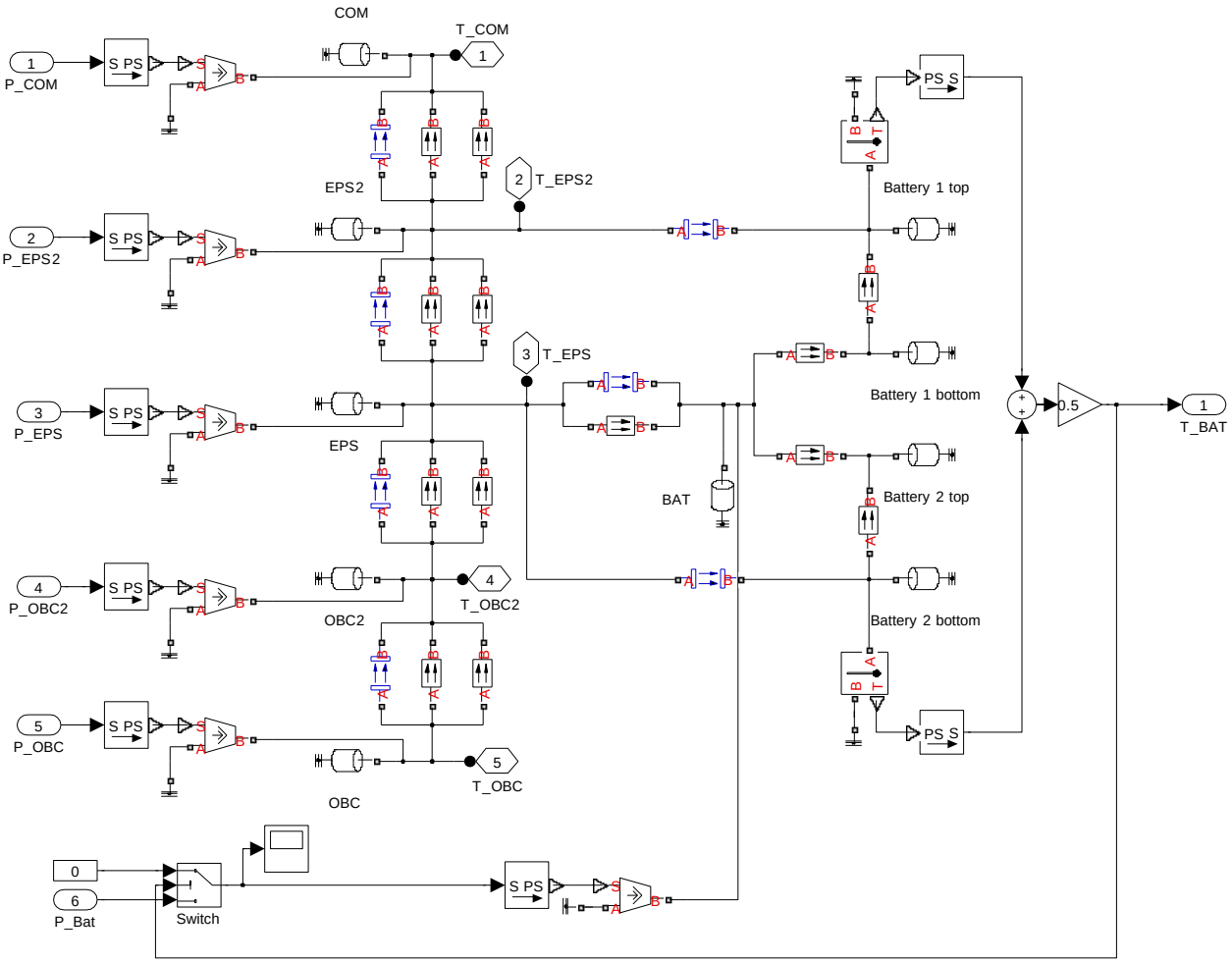

Figure 12 – *Advanced Simulink thermal model low level diagram: PCB stack model*

E 2D CONDUCTION LUMPED PARAMETER METHOD

The lumped parameter method allows to transform differential equations into algebraic equation. Concerning thermal conduction, the algebraic equation are moreover linear (if materials properties do not depend on temperature) and can therefore be written under a matrix form. Here, the case a 2D plate will be considered but the method can easily be generalized to 3D problems.

The lumped parameter method relies on a discretization of the domain into smaller isothermal elements called nodes. For rectangular elements, Figure 13 illustrates the incoming fluxes exchanged between adjacent nodes and energy conservation leads to:

$$Q_{1,n} + Q_{2,n} + Q_{3,n} + Q_{4,n} + Q_n = \rho c T_n$$

In case of steady state, $T_n = 0$ and using electrical analogy, one has:

$$GL_x\ (T_1 - T_n) + GL_x\ (T_3 - T_n) + GL_y\ (T_2 - T_n) + GL_y\ (T_4 - T_n) = -Q_n$$

where $GL_x = \frac{k t \Delta_y}{\Delta_x}$ and $GL_y \frac{k t \Delta_x}{\Delta_y}$ are respectively the thermal conductances along x and y directions with k the thermal conductivity and t the thickness of the plate.

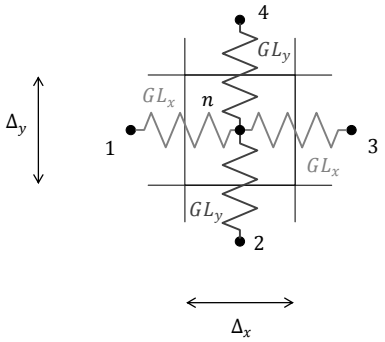

Figure 13 – *Equivalent conductivity of BAT PCB fastening in function of the PA washer thickness and thermal conductivity of the spacer*

Generalizing for n nodes the equations can be set under the following matrix form

$$\underline{\underline{A}}\ \underline{T} = \underline{g}$$

where $\underline{\underline{A}}$ is a $n \times n$ matrix, $A(i,j)$ representing the conductive coupling between nodes i and j and $g(i)$ the external loads of node i.

If there are B temperature boundary conditions and therefore $I = n - B$ unknowns, the system can be divided as follows:

$$\underline{T} = \begin{bmatrix} T_1 \\ \vdots \\ T_I \\ T_{I+1} \\ \vdots \\ T_n \end{bmatrix} = \begin{bmatrix} \underline{T}_I \\ \underline{T}_B \end{bmatrix}$$

Splitting matrix $\underline{\underline{A}}$ and vector $\underline{g}$ in the same way, this gives:

$$\begin{bmatrix} \underline{\underline{A}}_{II} & \underline{\underline{A}}_{IB} \\ \underline{\underline{A}}_{BI} & \underline{\underline{A}}_{BB} \end{bmatrix} \begin{bmatrix} \underline{T}_I \\ \underline{T}_B \end{bmatrix} = \begin{bmatrix} \underline{g}_I \\ \underline{g}_B \end{bmatrix}$$

and the unknowns temperature $\underline{T}_I$ are deduced without inversing the entire $\underline{\underline{A}}$ matrix:

$$\underline{T}_I = \underline{\underline{A}}_{II}^{-1} \left(\underline{g}_I - \underline{\underline{A}}_{IB} \underline{T}_B \right)$$

The method has been correlated with SamcefField has shown in Figure 14.

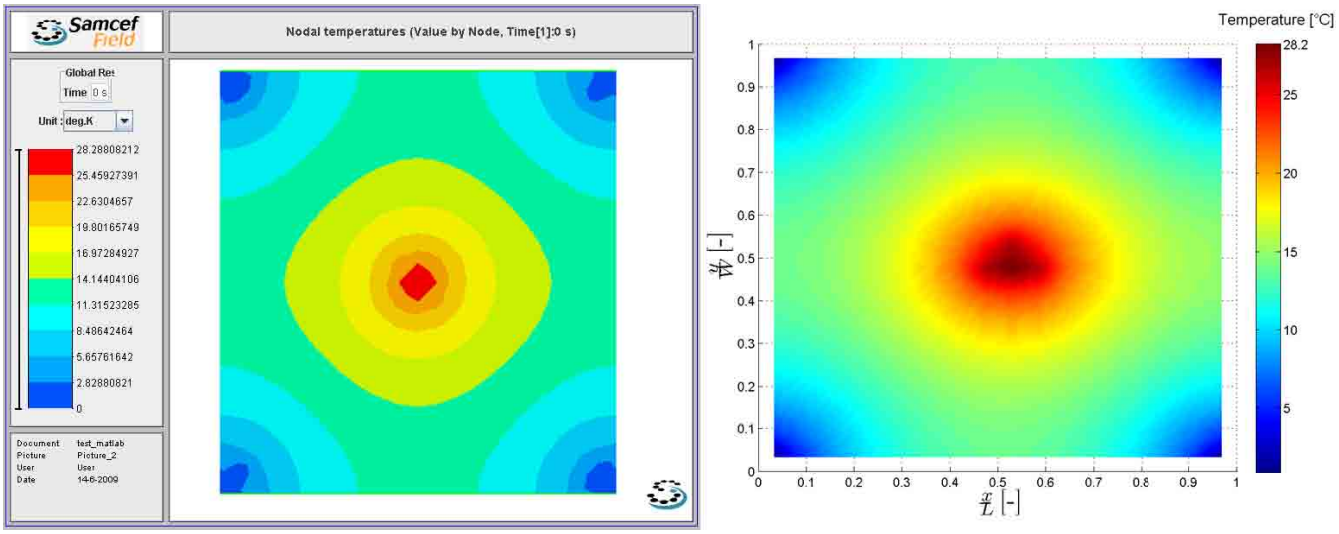

Figure 14 – *Equivalent conductivity of BAT PCB fastening in function of the PA washer thickness and thermal conductivity of the spacer*

Bibliography

[1] I. Alet, *Contrôle thermique des engins spatiaux*. École nationale Supérieure de l'Aéronautique de l'Espace, 1998. (Quoted page 23.)

[2] *ESARAD™ User Manual - UM-ESARAD-024*, Alstom Aerospace, Cambridge Road, Whetstone, Leicester LE8 6LH United Kingdom, oct 2007. (Quoted pages ix et 43.)

[3] *ESATAN™ User Manual - UM-ESATAN-004*, Alstom Aerospace, Cambridge Road, Whetstone, Leicester LE8 6LH United Kingdom, oct 2007.

[4] Analog Devices, Inc., "50 mhz to 6 ghz rf/if gain block, adl 5541," 2007, revision 0. (Quoted pages 86 et 99.)

[5] ——, "High performance narrow-band transceiver ic data sheet, adf 7021," 2007, revision A. (Quoted page 21.)

[6] *Vega User's Manual, Issue 3, revision 0*, http://www.arianespace.com, Arianespace, Boulevard de l'Europe, B.P. 177, 91006 Evry-Courcouronnes cedex, France, mar 2006.

[7] Azur Space Solar Power, "Azur space solar power gmbh," http://www.azurspace.com. (Quoted pages xii, 5, 42, 47 et 75.)

[8] H. W. Babel, C. Jones, and K. David, "Design properties for state-of-the-art thermal control materials for manned space vehicles in Leo," *Acta Astronautica*, vol. 39, pp. 369–379, Sept. 1996. (Quoted page 42.)

[9] V. Beukelaers, "From mission analysis to space flight simulation of the OUFTI-1 nanosatellite," Master's thesis, University of Liège, Belgium, 2009. (Quoted pages viii, 9, 23 et 76.)

[10] L. Chiarello, "Design and implementation of the control and monitoring system for the ground station of nanosatellite OUFTI-1 of University of Liège," Master's thesis, University of Liège, Belgium, 2009. (Quoted page 8.)

[11] J. H. Chou, "Design of Thermal Control Sub-System (TCS), Picosat course," May 2007. (Quoted page 42.)

[12] "Compass-1 Phase B documentation," http://www.raumfahrt.fh-aachen.de/, Jun 2004. (Quoted page 18.)

[13] "Delfi-C3's website," http://www.delfic3.nl/. (Quoted page 19.)

[14] DuPont™, "Summary of Properties for Kapton® Polyimide Films," www2.dupont.com/Kapton/en_US/assets/downloads/pdf/summaryofprop.pdf. (Quoted pages xii et 47.)

[15] J. R. Ehlert and T. Smith, "View Factors for Perpendicular and Parallel, Rectangular Plates," *Journal of Thermophysics and Heat Transfer 1993*, vol. 7, pp. 173–174, 1993. (Quoted pages xi et 120.)

[16] ESA-ESTEC, "Spacecraft thermal control design data, PSS-03-108," 1989.

[17] "ECSS-E-10-03A - space engineering : Testing," ESA Publications Division ESTEC, Feb 2002. (Quoted pages x, xii, 104, 105 et 106.)

[18] "ECSS-Q-70-71A - space product assurance : Data for selection of space materials and processes, rev.1," ESA Publications Division ESTEC, Jun 2004. (Quoted pages xii, 47 et 48.)

[19] N. Evrard, "Développement de l'infrastructure de mesure du nanosatellite OUFTI-1," Master's thesis, Gramme Institute, Belgium, 2009. (Quoted pages viii et 10.)

[20] H. Flemming, "DTU Satellite Systems and Design Course, Cubesat Thermal Design," http://www.dsri.dk/roemer/pub/cubesat, Sep 2001. (Quoted page 42.)

[21] *ThermaCAM™ Researcher User's manual*, FLIR Systems, Dec 2006. (Quoted pages ix, 42, 61 et 63.)

[22] P. Fortescue, J. Stark, and G. Swinerd, *Spacecraft Systems Engineering*, 3rd ed. Wiley, March 2003.

[23] S. Galli, "Mission design for the cubesat oufti-1," Master's thesis, University of Liège, 2008.

[24] D. Gilmore, *Spacecraft Thermal Control Handbook: Fundamental Technologies*, 2nd ed. Aerospace Press, December 2002. (Quoted pages viii, ix, x, xii, 16, 23, 25, 42, 70, 71, 104 et 109.)

[25] S. Hannay, "Modeling of the Attitude Determination and Control System of the nanosatellite OUFTI-1'," Master's thesis, University of Liège, Belgium, 2009. (Quoted pages viii, 7, 32 et 52.)

[26] J. Hardy, "Implémentation du protocole AX.25 à bord du nanosatellite OUFTI-1," Master's thesis, Gramme Institute, Belgium, 2009. (Quoted page 10.)

[27] P. G. Harkness, "An aerostable drag-sail device for the deorbit and disposal of sub-tonne, low Earth orbit spacecraft," Ph.D. dissertation, Cranfield University, School of Engineering, 2006. (Quoted page 42.)

[28] R. Henrard, "Mission Design for the CubeSat OUFTI-1," Master's thesis, University of Liège, Belgium, 2009. (Quoted pages viii, 8 et 76.)

[29] L. Jacques, "Rapport de stage : Etude thermique d'un capteur cylindro-parabolique," University of Liège - Centre Spatial de Liège, Belgium, Tech. Rep., nov 2008.

[30] L. Jacques and G. Pierlot, "Spécifications mécaniques des cartes pc104 destinées au projet oufti-1," Department of Aerospace and Mechanical Engineering, University of Liège, Liège, Belgium, Tech. Rep., mar 2009.

[31] Kokam Co., Ltd., "Superior Lithium Polymer Battery, specification for SLPB554374H," Mar 2007. (Quoted page 21.)

[32] ——, "Superior Lithium Polymer Battery, specification for SLPB723870H4," Apr 2007. (Quoted pages x et 87.)

[33] P. Ledent, "Design and Implementation of On-board Digitaly Controled Electrical Power Supply of Student Nanosatellite OUFTI-1 of University of Liege," Master's thesis, University of Liège, Belgium, 2009. (Quoted pages 8, 50, 77 et 87.)

[34] ——, "Test report - Vacuum tests for Varta and Kokam batteries," University of Liège, Belgium, Tech. Rep., May 2009. (Quoted pages x, 92 et 93.)

[35] Y. Madhour, "Phase C - SwissCube thermal Analysis," http://swisscube.epfl.ch/, EPFL - LTCM, Lausanne, Switzerland, Tech. Rep., Jun 2008. (Quoted page 49.)

[36] F. Mahy, "Design and Implementation of On-board Telecommunication System of Student Nanosatellite OUFTI-1 of University of Liège," Master's thesis, University of Liège, Belgium, 2009. (Quoted pages viii, 8 et 76.)

[37] Microchip Technology, Inc., "Pic18f2331/2431/4331/4431 data sheet," 2003. (Quoted page 21.)

[38] "Military specification - MIL-A-8625F Anodic Coatings, for Aluminum and Aluminum Alloys, with Amendment 1," http://www.wbdg.org/ccb/FEDMIL/a8625.pdf, Sep 2003. (Quoted page 60.)

[39] "Military specification - MIL-DTL-5541F Chemical Conversion coatings on Aluminum and Aluminum alloys," http://www.wbdg.org/ccb/FEDMIL/dtl5541f.pdf, Nov 1990. (Quoted page 60.)

[40] Minco, "Flexible Heaters Design Guide," www.minco.com. (Quoted pages 93 et 94.)

[41] PC/104 Embedded Consortium, "PC/104-*Plus* Specification, version 2.3," www.pc104.org, University of Liège, Belgium, Tech. Rep., Oct 2008. (Quoted page 48.)

[42] G. Pierlot, "OUFTI-1 : Flight system configuration and structural analysis," Master's thesis, University of Liège, Belgium, 2009. (Quoted pages viii, 10 et 108.)

[43] P. Poinas, "Rosetta - Experiment Thermal Interface Mathematical Models," ESA - ESTEC - TOS-MCT, Tech. Rep., Jun 1999, issue 2, reference : RO-EST-TN-3021. (Quoted page 42.)

[44] ——, "Satellite Thermal Control Engineering, prepared for "SME" 2004," Jun 2004. (Quoted page 16.)

[45] P. Prat, "GLAST Large Area Telescope Calorimeter Subsystem Thermal Design and Analysis," Laboratoire Leprince-Ringuet, Ecole polytechnique, Tech. Rep., Mar 2003. (Quoted page 42.)

[46] F. Primore, "Online calculator for the thermal properties in the plate direction for multi-layer glass-epoxy PCBs," http://www.frigprim.com/online/cond_pcb.html. (Quoted page 47.)

[47] Pumpkin, Inc., "CubeSat Kit User Manual," http://www.cubesatkit.com, 2005. (Quoted pages 6 et 21.)

[48] ——, "CubeSat Kit™ FM430 Flight Module Datasheet," Jun 2008, revision J. (Quoted page 21.)

[49] A. Rajendra, "Pressure Sensor Development Using Hard Anodized Aluminum Diaphragm and Thin Film Strain Gauges," Master's thesis, Indian Institute of Science, Department of Instrumentation, Bangalore, Apr 2006. (Quoted page 42.)

[50] P. Rochus, "Conception d'expériences spatiales," 2008. (Quoted pages 16, 42 et 70.)

[51] Semelab, "2N5151 High Speed Medium Voltage Switches Datasheet," mar 1997. (Quoted page 69.)

[52] *Sheldahl Red Book - Aerospace Thermal Control Materials*, http://www.sheldahl.com, Sheldahl, 1150 Sheldahl Road, Northfield, MN 55057, oct 2007. (Quoted pages 63 et 88.)

[53] "SwissCube's website," http://swisscube.epfl.ch/. (Quoted page 18.)

[54] D. Teney, "Design and implementation of on-board processor and software of student nanosatellite OUFTI-1 of University of Liège," Master's thesis, University of Liège, Belgium, 2009. (Quoted page 10.)

[55] P. Thirion, "Mission Design for the CubeSat OUFTI-1," Master's thesis, University of Liège, Belgium, 2009. (Quoted pages 8, 50 et 87.)

[56] D. Vallado, *Fundamentals of Astrodynamics and Applications* , 3rd ed. Microcosm Press and Kluwer Academic Publishers, 2007. (Quoted page 23.)

[57] J. Van Noord, "Icarus Final Thermal Report," http://data.engin.umich.edu/Icarus/, Nov 1999. (Quoted page 42.)

[58] VARTA Microbattery GmbH, "VARTA Sales Program and Technical Handbook, VARTA PoLiFlex® Batteries Superior Polymer Technology," http://www.varta-microbattery.com, Feb 2008. (Quoted page 21.)

[59] P. Veughs and G. Schmetz, "ESARAD - ESATAN, Introduction aux logiciels, Rapport SF-258," University of Liège, Belgium, Tech. Rep., May 2007. (Quoted page 47.)

[60] P. Villano, M. Carewska, and S. Passerini, "Specific heat capacity of lithium polymer battery components," *Thermochimica Acta*, vol. 402, no. 1-2, pp. 219 – 224, 2003. [Online]. Available: http://www.sciencedirect.com/science/article/B6THV-47NF62S-4/2/4651f95f8ef619f68976a9d85dfe9b60 (Quoted page 59.)

[61] N. T. Wakelyn, "Thermal control coating," National Aeronautics And Space Administration, NASA, Tech. Rep., nov 1964, patented Jul, 1968. (Quoted pages ix et 60.)

[62] J. R. Wertz and W. J. Larson, *Space Mission Analysis and Desig*, 3rd ed. Microcosm Press and Kluwer Academic Publishers, 1999. (Quoted page 21.)

[63] J. Wertz, "Conception et réalisation du système de déploiement des antennes du nanosatellite OUFTI-1," Master's thesis, Gramme Institute, Belgium, 2009. (Quoted pages viii, 9 et 70.)

[64] A. Wiberg, "Thermal study on hardware with comparisons between physical measurements and simulations," ABB Automation Technologies AB, Tech. Rep., may 2005. (Quoted page 42.)